

1



2

# Exploiting CVD diamond properties for particle detection and identification

3

4

5

Matevž Červ

6

Vienna University of Technology

7

A thesis submitted for the degree of

8

*Doctor of technical sciences*

9

Geneva 2016



# <sup>10</sup> Contents

<sup>11</sup> <b>1</b>	<b>Introduction</b>	<b>1</b>
<sup>12</sup> 1.1	Fundamental research . . . . .	2
<sup>13</sup> 1.1.1	CERN . . . . .	3
<sup>14</sup> 1.1.2	Particle accelerators . . . . .	4
<sup>15</sup> 1.1.3	The ATLAS experiment . . . . .	5
<sup>16</sup> 1.1.4	Atominsttitut, Vienna . . . . .	7
<sup>17</sup> 1.1.5	n-ToF . . . . .	7
<sup>18</sup> 1.2	Particle detectors . . . . .	8
<sup>19</sup> 1.2.1	Semiconductor detectors . . . . .	9
<sup>20</sup> 1.2.2	Diamond sensors . . . . .	11
<sup>21</sup> <b>2</b>	<b>Signal formation in diamond</b>	<b>13</b>
<sup>22</sup> 2.1	Principles of signal formation in semiconductors . . . . .	14
<sup>23</sup> 2.1.1	Signal induction by moving charges . . . . .	16
<sup>24</sup> 2.1.2	Radiation-induced electrical pulses . . . . .	18
<sup>25</sup> 2.1.3	Signal charge fluctuations . . . . .	19
<sup>26</sup> 2.2	Carrier transport in a diamond sensor . . . . .	19
<sup>27</sup> 2.3	Electronics for signal processing . . . . .	22
<sup>28</sup> 2.3.1	Signal preamplifiers . . . . .	23
<sup>29</sup> 2.3.1.1	Current-sensitive amplifier . . . . .	23
<sup>30</sup> 2.3.1.2	Charge-sensitive amplifier . . . . .	24
<sup>31</sup> 2.3.1.3	Analogue electronic noise . . . . .	25
<sup>32</sup> 2.3.2	Analogue-to-digital converters . . . . .	25
<sup>33</sup> 2.3.3	Digital signal processing . . . . .	26
<sup>34</sup> <b>3</b>	<b>Experimental results</b>	
<sup>35</sup>	<i>Diamond irradiation study</i>	<b>28</b>
<sup>36</sup> 3.1	Measurement setup . . . . .	29
<sup>37</sup> 3.1.1	Preamplifiers . . . . .	29
<sup>38</sup> 3.1.1.1	Calibration . . . . .	30
<sup>39</sup> 3.1.2	Diamond samples . . . . .	31
<sup>40</sup> 3.1.3	Readout devices . . . . .	32
<sup>41</sup> 3.1.4	Setup for the efficiency study using $\beta$ particles . . . . .	32
<sup>42</sup> 3.1.5	Room temperature $\alpha$ -TCT setup . . . . .	33

## CONTENTS

---

43	3.1.6	Cryogenic $\alpha$ -TCT setup . . . . .	33
44	3.2	Charged particle pulses and spectra . . . . .	35
45	3.2.1	Noise limitations . . . . .	35
46	3.3	Radiation limitations . . . . .	37
47	3.3.1	Quantifying radiation damage in diamonds . . . . .	38
48	3.3.1.1	Irradiation with a $\pi_{300 \text{ MeV}}$ beam . . . . .	39
49	3.3.1.2	Charge collection efficiency and charge collection distance . . . . .	39
50	3.3.1.3	Irradiation damage factor . . . . .	40
52	3.3.2	Long-term measurement stability . . . . .	41
53	3.3.2.1	$\beta$ long-term stability . . . . .	42
54	3.3.2.2	$\alpha$ long-term stability . . . . .	43
55	3.4	Temperature limitations . . . . .	47
56	3.4.1	Temperature-variant $\alpha$ -TCT before irradiation . . . . .	49
57	3.4.2	Temperature-variant $\alpha$ -TCT after irradiation . . . . .	51
58	3.4.2.1	Collected charge as a function of temperature . . . . .	52
59	3.4.2.2	Charge trapping . . . . .	54
60	3.5	Conclusion . . . . .	58
61	<b>4</b>	<b>Charge monitoring</b>	
62		<i>The ATLAS Diamond Beam Monitor</i>	<b>59</b>
63	4.1	Luminosity measurements . . . . .	60
64	4.2	Diamond pixel module . . . . .	61
65	4.2.1	Sensors . . . . .	62
66	4.2.2	Front-end electronics . . . . .	63
67	4.3	Module assembly and quality control . . . . .	65
68	4.3.1	Assembly . . . . .	65
69	4.3.2	Testing . . . . .	66
70	4.3.3	Installation and commissioning . . . . .	68
71	4.4	Performance results . . . . .	69
72	4.4.1	Source tests . . . . .	69
73	4.4.2	Test beam results . . . . .	71
74	4.5	Operation . . . . .	72
75	4.5.1	Positioning . . . . .	72
76	4.5.2	Data taking during collisions . . . . .	73
77	4.6	Conclusion . . . . .	75
78	<b>5</b>	<b>Current monitoring</b>	
79		<i>Real-time particle identification</i>	<b>77</b>
80	5.1	Motivation . . . . .	78
81	5.2	Requirements . . . . .	78
82	5.3	Device specifications . . . . .	79
83	5.4	Pulse parameters . . . . .	79

## CONTENTS

---

84	5.5 Applications . . . . .	81
85	5.6 Description of the firmware . . . . .	82
86	5.6.1 Design constraints . . . . .	82
87	5.6.2 Analysis module . . . . .	83
88	5.6.3 Area and width measurement . . . . .	85
89	5.6.3.1 Vector cleaning . . . . .	86
90	5.6.3.2 Algorithm . . . . .	87
91	5.7 Control and data interface . . . . .	89
92	5.7.1 Software . . . . .	89
93	5.7.2 Data readout . . . . .	89
94	5.8 Performance results . . . . .	90
95	5.8.1 Comparison between the charge- and current-sensitive spec-	
96	troscopy . . . . .	91
97	5.9 Source calibration . . . . .	94
98	5.9.1 Source measurements – scatter plots . . . . .	96
99	5.9.1.1 $^{241}\text{Am}$ source . . . . .	96
100	5.9.1.2 $^{90}\text{Sr}$ and $^{60}\text{Co}$ source . . . . .	101
101	5.10 Applications in neutron instrumentation . . . . .	105
102	5.10.1 Thermal neutron flux monitoring . . . . .	105
103	5.10.1.1 Measurements . . . . .	106
104	5.10.1.2 Results and discussion . . . . .	107
105	5.10.1.3 Conclusion . . . . .	107
106	5.10.2 Fusion power monitoring . . . . .	107
107	5.10.2.1 Measurements . . . . .	108
108	5.10.2.2 Results and discussion . . . . .	109
109	5.10.2.3 Conclusion . . . . .	109
110	5.10.3 Fast and thermal neutron monitoring . . . . .	111
111	5.10.3.1 Measurements . . . . .	111
112	5.10.3.2 Results and discussion . . . . .	113
113	5.10.3.3 Conclusion . . . . .	113
114	5.11 Conclusion . . . . .	114
115	Bibliography	115

# <sup>116</sup> List of Figures

<sup>117</sup> 1.1	Standard model [22]. . . . .	3
<sup>118</sup> 1.2	The Large Hadron Collider [20]. . . . .	5
<sup>119</sup> 1.3	The ATLAS Experiment [38]. . . . .	6
<sup>120</sup> 1.4	The TRIGA MARK II neutron reactor [15]. . . . .	7
<sup>121</sup> 1.5	The calorimeter in the n-ToF area [19]. . . . .	9
<sup>122</sup> 1.6	The Insertable B-Layer – a silicon particle tracker installed in the ATLAS experiment in 2014 [34]. . . . .	10
<sup>123</sup> 1.7	A pCVD diamond pad detector [23]. . . . .	11
<sup>125</sup> 2.1	In the equivalent electrical circuit diagram the electron-hole creation and drift can be modelled as a current source with a capacitor in parallel. . . . .	15
<sup>126</sup> 2.2	Stopping power for muons according to the Bethe-Bloch formula [] . . . . .	16
<sup>127</sup> 2.3	A point-like charge inducing current in a conductive plane. . . . .	17
<sup>128</sup> 2.4	Charge carrier drift in diamond for $\beta/\gamma$ and for $\alpha$ particles. . . . .	18
<sup>129</sup> 2.5	Calculated intrinsic energy resolution for silicon and diamond. . . . .	20
<sup>130</sup> 2.6	Left figure shows a profile of a diamond sensor only with an externally applied electric field. In the figure on the right a uniformly distributed space charge is added in the diamond, contributing to the internal electric field distribution. The induced current signal is proportional to the electrical field. $d$ is the thickness of the diamond sensor. . . . .	21
<sup>131</sup> 2.7	Impurities and non-uniformities in the crystal lattice due to radiation damage. . . . .	22
<sup>132</sup> 2.8	Simplified equivalent circuits of a current and charge amplifier. . . . .	23
<sup>133</sup> 2.9	Input and output signal of the current amplifier. . . . .	24
<sup>134</sup> 2.10	Input and output signal of the charge amplifier. . . . .	24
<sup>135</sup> 2.11	Input signal digitisation and quantisation error. . . . .	26
<sup>136</sup> 2.12	An example of an FPGA and an ASIC chip. . . . .	27
<sup>137</sup> 3.1	Diagram of a diamond detector readout chain. . . . .	29
<sup>138</sup> 3.2	Amplifiers used for the charge and current measurements. . . . .	30
<sup>139</sup> 3.3	Two scCVD diamond samples: A IIa 1scdhq (left) and an E6 S37 (right). . . . .	31
<sup>140</sup> 3.4	Positioning of the $\alpha$ -source on top of the sensor carrier. . . . .	34

---

*LIST OF FIGURES*

147	3.5	Superimposed and averaged pulses (left figures, current amplifier) and distributions of deposited energy (right figures, charge amplifier) for three types of radiation. Note the scale on the X axis of the distributions.	36
148			
149			
150	3.6	Diamond radiation damage - a model based on displacements per atom [26]. Added are data points for protons and pions by RD42 [35] and one data point for pions measured in the scope of this study. . . . .	39
151			
152			
153	3.7	First figure shows the CCD for S37, S79 and S52 at a range of bias voltage settings. The charge collection distance at 1 V/ $\mu\text{m}$ bias voltage for the three diamond samples is then compared to the RD42 data for pion irradiation in the second figure. The data points are about 15–25 % lower than expected from the RD42 data [35]. . . . .	41
154			
155			
156	3.8	Relative increase of charge collection over time due to priming with the $^{90}\text{Sr}$ radioactive source. The charge collection for the non-irradiated S37 stays constant. The bias voltage for this measurement is 1 V/ $\mu\text{m}$ .	43
157			
158	3.9	Relative decrease of collected charge with time for non-irradiated and irradiated diamond samples. . . . .	44
159			
160	3.10	The signal of the irradiated and primed S79 deteriorates with time for both polarities. Every plot contains 60 superimposed pulses. . . . .	45
161	3.11	Deterioration of the pulse shapes with time. . . . .	46
162	3.12	Comparison of the five procedures for the “healing” process for an irradiated diamond that had been exposed to $\alpha$ radiation with a rate of $10^1 \text{ s}^{-1}$ , with the bias voltage switched on, for at least 30 minutes.	48
163	3.13	Varied bias voltage at a fixed temperature. . . . .	49
164	3.14	Several data points between 4 K and 295 K at a bias voltage of $\pm 500 \text{ V}$ .	50
165	3.15	Varied bias voltage at a fixed temperature for an irradiated sample. . . . .	52
166	3.16	After irradiation: several data points between 4 K and 295 K at a bias voltage of $\pm 500 \text{ V}$ . . . . .	53
167	3.17	Collected charge as a function of temperature. . . . .	55
168	3.18	Charge carrier lifetime decreases with irradiation, but is stable across the range of temperatures between 4 K – 75 K and 150 K – 295 K. The first figure shows the carrier lifetime s a function of temperature whereas the second figure depicts the carrier lifetime averaged over all temperatures and plotted as a function of the $\pi$ irradiation dose. . . . .	57
169			
170			
171			
172			
173			
174			
175			
176			
177			
178			
179			
180	4.1	Diamond detectors installed in high-energy physics experiments in the last decade, sorted by the active sensor area. The first four detectors from the left are radiation monitors whereas the right two are pixel trackers. . . . .	60
181			
182			
183			
184	4.2	DBM module, top-down view. Visible is the flexible PCB with signal and power connections, the silicon sensor and a part of the FE-I4. Wire bonds from the PCB to the FE-I4 and to the sensor are also visible. . . . .	61
185			
186			

---

## LIST OF FIGURES

---

187	4.3	A pCVD wafer. The golden dots on the surface are the electrodes that are applied during the qualification test. The wafer is measured across the surface to find the regions with the highest efficiency. . . . .	62
188	4.4	FE-I4 layout, top-down view. The pink area are pixels grouped into columns, the green area below is the common logic and the red strip at the bottom are the wire bond pads. . . . .	63
189	4.5	Schematic of an analog pixel. Courtesy of the FE-I4 collaboration. . .	64
190	4.6	An assembled DBM module. . . . .	66
191	4.7	Module production with time. . . . .	67
192	4.8	Occupancy and pseudo-efficiency scans for the silicon (left) and diamond sensor (right) to check for disconnected regions and estimate the sensor's efficiency. Shadows of the electronic components are clearly visible because fewer electrons were able to traverse through such a higher amount of material. . . . .	70
193	4.9	Measurements of pseudo-efficiency and disconnected regions for all modules that went through the QC procedure. . . . .	71
194	4.10	An efficiency study of a prototype DBM diamond module in a test beam. The statistics are low ( $\sim 10$ hits/pixel) as the data was collected during a short run. . . . .	72
195	4.11	This photo highlights four telescopes installed onto the nSQPs and around the pipe. . . . .	73
196	4.12	Position of the DBM in the ATLAS experiment. . . . .	73
197	4.13	Occupancy of individual modules during collisions. Only 16 modules were taking data. . . . .	74
198	4.14	A diagram showing the radial distance $R_0$ and longitudinal distance $Z_0$ of the trajectory from the interaction point at the minimal distance $d$ . $Z$ is the axis along the beam line. Three module planes intercept a particle and reconstruct its trajectory. . . . .	75
199	4.15	These two plots show two parameters of particle tracks recorded by one of the DBM telescopes: radial and longitudinal distance of the projected tracks from the interaction point. . . . .	76
200	5.1	A pulse and its parameters. . . . .	80
201	5.2	Form Factor is the ratio between the measured area ( $a$ ) and the calculated area ( $A \times BW$ ) of the pulse. The calculated area is significantly larger than the measured area for a triangular triangular pulse, but less so for the rectangular one. The red and blue dot in the right plot are the value entries of the two pulses shown. The red and blue oval shapes depict the regions for the values expected from triangular and rectangular pulses. By carefully choosing the linear qualifier (dashed line) and taking only the entries below the cut rectangular pulses can be identified. . . . .	80
202	5.3	Firmware design structure. . . . .	82

---

*LIST OF FIGURES*

229	5.4	Code design plan. . . . .	83
230	5.5	A sample pulse. The first vector shows which samples are above the width measurement height. The second vector is a clean vector. The third line shows the position of the maximum amplitude. The vector cleaning algorithm starts from the maximum amplitude and continues in both ways along the vector. . . . .	86
231	5.6	This block counts the remaining binary ones in the clean vectors and outputs this value as the pulse width. . . . .	86
232	5.7	This block masks the input data with the clean vector and sums the remaining samples. . . . .	87
233	5.8	Vector cleaning routine outputs two vectors - one forward in time and one back in time from the peak of the pulse. . . . .	87
234	5.9	One logic step in the algorithm chain before and after Karnaugh minimisation. . . . .	88
235	5.10	Vector is divided into two 16-bit logic chains. The algorithm logic is then run on the two chains separately. The results are then merged into one 32-bit clean vector by using a set of AND gates. . . . .	88
236	5.11	Abstraction levels of the controller software. . . . .	89
237	5.12	This figure shows the capability of the device to analyse all arriving pulses for a range of input frequencies. The highest achievable rate with zero lost pulses is $5 \times 10^6 \text{ s}^{-1}$ . . . . .	91
238	5.13	These diagrams show the linearity of the measurements and their stability with respect to analog noise. . . . .	92
239	5.14	Spectrum of a $^{148}\text{Gd}^{239}\text{Pu}^{241}\text{Am}^{244}\text{Cm}$ source using a Cx and a C2 amplifier. . . . .	93
240	5.15	Accumulated pulses for all runs. . . . .	95
241	5.16	$^{241}\text{Am}$ , $e^-$ collection. Qualifier: FWHM. Optional qualifiers: Amplitude, Form Factor. . . . .	98
242	5.17	$^{241}\text{Am}$ , $h^+$ collection. Qualifier: FWHM. . . . .	99
243	5.18	$^{241}\text{Am}$ area histograms for electron and hole collection. . . . .	100
244	5.19	$^{90}\text{Sr}$ scatter plots. . . . .	102
245	5.20	$^{60}\text{Co}$ scatter plots. . . . .	103
246	5.21	Energy distributions for $\gamma$ and $\beta$ particles. . . . .	104
247	5.22	Thermal neutrons, photons. Qualifier: FWHM. . . . .	107
248	5.23	Energy spectrum after applied qualifiers reveals the tritium and $\alpha$ peak	108
249	5.24	$^{239}\text{Pu}$ Be. Qualifiers: BW-FWHM, FWHM, Form Factor . . . . .	110
250	5.25	$^{239}\text{Pu}$ Be, energy distribution of the neutrons interacting in the ballistic centre. . . . .	111
251	5.26	Fast neutrons, thermal neutrons, photons. Qualifiers: BW-FWHM, FWHM, Form factor, Slope. . . . .	112
252	5.27	Energy spectrum in CROCUS before and after applied qualifiers . . . . .	113

*LIST OF FIGURES*

---

# <sup>270</sup> Chapter 1

## <sup>271</sup> Introduction

<sup>272</sup> The aim of the thesis is to present and discuss applications of diamond based particle  
<sup>273</sup> detectors.

<sup>274</sup> The introductory chapter paints a picture of the current state of particle physics  
<sup>275</sup> research. It presents some of the research institutes that are active in this field,  
<sup>276</sup> pushing the boundaries of human knowledge further. It explains their goals and the  
<sup>277</sup> means with which they are achieving them. Next section describes particle detectors  
<sup>278</sup> in a broad sense – their history and the types existing now. One type in particular –  
<sup>279</sup> a diamond detector – is then described more in detail.

<sup>280</sup> The second chapter discusses the properties of diamond detectors. First it explains  
<sup>281</sup> the detector chain into individual parts and describes them in detail – sensors, am-  
<sup>282</sup> plifiers, digitisers and signal processing units. Second, it contains information about  
<sup>283</sup> energy resolution in diamond, the analog and digital noise contribution, etc. Third, it  
<sup>284</sup> presents the principles of signal formation, starting with the famous Shockley-Ramo  
<sup>285</sup> theorem and building from there. It uses the theorem to show that different types of  
<sup>286</sup> radiation induce different electrical signal shapes.

<sup>287</sup> The base laid down in the second chapter is complemented in the third where the  
<sup>288</sup> measurements are presented and the results discussed. The chapter focuses on charge  
<sup>289</sup> measurement stability with respect to irradiation damage.

<sup>290</sup> Building on the understanding of the behaviour of the diamond, two applications  
<sup>291</sup> were developed. The fourth chapter describes the Diamond Beam Monitor, a detec-  
<sup>292</sup> tor that makes use of the diamond's charge measurement capabilities and its high  
<sup>293</sup> radiation hardness. This detector has been installed in one of the largest particle  
<sup>294</sup> physics experiments in the world and is currently taking data. Here, its development  
<sup>295</sup> process is presented: the quality control procedures during assembly and installation,  
<sup>296</sup> its performance in the test environment and some recent experimental data.

<sup>297</sup> The final and most important chapter describes the real-time application for par-  
<sup>298</sup> ticle identification. Here the shape of the current signal of the diamond sensor is used  
<sup>299</sup> to discriminate different types of radiation in real time. The chapter includes the de-  
<sup>300</sup> scription of the device's logic and algorithms, experimental results and applications  
<sup>301</sup> in neutron monitoring.

## 302 1.1 Fundamental research

303 This section gives a short overview of the institutes and collaborations carrying out  
304 fundamental physics research. The facilities were used for the research carried out in  
305 this thesis.

306 The aim of fundamental research is to define scientific theories and verify them  
307 to improve our understanding of the universe. It does not in itself focus on applying  
308 this research by developing products and is not meant to create a direct return on  
309 investment. Instead, it expands the overall knowledge of the human kind - by making  
310 the results freely available to the general public.

311 Particle physics research peers into the smallest constituents of the universe, dis-  
312 secting the atoms into quarks and electrons, catching cosmic rays and figuring out  
313 what dark matter is made up of. Particle physicists want to explain the phenomena  
314 surrounding us by studying the fundamental particles and the mechanisms governing  
315 their interactions. By understanding this, we would be able to answer difficult ques-  
316 tions; How did the universe begin? What is the invisible force (dark matter, dark  
317 energy) pushing the galaxies apart from each other? Where does mass come from?  
318 Why is there almost no antimatter in the universe? In this effort, scientists have  
319 formed several theories. One of them, the Standard Model of particles, is currently  
320 the best theory to describe the constituents of matter and their interactions.

321 **The Standard Model** (SM) is a physics theory developed in the 1970's [37]. It  
322 was designed to explain the current experimental results. As such, it was also able to  
323 predict new discoveries and was a driving force for the scientists to invest time and  
324 money in developing new experiments. To date, it is by far the most established and  
325 verified physics theory. It explains how the basic building blocks of matter – *fermions*  
326 – interact with each other via mediators of interactions called *bosons*. There are two  
327 main families of fermions - *quarks* and *leptons*, as shown in figure 1.1. Each group  
328 consists of six members divided into three *generations*, the first being the lightest and  
329 most stable and the last the heaviest – unstable. The nature around us is made up  
330 of the stable particles – those from the second or third generations can only be found  
331 in cosmic rays or produced artificially using particle accelerators.

332 Quarks have a spin of 1/2 and a charge of either +2/3 (up, charm, top) or -1/3  
333 (down, strange, bottom) while the leptons have a spin of 1/2 and a charge of either 1  
334 (electron, muon, tau) or 0 (electron neutrino, muon neutrino, tau neutrino). Leptons  
335 only exist individually – they do not cluster. Quarks, however, immediately form a  
336 cluster of either two (unstable), three (more stable) or five (unstable). Two up and  
337 one down quark make up a proton whereas two down and one up quark make up a  
338 neutron.

339 In addition to fermions, each particle has its corresponding antiparticle – a particle  
340 with the same mass but the opposite charge. If an antiparticle hits a particle, they  
341 annihilate each other, producing energy in form of photons.

342 Bosons are the carriers of force, mediating weak ( $W^+$ ,  $W^-$  and  $Z$  bosons), strong

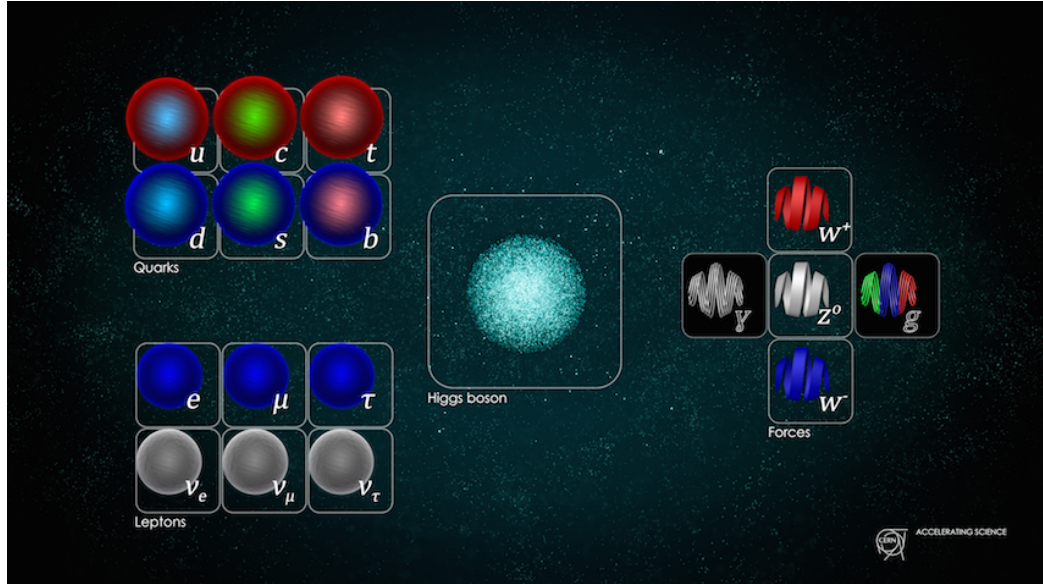


Figure 1.1: Standard model [22].

(gluons) and electromagnetic (photons) interactions. The weak interaction is responsible for the radioactive decay of subatomic particles, thus playing an essential role in nuclear fission – a process taking place in the stars. The electromagnetic interaction works at a macroscopic level – it allows particles to interact via electric and magnetic fields. The strong interaction is effective at distances of a femtometer and it governs how quarks interact and bind with each other. An additional boson is the Higgs boson and was discovered at CERN in 2012 [2]. It is a representation of the Higgs mechanism, which gives rise to the mass (or lack thereof) of all the particles in the Standard Model.

### 1.1.1 CERN

CERN (European Centre for Nuclear Research) [6] is the largest particle physics laboratory in the world, straddling the Swiss-French border just outside Geneva. It was established in 1954 to bring the war-torn Europe together by means of fundamental scientific research. Today, its 22 member state countries and several observer states contribute approximately 1 billion CHF annually to fund the research and development. More than 10000 scientists, engineers, technicians, students and others from all around the globe work at CERN on many projects in research fields ranging from particle to nuclear physics. The scope is to probe the fundamental structure of the universe and to understand the mechanisms governing it. Therefore CERN's main function is to provide the infrastructure for high-energy physics experiments. These are carried out using large machines called particle accelerators. These instruments boost beams of particles to high energies before making them collide with each other or with stationary targets. The resulting collisions are recorded by particle detectors and later analysed by physicists. To carry out research on the smallest constituents

## 1.1. FUNDAMENTAL RESEARCH

---

of matter, their dynamics and structure, very high energies are needed. This is why the most powerful accelerators are used for fundamental research. The largest accelerators at CERN are the Proton Synchrotron [], the Super Proton Synchrotron [36] and the Large Hadron Collider [], described in 1.1.2.

### 1.1.2 Particle accelerators

A particle accelerator is a machine that accelerates beams of charged particles like protons, electrons, ions etc. It generates electric fields that add kinetic energy to the particles, speeding them up. It then uses magnets to retain them within a defined trajectory and inside the evacuated beam pipe. The trajectory can be either linear (linear accelerators) or circular (circular or cyclic accelerators). The advantage of the latter ones is that they can accelerate particles many times while keeping them in orbit.

Particle accelerators are used in numerous fields ranging from fundamental and material research, cancer treatment to industrial applications, such as biomedicine and material processing. Several types of accelerators exist: electrostatic accelerators, linear accelerators (LINACs), cyclotrons, synchrocyclotrons, synchrotrons, synchrotron radiation sources and fixed-field alternating gradient accelerators (FFAGs).

**The Large Hadron Collider** (LHC, figure 1.2) at CERN is the largest particle collider in the world. It was build between 1998 and 2008 and was first successfully started in 2010 and operated stably until 2013 when it underwent a two years long upgrade. Its second operational cycle started at the beginning of 2015.

The LHC is a 27 km long circular machine set up in a tunnel deep under the surface, ranging from 50 to 175 m below ground. It accelerates two proton beams to the energy of 6.5 TeV per beam before it makes them to collide with each other with the energy of 13 TeV at four different points around its circumference. The hair-thin particle beams travel inside two evacuated pipes with a  $\sim$ 5 cm radius. Coils made up of a superconductive material are wound up around the pipes in special patterns. When cooled down to -271 °C using liquid helium, they become superconductive; the resistivity of the material drops significantly, minimising the heat dissipation despite high electric currents. These produce strong magnetic fields which bend the particles and keep them in a circular trajectory. The particles are accelerated when traversing the radio-frequency (RF) cavities with the RF frequency of 400 MHz. This oscillating frequency creates buckets – compartments for bunches of highly energetic particles – which are 2.5 ns long. Only one out of ten buckets is filled, so the bunches are spaced at 25 ns. This defines the machine's clock (40 MHz) as well as the maximum rate of collisions - the bunches travelling in the opposite direction cross at the intersections up to 40 million times per second. Currently around 20 collisions occur during every bunch crossing, yielding the maximum collision rate of the order of  $10^9$  s<sup>-1</sup>. The number of collisions will further increase in the following years; the number of particles in every bunch will be increased and the transverse spread of the bunches will be

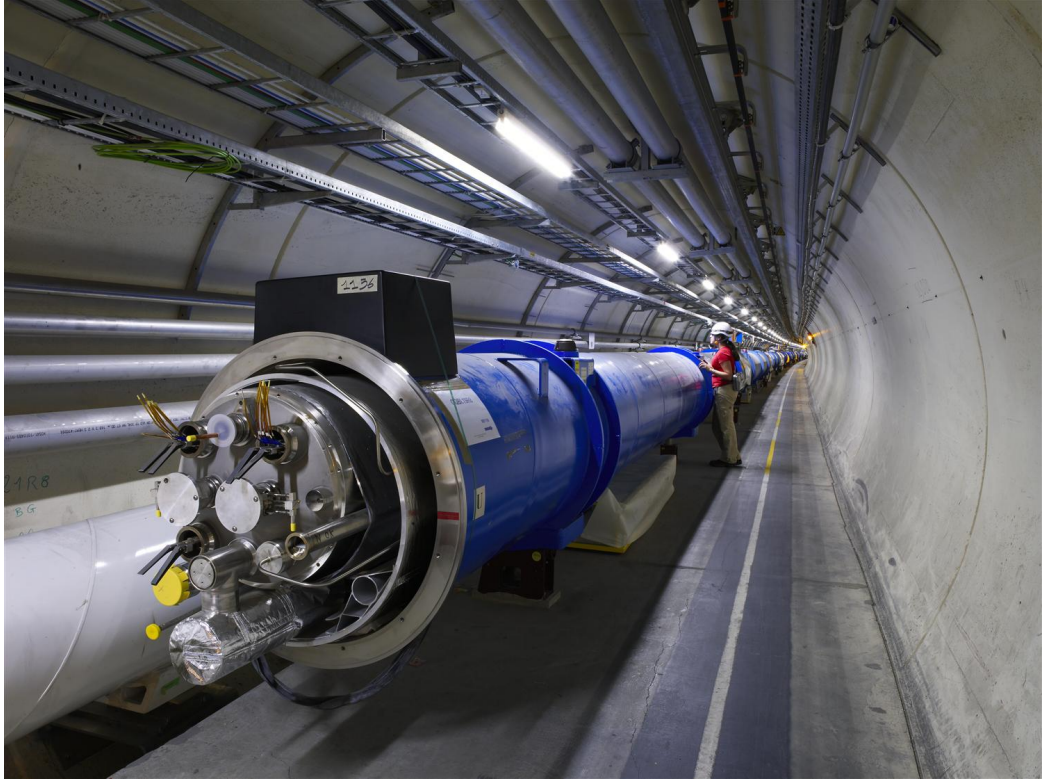


Figure 1.2: The Large Hadron Collider [20].

407 decreased, squeezing the bunches further. The density will therefore be increased,  
 408 which will in turn increase the collision probability – the cross-section. The original  
 409 design number of collisions accumulated over the years of operation is presented in the  
 410 form of integrated luminosity [] and is of the order of  $300 \text{ fb}^{-1}$  (inverse femtobarn).  
 411 After the planned upgrades in 2020, the High-Luminosity LHC [] will achieve up to  
 412  $3000 \text{ fb}^{-1}$ .

### 413 1.1.3 The ATLAS experiment

414 ATLAS (short for A Toroidal Lhc ApparatuS, figure 1.3) [] is a particle physics ex-  
 415 periment at CERN. Its purpose is to verify current theories and to search for new  
 416 discoveries by observing and analysing high energy proton-proton collisions produced  
 417 by the LHC. It is the biggest experiment at CERN by dimensions (45 m in length and  
 418 26 m in height) and the number of people involved (more than 3000 physicists and en-  
 419 gineers). The ATLAS experiment consists of a number of detectors, each designed to  
 420 measure a specific property of the particles and photons produced during the collision.  
 421 The closest to the collision point is the Inner Detector (ID), which consists of several  
 422 layers of highly spatially segmented semiconductor sensors recording single points of  
 423 the incident particles. These points are later reconstructed into particle tracks. In ad-  
 424 dition, a strong magnetic field of 2 T curves the paths of the charged particles, which  
 425 in turn allows the ID to identify an individual particle's charge and momentum. The

## 1.1. FUNDAMENTAL RESEARCH

---

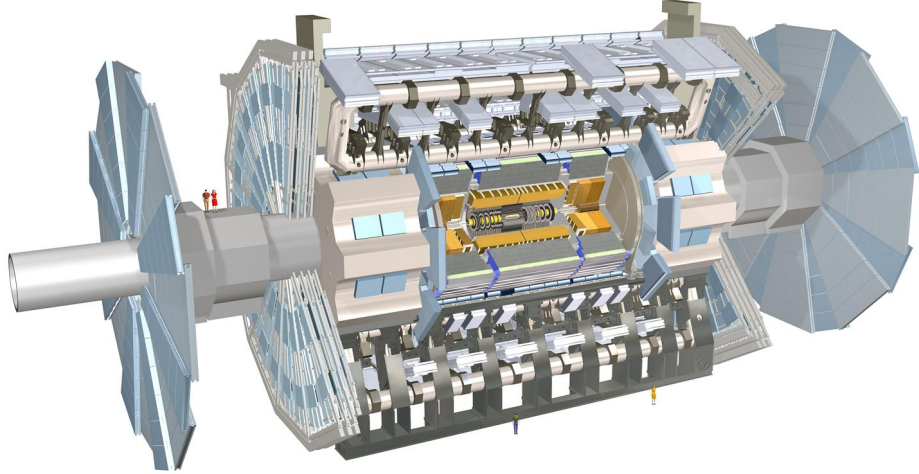


Figure 1.3: The ATLAS Experiment [38].

426 next two parts are the electromagnetic and tile calorimeter. These detectors weigh  
427 a few thousand tonnes and measure the energy of the particles that are stopped in  
428 the material. The only particles that make it through the calorimeters are muons.  
429 These are detected by the Muon Spectrometer, a set of large detector plates placed  
430 all around the calorimeters. Last is the superconductive magnet, which provides the  
431 magnetic field through the entire ATLAS except the ID, which already has its own  
432 magnets. To sum up, the Inner Detector measures the charge and momenta of the  
433 particles, the calorimeters measure their energies, the Muon Spectrometer measures  
434 muons and the magnets provide magnetic fields, which curve the trajectories of the  
435 charged particles, allowing for identification of particle momentum.

436 A complex Trigger and Data Acquisition system (TDAQ) is in place to distribute  
437 the clock signal, configure the detectors, trigger them and handle the output data.  
438 They are then stored at the CERN computer centre and distributed across the globe  
439 by means of the GRID – a distributed data analysis and data storage system.

440 The ATLAS detector has been designed to measure every collision taking place in  
441 its core. With 25 ns between collisions, this makes up 40 million collisions per second.  
442 In reality, the maximum achievable rate is about 300 kHz. The recorded collision is  
443 called an event. Every event holds information from all the detector channels within  
444 ATLAS. With  $\sim 10^6$  channels, an event size is approximately 10 MB. At the maximum  
445 achievable rate this means a data rate of up to 3 TB/s. To reduce the amount of data  
446 stored a special classification system with a complex trigger logic is in place to decide  
447 which events should be stored and analysed further. It is programmed to decide in  
448 the order of tens of microseconds after an event whether it is potentially interesting

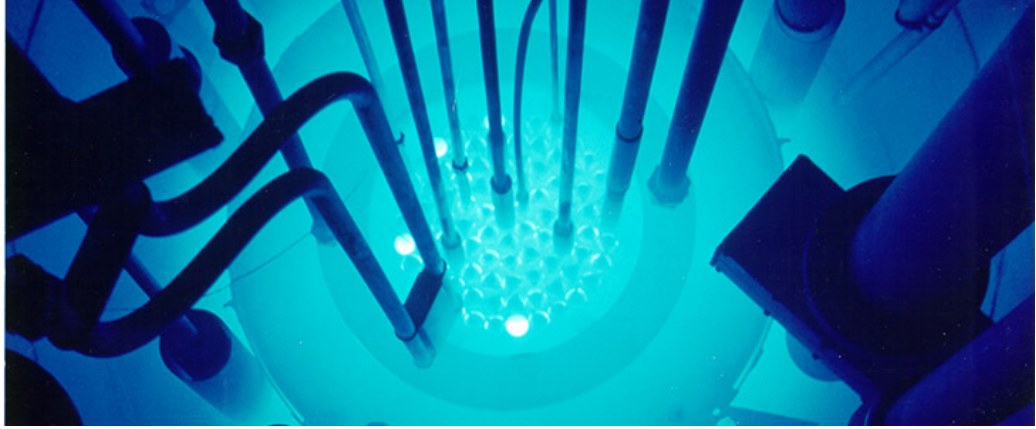


Figure 1.4: The TRIGA MARK II neutron reactor [15].

449 or not. If so, the system triggers the readout of the entire detector. This way the  
450 recorded event rate is reduced from 300 kHz to  $\sim$ 500 Hz.

#### 451 1.1.4 Atominstitut, Vienna

452 Atominstitut (ATI) [2], an institute for atomic and subatomic physics, was estab-  
453 lished in 1958 in Vienna as an inter-university institute. It currently houses around  
454 200 people involved in a broad range of research fields: quantum, particle, neutron,  
455 nuclear, radiation and reactor physics, quantum optics etc. Its central facility is a  
456 TRIGA MARK II neutron reactor (described in detail below).

457 As of 2002 the ATI is part of the University of Technology in Vienna.

458 **TRIGA MARK II neutron reactor** [12] is a reactor of a swimming-pool type  
459 used for training, research and isotope production. It is one of 40 such reactors  
460 worldwide, produced by the Californian company General Atomic in the early 60's. It  
461 is capable of continuous operation at a maximum output power of 250 kW. The reactor  
462 core consists of 3 kg of 20 % enriched uranium ( $^{235}\text{U}$ ). The fuel moderator rods are  
463 mostly made up of zirconium with low percentage of hydrogen and uranium. Both the  
464 core and the rods are immersed in a pool of water as shown in figure 1.4 for the purpose  
465 of cooling and radiation protection. The surrounding concrete walls are 2 m wide  
466 with an added graphite layer for improved shielding. Four main experimental beam  
467 holes are placed radially through the walls. All exits are heavily shielded to prevent  
468 radiation damage to people, but still leaving enough space to set up experiments.  
469 Apart from the beam holes, there are several other exits and components, e.g. a  
470 thermal column for generation of thermal (low energetic) neutrons.

#### 471 1.1.5 n-ToF

472 n-ToF (or neutron time-of-flight) [9] is a scientific collaboration with the aim of study-  
473 ing neutron-nucleus interactions. Over 30 institutes and universities are currently

## 1.2. PARTICLE DETECTORS

---

474 active members of this collaboration, among them Atominstitut in Vienna. n-ToF  
475 is also a facility at CERN where the experiments are carried out in a 200 m long  
476 experimental area. The knowledge stemming from the experimental results can then  
477 be applied in various fields ranging from nuclear technology and cancer therapy to  
478 astrophysics.

479 A pulsed beam of highly energetic protons (20 GeV/c) is produced by the Proton  
480 Synchrotron (PS) and aimed at a fixed lead spallation target. Each proton hitting  
481 the target produces around 300 neutrons of various energies. Initially highly energetic  
482 neutrons are slowed down by the target and by a slab of water placed behind it. This  
483 broadens their energy spectrum, which then ranges from meV (thermal neutrons) to  
484 GeV (fast neutrons). The neutrons are then collimated and sent through a 185 m  
485 long evacuated pipe to the experimental area, where they are made to collide with  
486 another target or a sample. The radiation resulting from the collisions is detected  
487 by a set of dedicated detectors around the interaction point, as shown in figure 1.5.  
488 Having different energies, neutrons travel with different speeds, highly energetic ones  
489 reaching the target faster than those with low energies. The analysis of collisions  
490 with a precise timing allows for a determination of the interaction probability with  
491 the sample material as a function of incident neutron energy.

## 492 1.2 Particle detectors

493 Particle detectors, or radiation detectors, have first come into use at the end of the  
494 19th century. At that time Wilhelm Röntgen used a photographic plate onto which  
495 he shone X-rays. Soon after, in 1912, Victor F. Hess discovered cosmic rays during  
496 a balloon flight. This paved the way for development of particle detectors. A cloud  
497 chamber was designed – a chamber filled with a supersaturated vapour of water or  
498 alcohol. If a highly energetic particle traversed the chamber, the mixture ionised,  
499 creating condensation nuclei. These traces were visible and were photographed. All  
500 the subsequent particle detectors relied on the same principle of interaction between  
501 the particles – ionisation. The bubble chamber invented in 1952 used a superheated  
502 transparent liquid – a liquid heated just below its boiling point. A particle ionised  
503 the liquid, forming microscopic bubbles along its trajectory. Then followed the spark  
504 chamber and the wire chamber where the particle ionised the gas, causing a spark  
505 between two parallel plates at a high potential difference. These are nowadays used in  
506 museums as showcases. Next were ionisation chambers, which measured the induced  
507 current of the free ionised charges moving in an externally applied electric field.  
508 Finally in the 1960s, semiconductor detectors were introduced. Their principle of  
509 operation is similar to that of an ionisation chamber, with the difference that a semi-  
510 conductive material is used as an ionisation medium instead of gas. Nowadays an  
511 ensemble of several types of detectors is used as a single detector system. Many  
512 considerations need to be taken into account when designing such a system: detector  
513 geometry, segmentation, event rate, efficiency, readout, support structures, cabling,  
514 cooling, cost etc.

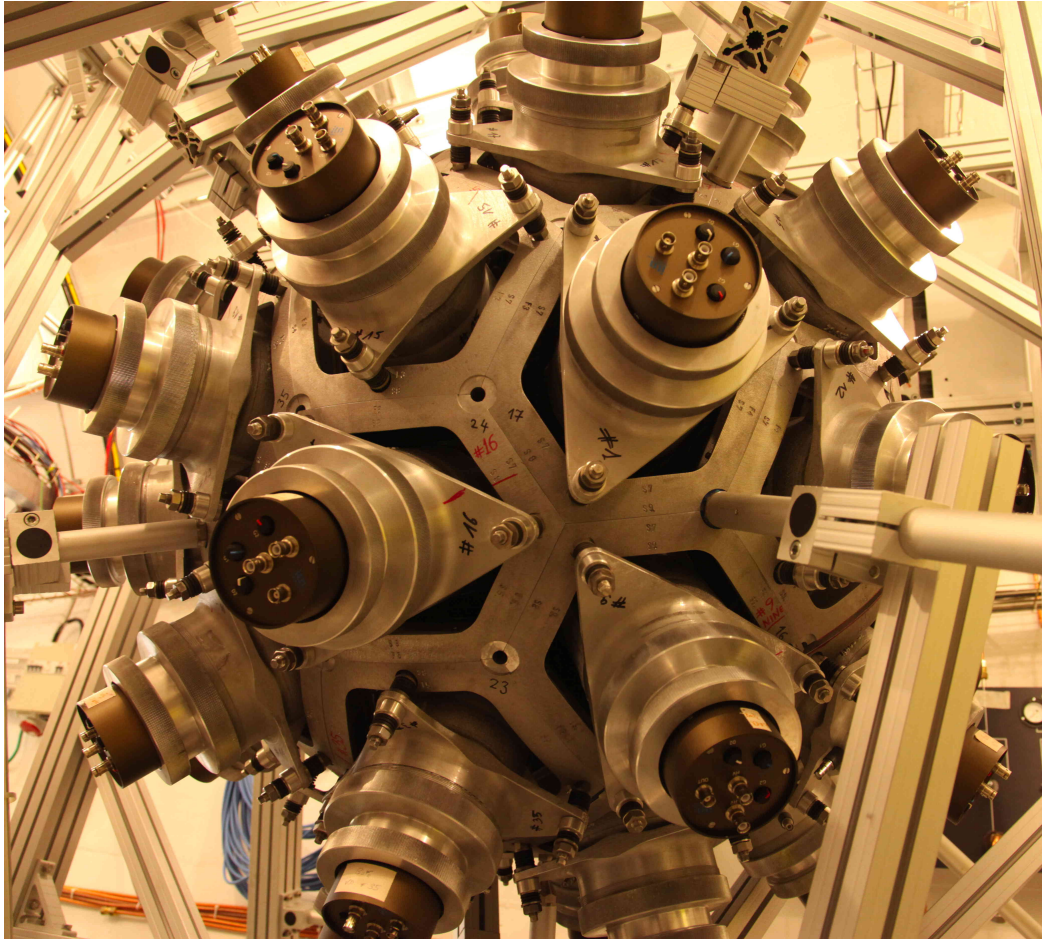


Figure 1.5: The calorimeter in the n-ToF area [19].

515 Particle detectors can be divided in two groups: tracking detectors and calorimeters.  
 516 The former are designed to measure trajectories (momentum) of particles and  
 517 photons with a minimal impact on their flight path or energy with the aim to optimise  
 518 the spatial resolution. Typically they are semiconductor detectors. The calorimeters,  
 519 on the other hand, measure the energy of the particles/photons by stopping them.  
 520 This means they need to be heavy and dense. A typical physics experiment nowadays  
 521 would consist of a tracking detector enclosed by a calorimeter. This way both the  
 522 momentum and energy are derived, measuring energy, charge and trajectory of every  
 523 particle/photon.

### 524 1.2.1 Semiconductor detectors

525 Semiconductor particle detectors are devices that use a semiconductor for detecting  
 526 radiation. They work on the principle of an ionisation chamber. An incident particle  
 527 or a photon ionises the atoms in the crystal lattice. The charges are freed if the  
 528 deposited energy is higher than the energy band gap. The freed charge carriers start  
 529 drifting in an externally applied electric field, inducing current on the electrodes.

## 1.2. PARTICLE DETECTORS

---

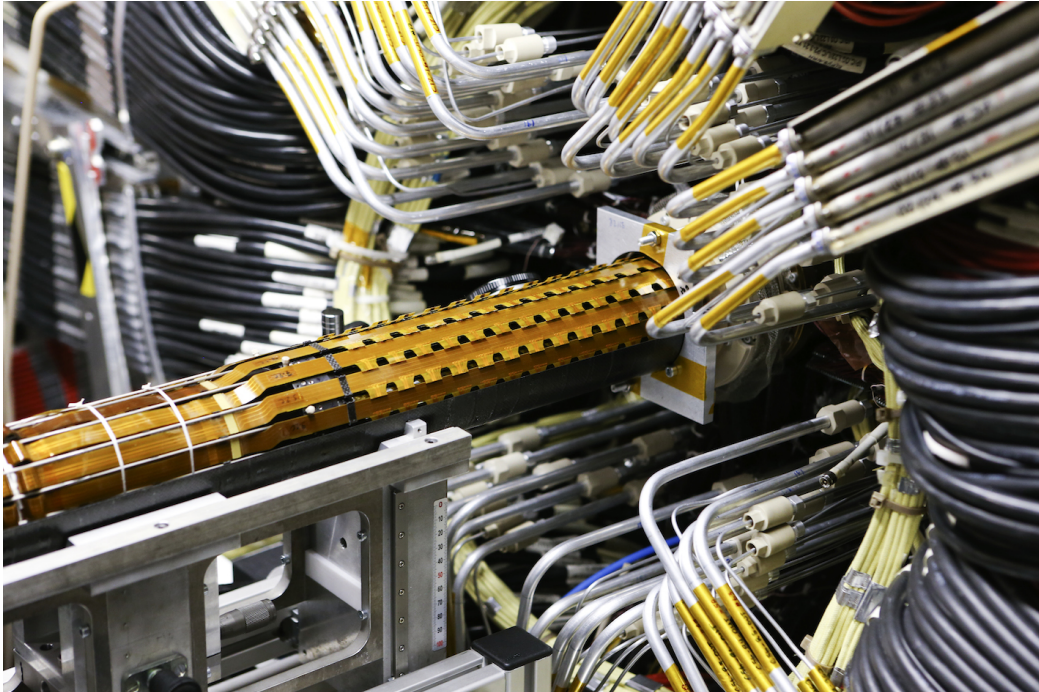


Figure 1.6: The Insertable B-Layer – a silicon particle tracker installed in the ATLAS experiment in 2014 [34].

530 A number of semiconductor materials exist, each with a different band gap. Ger-  
531 manium (Ge) for instance has a band gap of 0.67 eV, which means that most of the  
532 electrons at the room temperature are already in an excited state due to thermal  
533 excitation. The 5.5 eV band gap in the diamond, on the other hand, prevents the  
534 thermally excited electrons to jump to the conduction band. In addition, the gap is  
535 too wide for the visible light to excite the electrons. Silicon with an energy gap of  
536 1.12 eV fulfils most of the needs for particle physics requirements and is therefore the  
537 most widely used material for particle detection.

538 Semiconductor detectors are most widely used for tracking applications, like the  
539 Insertable B-Layer shown in figure 1.6 [39], which was installed in ATLAS Experiment  
540 in 2014. First , they can be produced in thin layers to minimise the impact on the  
541 path of the incident particles. Second, their low sensor capacitance allows for a fast  
542 signal response. Third, they are highly efficient and highly resistant to radiation  
543 damage. Finally, the industrial processes allow for a fine spatial segmentation, which  
544 in turn improves the track resolution of a detector system.

545 Semiconductor sensors come in several configurations. The simplest type is a pad  
546 – a single plate with two electrodes. Pads are used for particle counting and radiation  
547 monitoring. Next is a strip detector, a more finely segmented detector made out of  
548 long parallel sensing areas or strips. Normally each strip has its own signal line for  
549 readout. Usually the strip detectors are used in pairs – one detector is placed on top  
550 of the other at an angle to increase spatial resolution in both axes. The third and  
551 the most finely segmented is a pixel detector, consisting of a 2D array of independent

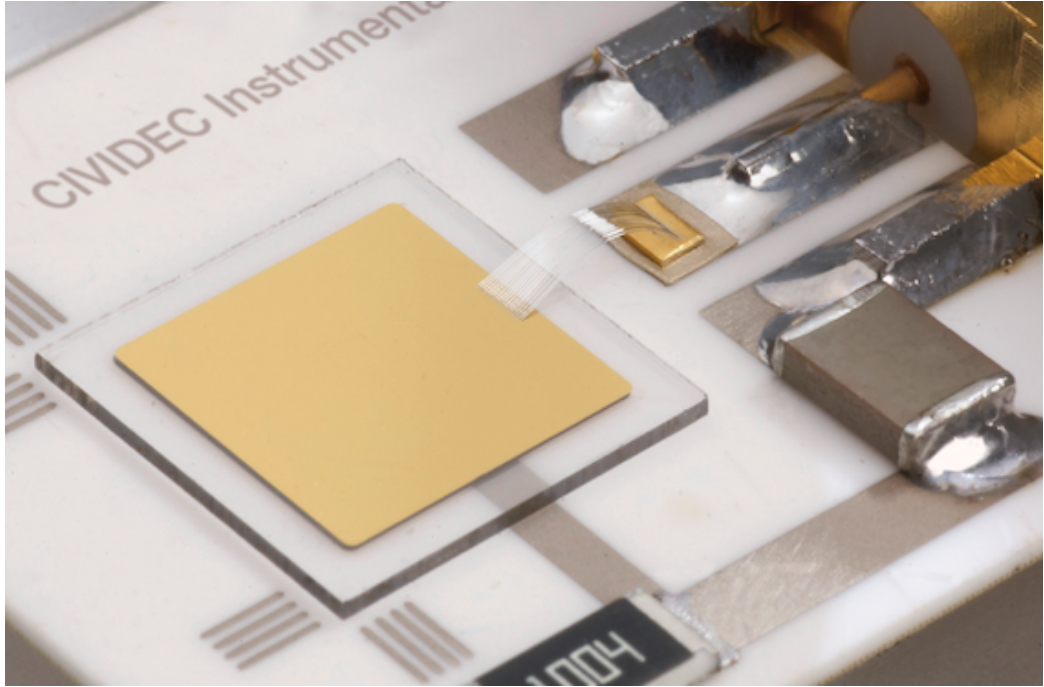


Figure 1.7: A pCVD diamond pad detector [23].

552 sensing areas. In tracking applications, pixel detectors are used where the need for a  
553 high detection resolution and granularity is the highest. Due to their high production  
554 cost and a high number of signal channels, they can only cover limited areas. Strip  
555 detectors are cheaper to produce and can be used to cover larger areas in several  
556 consecutive layers.

### 557 1.2.2 Diamond sensors

558 Diamond has been known for over two millennia, valued for its mechanical properties  
559 and its appearance. When the procedures for its synthesis were discovered, diamond  
560 made its way to a broad range of industries which exploit its optical and electrical  
561 properties. The discovery of the Chemical Vapour Deposition (described below) as  
562 a new synthesis process gave rise to a range of new applications. Purer specimens  
563 are used in electronics, high-power switching devices, electrochemical systems, radi-  
564 ation sensors, quantum computing etc. Recently it was found that it also exhibits  
565 superconductivity. This thesis focuses on the use of diamond for radiation detection.  
566

567 Compared to a natural diamond, a detector-grade CVD diamond has almost no  
568 impurities (foreign atoms like nitrogen or boron). If proper procedures are followed,  
569 the diamond lattice can be grown very uniformly. This in turn improves electrical  
570 properties of the grown sample. Diamond is an almost perfect thermal and electri-  
571 cal insulator. Compared to silicon, the most widely used semiconductor material for  
572 radiation detection, it has many advantages, which are described in detail in chap-

## 1.2. PARTICLE DETECTORS

---

573 ter 2. Figure 1.7 shows a diamond pad sensor produced by CIVIDEC Instrumentation  
574 GmbH.

575 **Chemical vapour deposition** (CVD) [] is a process where a material is deposited  
576 from a gas onto a substrate, involving chemical reactions. It is often carried out  
577 under high pressure and high temperatures. It takes place in enclosed chambers  
578 called furnaces with careful regulation of the temperature, pressure and gas mixture.  
579 Synthetic diamond is grown at 700–900 °C with a mixture of hydrogen and methane  
580 gas. At this temperature the molecules dissociate into carbon and hydrogen atoms.  
581 The carbon atoms are the building blocks and are deposited on the surface of the  
582 substrate.

583 Under a carefully controlled pressure and temperature conditions with an added abra-  
584 sive atomic hydrogen the graphitic bonds break and form into diamond bonds. The  
585 speed of the growth can be anywhere between 0.1 and 10 µm per hour. The detector  
586 grade samples are grown at a rate of the order of 1 µm per hour. They can grow up to  
587 several millimetres in thickness. The width of the samples, however, depends entirely  
588 on the substrate used. Diamond can be deposited on various materials: diamond,  
589 silicon, tungsten, quartz glass etc. The substrate material must be able to withstand  
590 the high temperatures during the CVD process. The diamond substrate does not  
591 need any surface pre-treatment. Carbon atoms form bonds with atoms in the exist-  
592 ing crystal structure. This is the homo-epitaxial growth where the newly deposited  
593 atoms retain the orientation of the structure in the substrate. Other non-diamond  
594 substrates, however, need to be pre-treated, usually by being polished using diamond  
595 powder. Some powder particles remain on the surface, acting as seeds for the growth  
596 of small crystals or grains. These grains grow and at some point merge with the  
597 adjacent ones, making up a compact material. The lower side is later polished away.  
598 These diamonds are called *polycrystalline* (pCVD) whereas those grown on a diamond  
599 substrate are *single crystal* (sCVD) diamonds. The area of the former can be large -  
600 up to 0.5 m<sup>2</sup> or more compact 15 cm<sup>2</sup> in the case of detector grade diamonds. The  
601 sCVD diamonds, on the other hand, can currently only measure up to 1.5 cm<sup>2</sup>.

## 602 Chapter 2

### 603 Signal formation in diamond

604 This chapter describes the fundamentals of signal formation in a diamond sensor, as  
605 well as its use as a particle detector. This is described in section 2.1 where the energy  
606 deposition principles are explained. Then examples of ionisation are shown. Later the  
607 internal lattice defects that affect the signal are described. The final section contains  
608 the description of the remaining part of the signal chain – signal amplifiers, digitisers  
609 and devices for signal processing. Noise contributions are discussed at every stage of  
610 the signal chain.

611 Ionisation is the main signal generation mechanism in diamond, silicon and other  
612 semiconducting materials. A semiconductor sensor converts the energy deposited by  
613 an incident energetic charged particle to an electrical signal. In particular, the particle  
614 ionises the atoms in the lattice, freeing electrons and holes, which then drift towards  
615 positively and negatively charged electrodes due to an externally applied electrical  
616 field, inducing an electrical signal on the electrodes.

617 Silicon is currently considered as the industry standard for particle detection.  
618 However, there are several disadvantages of using silicon instead of diamond, due  
619 to significant differences in the material properties. In particular, the properties of  
620 silicon change significantly with radiation. For instance, the leakage current increases,  
621 which in turn increases shot noise and can lead to a thermal runaway. In addition, due  
622 to induced lattice defects, which act as charge traps, its charge collection efficiency is  
623 decreased. Both are true for diamond as well, but on a much smaller scale.

624 Table 5.2 compares the properties of diamond and silicon. Some of these values  
625 are revisited and used in the course of this thesis.

## 2.1. PRINCIPLES OF SIGNAL FORMATION IN SEMICONDUCTORS

---

Property	Diamond	Silicon
Band gap energy $E_g$ (eV)	5.5	1.12
Electron mobility $\mu_e$ ( $\text{cm}^2 \text{ V}^{-1} \text{ s}^{-1}$ )	1800	1350
Hole mobility $\mu_h$ ( $\text{cm}^2 \text{ V}^{-1} \text{ s}^{-1}$ )	1200	450
Breakdown field ( $\text{V cm}^{-1}$ )	$10^7$	$3 \times 10^5$
Resistivity ( $\Omega \text{ cm}$ )	$> 10^{11}$	$2.3 \times 10^5$
Intrinsic carrier density ( $\text{cm}^{-3}$ )	$< 10^3$	$1.5 \times 10^{10}$
Mass density ( $\text{g cm}^{-3}$ )	3.52	2.33
Atomic charge	6	14
Dielectric constant $\epsilon$	5.7	11.9
Displacement energy (eV/atom)	43	13 – 20
Energy to create an e-h pair (eV)	13	3.6
Radiation length (cm)	12.2	9.6
Avg. signal created/ $\mu\text{m}$ (e)	36	89

Table 2.1: Comparison diamond – silicon [?, 28].

## 2.1 Principles of signal formation in semiconductors

Particles can interact with the sensor in several ways, e.g. via bremsstrahlung [], elastic or inelastic scattering (e-h pair production) or nuclear reactions. Bremsstrahlung is radiation created when a particle is deflected from its original path due to attraction of the core of an atom. This is in principle an unwanted effect in semiconductors as it deteriorate the spatial resolution of the sensor. Elastic scattering is deflection of the particle's trajectory due to the pull from the nucleus without depositing any energy in it. Inelastic scattering is the interaction through which an atom is ionised and an electron-hole pair is created. All these effects are competing and are dependent on the particle's mass, momentum etc.

Semiconductors are materials with a conductance between that of insulators and that of metals – of the order of  $10^{?5} \Omega^{-1} \text{ cm}^{?1}$ . They can be made up of atoms with four electrons in their valence band (e.g. silicon–Si, carbon–C or germanium–Ge) or as combinations of two or more different materials (e.g. gallium arsenide–GaAs). The atoms in the lattice form valence bonds with adjacent atoms, making solid crystal structures. These bonds can break apart if sufficient external energy is deposited. The electron that was forming the bond is kicked out, leaving behind a positively charged ion with a vacancy – a hole – in its valence band, as shown in figure 2.1a. A free electron-hole pair is thus created. The free electron travels through the crystal until it is recombined with another hole. Similarly, the hole also “travels” through the material. Its positive charge attracts a bound electron in the vicinity, which breaks from the current bond and moves to the vacancy, leaving a new hole behind. The process continues, making it look like the hole is traveling through the material.

The electrons need to absorb a certain energy to get to get ionised. The minimal transferred energy required to excite an electron in a semiconductor is equal to the energy gap  $E_g$ . Typical widths of the forbidden gap are 0.7 eV in Ge, 1.12 eV in Si,

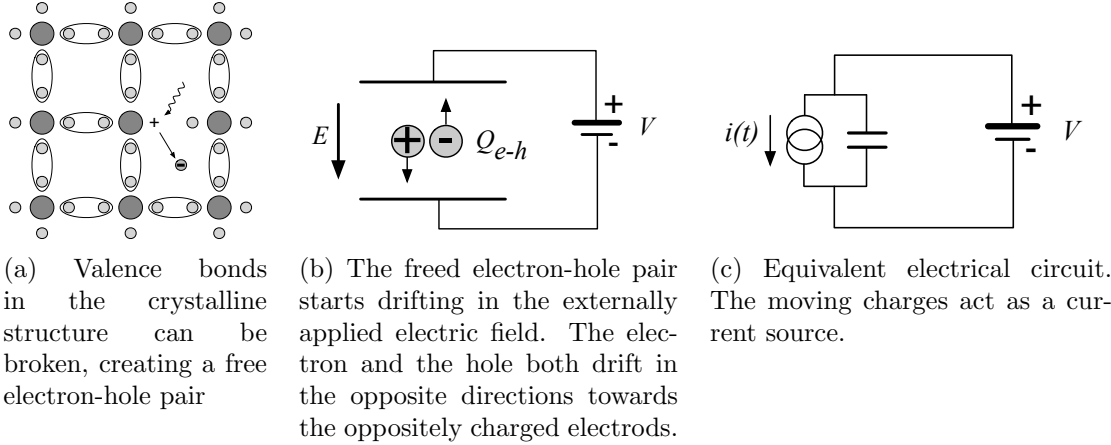


Figure 2.1: In the equivalent electrical circuit diagram the electron-hole creation and drift can be modelled as a current source with a capacitor in parallel.

655 1.4 eV in GaAs and 5.5 eV in diamond. Due to the small band gap in semiconductors  
 656 a significant amount of electrons already occupies the conduction band at room tem-  
 657 perature (RT) due to thermal excitation, according to the probabilistic distribution.  
 658 The intrinsic carrier concentration  $n_i$  in semiconductors is given as

$$n_i = T^{3/2} \cdot \exp\left(-\frac{E_g}{2k_B T}\right) \quad (2.1)$$

659 wherein  $k_B = 1.381 \times 10^{-23} \text{ m}^2 \text{ kg s}^{-2} \text{ K}^{-1}$  is the Boltzmann constant and  $T$  is the  
 660 temperature in K.

661 If an external electric field is applied to the crystalline structure, the free electrons  
 662 and holes drift toward the positive and negative potential, respectively, as shown in  
 663 figure 2.1b. While drifting, the charges couple with the electrodes, inducing current  
 664 in the circuit, which is explained by the Shockley–Ramo theorem below. The charges  
 665 recombine upon reaching the electrodes. The equivalent electrical circuit is shown in  
 666 figure 2.1c.

### 667 Energy deposition of $\alpha$ radiation and heavy ions

668 **Energy deposition of  $\beta$  and  $\gamma$  radiation** The mean energy loss of a particle travers-  
 669 ing the detector as a function of the momentum is given with the the Bethe-Bloch  
 670 equation []:

$$-\left\langle \frac{dE}{dx} \right\rangle = \frac{4\pi}{m_e c^2} \cdot \frac{n z^2}{\beta^2} \cdot \left( \frac{e^2}{4\pi\epsilon_0} \right)^2 \cdot \left( \ln \left( \frac{2m_e c^2 \beta^2}{I \cdot (1 - \beta^2)} \right) - \beta^2 \right) \quad (2.2)$$

671 The resulting function for a muon (a heavy electron) is shown in figure 2.2. At a  
 672 momentum of around 300 MeV/c the particle deposits the lowest amount of energy.  
 673 That is called a minimum ionising particle or a MIP.

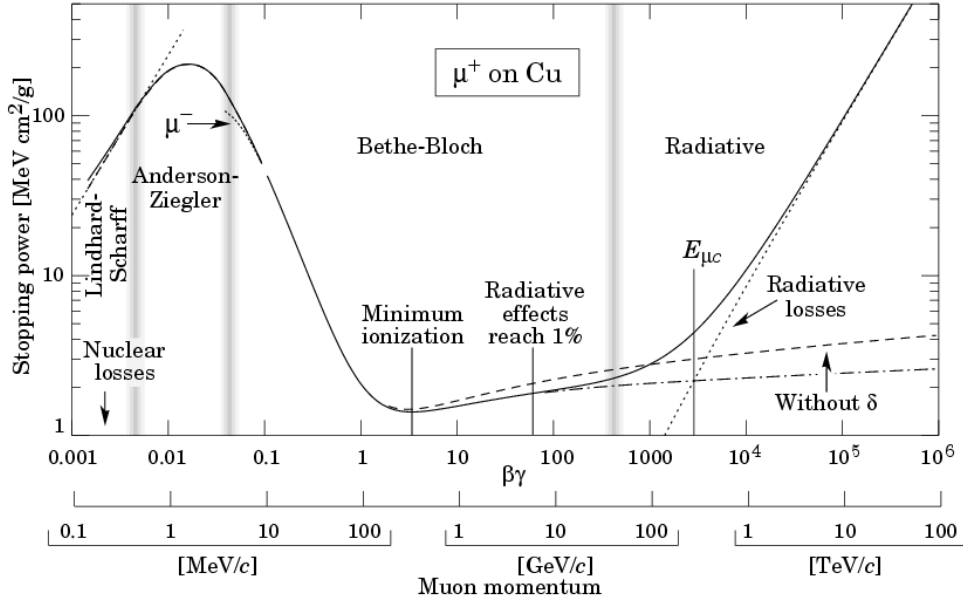


Figure 2.2: Stopping power for muons according to the Bethe-Bloch formula [].

### 674 2.1.1 Signal induction by moving charges

675 The book [17] gives a derivation of signal induction in a conducting plane by a point-  
 676 like charge, which couples with an electrode. The electrode can in this case be mod-  
 677 modelled as an infinite conducting plane. When a point charge  $q$  is created (e.g. an  
 678 electron-hole pair created via ionisation), its electrostatic field lines immediately cou-  
 679 ple with the electrode, as seen in figure 2.3a. The electric field on the metal surface  
 680 due to a point-like charge  $q$  at the distance  $z_0$  equals

$$E_z(x, y) = \frac{q z_0}{2\pi\epsilon_0(x^2 + y^2 + z_0^2)^{\frac{3}{2}}} \quad E_y = E_z = 0. \quad (2.3)$$

681 A mirror charge appears on the conducting plane, with a charge density distribution

$$\sigma(x, y) = \epsilon_0 E_z(x, y) = \frac{q z_0}{2\pi(x^2 + y^2 + z_0^2)^{\frac{3}{2}}}. \quad (2.4)$$

682 The charge density integrated over the entire plane yields a mirror charge  $Q$ , which  
 683 is an opposite of point charge  $q$ :

$$Q = \int_{-\infty}^{\infty} \int_{-\infty}^{\infty} \sigma(x, y) dx dy = -q. \quad (2.5)$$

684 The plane is segmented into infinitely long strips with a width  $w$  whereby each of  
 685 the strips is grounded (figure 2.3c). Considering a charge density distribution 2.4,  
 686 the resulting mirror charge on a single strip  $Q_2$  directly below the point charge ( $x =$   
 687  $0, y = 0$ ) yields

$$Q_2(z_0) = \int_{-\infty}^{\infty} \int_{-w/2}^{w/2} \sigma(x, y) dx dy = -\frac{2q}{\pi} \arctan\left(\frac{w}{2z_0}\right) \quad (2.6)$$

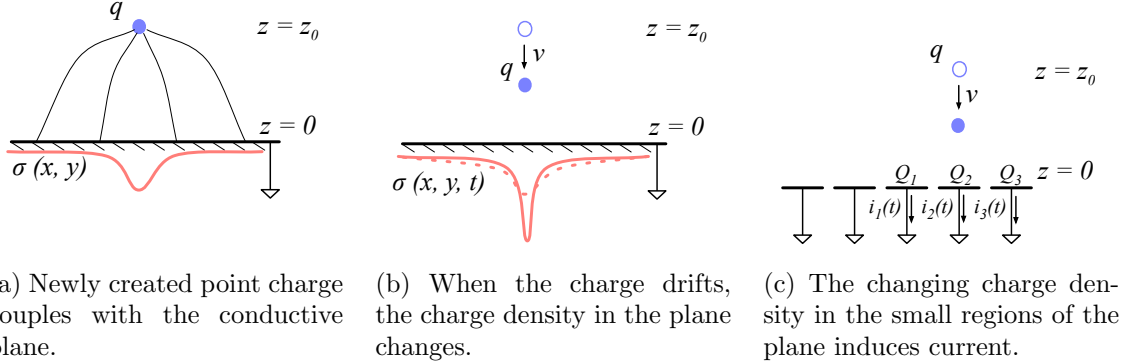


Figure 2.3: A point-like charge inducing current in a conductive plane.

If the charge starts moving towards the conducting plane, the mirror charge density distribution also changes, as shown in figure 2.3b. This results in the  $Q_2[z_0(t)]$  to change with time, inducing an electric current  $i_n(t)$ :

$$i_n(t) = -\frac{d}{dt}Q_2[z_0(t)] = -\frac{\partial Q_2[z_0(t)]}{\partial z_0} \frac{\partial z_0(t)}{\partial t} = \frac{4qw}{\pi[4z_0(t)^2 + w^2]}v. \quad (2.7)$$

The movement of the point-like charge therefore induces current in the conducting plane. The induced current is linearly dependent on the velocity of the point-like charge.

W. Shockley [42] and S. Ramo [40] independently proposed a theory which explains how a moving point charge induces current in a conductor. The Shockley-Ramo theorem can therefore be used to calculate the instantaneous electric current induced by the charge carrier or a group of charge carriers. It can be used for any number of electrodes. It states that the current  $I_n^{\text{ind}}(t)$  induced on the grounded electrode  $n$  by a point charge  $q$  moving along a trajectory  $\mathbf{x}(t)$  reads

$$I_n^{\text{ind}}(t) = -\frac{dQ_n(t)}{dt} = -\frac{q}{V_w} \nabla \Psi_n[\mathbf{x}(t)]v(t) = -\frac{q}{V_w} \mathbf{E}_n[\mathbf{x}(t)]v(t), \quad (2.8)$$

where  $\mathbf{E}_n(\mathbf{x})$  is the electric field in the case where the charge  $q$  is removed, electrode  $n$  is set to voltage  $V_w = 1$  and all other electrodes are grounded.  $\mathbf{E}_n(\mathbf{x})$  is also called the *weighting field* of electrode  $n$  and is defined as the spatial differential of the *weighting potential*:  $\mathbf{E}_n(\mathbf{x}) = \nabla \Psi_n(\mathbf{x})$ . In the case of two parallel electrodes, the weighting field is  $E_w = -\frac{d\Psi}{dx} = -1/d$ , where  $d$  is the distance between the electrodes. The resulting induced current is therefore

$$i(t) = \frac{q}{d}v_{\text{drift}}(x, t), \quad (2.9)$$

whereby  $v_{\text{drift}}$  is the drift velocity of the point-like charge and  $d$  is the distance between the electrodes.

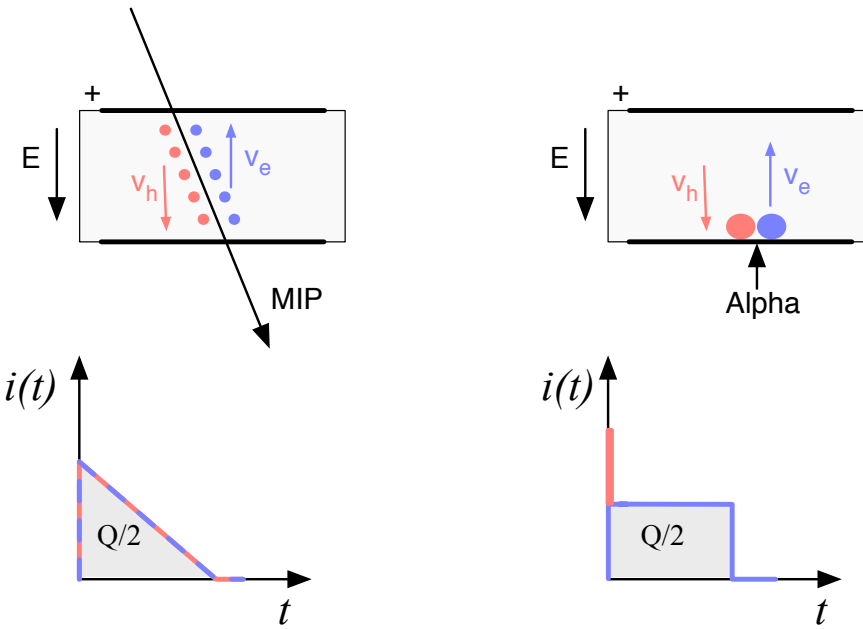


Figure 2.4: Charge carrier drift in diamond for  $\beta/\gamma$  and for  $\alpha$  particles.

### 2.1.2 Radiation-induced electrical pulses

When a highly-energetic particle travels through the sensor, it interacts with atoms in the lattice. It ionises the valence electrons, creating electron-hole (e-h) pairs on its way. It can either deposit only a fraction of its energy and fly exit the sensor on the other side or it can get stopped in the bulk, depositing all of its energy. A special case is when it interacts with the core of the atom in the middle of the sensor via a nuclear interaction. All these various types interactions produce different amounts and different spatial distributions of e-h pairs. The induced electrical current therefore differs for different types of interaction. Two most frequent types are shown in figure 2.4. The first diagram shows the interaction of a minimum ionising particle. The electrons and holes are created all along the trajectory of the particle and immediately start drifting towards the positive and negative electrode, respectively. At the beginning, all charges drift and contribute to the induced current. Those closest to the electrodes have a very short drift path and recombine quickly, reducing the induced current. Gradually all the charge carriers recombine. The resulting current signal is a triangular pulse with a sharp rising edge and a linear falling edge. The accumulated charge  $Q_s$  equals to the sum of the contributions of the positive and negative charge carriers. The second type of interaction happens when the particle is stopped in the diamond close to the point of entry. Most of its energy is deposited in a small volume close to the electrode. A cloud of charge carriers is created and the charges with the shorter path to the electrode recombine almost instantly. The carriers of the opposite charge, however, start drifting through the sensor to the other

730 electrode. In an ideal diamond sensor, their velocity is constant throughout the drift  
 731 up until they are collected at the opposite electrode. The contribution of the first  
 732 charge cloud is a peak with a short time. The cloud drifting through the sensor, on  
 733 the other hand, induces a current signal with a flat top. The resulting signal has a  
 734 shape of a rectangle, with a spike in the beginning. This spike is filtered out in a real  
 735 device because it is too fast for the electronics existing currently. The accumulated  
 736 charge  $Q_s$  is equal to a half of the deposited charge by the stopped particle.

737 The two aforementioned types of interactions have well defined signal responses.  
 738 Nuclear interactions on the other hand yield various results. The resulting signal  
 739 shape depends on the decay products of the interaction, which can be  $\alpha$ ,  $\beta$  or  $\gamma$   
 740 quanta, inducing a mixed shaped signal.

### 741 2.1.3 Signal charge fluctuations

742 Two important sensor properties are the magnitude of the signal and the fluctua-  
 743 tions of the signal at a given absorbed energy. They determine the relative resolution  
 744  $\Delta E/E$ . For semiconductors the signal fluctuations are smaller than the simple sta-  
 745 tistical variance  $\sigma_Q = \sqrt{N_Q}$ . Here  $N_Q$  is the number of released charge pairs, i.e.  
 746 the ratio between the total deposited energy  $E_0$  and the average energy deposition  $E_i$   
 747 required to produce an electron-hole pair. [] shows that the variance is  $\sigma_Q = \sqrt{FN_Q}$ ,  
 748 where  $F$  is the Fano factor [] (0.08 for diamond and 0.115 for silicon []). Thus, the  
 749 variance of the signal charge is smaller than expected,  $\sigma_Q \approx 0.3\sqrt{N_Q}$ . The resulting  
 750 intrinsic resolution of semiconductor detectors is

$$\Delta E_{FWHM} = 2.35\sqrt{FEE_i} \quad (2.10)$$

751 wherein  $E_i(Si) = 3.6$  eV and  $E_i(C) = 13$  eV. E.g., for an  $\alpha$  particle with energy  $E_\alpha$   
 752 = 5.486 MeV the calculated resolution in diamond is equal to  $\Delta E_{FWHM} = 5.6$  keV.  
 753 This defines the minimum achievable resolution for energy spectroscopy with semi-  
 754 conductors. Figure 2.5 shows the resolution limit as a function of energy in silicon  
 755 and diamond.

## 756 2.2 Carrier transport in a diamond sensor

757 This section describes the carrier transport phenomena in diamond. This theory  
 758 provides the basis for discussion about the measurements in chapter 3.

759 Free charge carriers in a semiconductor with no concentration gradient and with-  
 760 out an externally applied electric field get thermally excited and scatter in random  
 761 directions with a thermal velocity  $v_{th}$  []. Their integral movement due to thermal  
 762 excitation equals zero.

763 **Diffusion** Diffusion is caused by the concentration gradient. In its presence the in-  
 764 tegral movement is in the direction of the lower concentration until an equilibrium is  
 765 reached. The concentration profile dissolves with time forming a Gaussian distribu-  
 766 tion with variance  $\sigma(t) = \sqrt{Dt}$  [] .

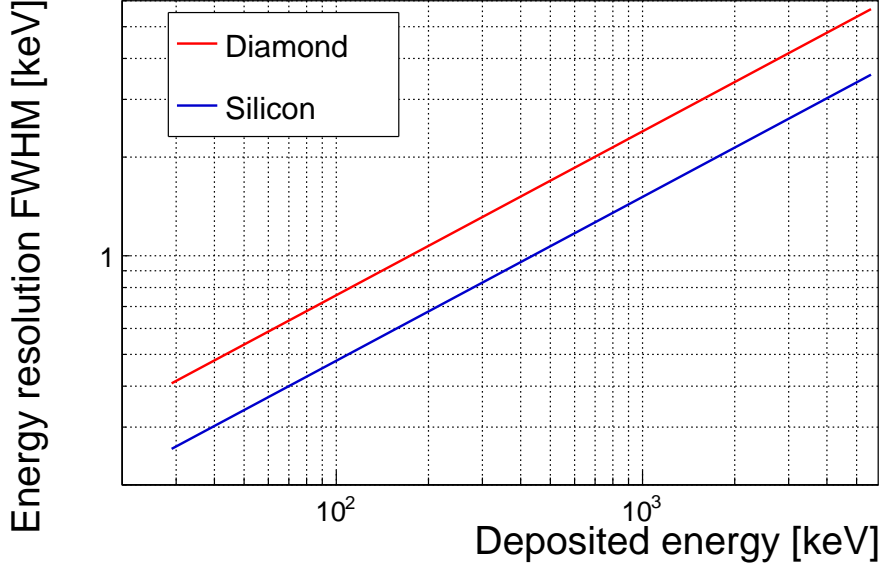


Figure 2.5: Calculated intrinsic energy resolution for silicon and diamond.

767 **Drift** Drift is caused by an externally applied electrical field. In that case the carriers move along the field lines. In a sensor with a high applied field the diffusion  
 768 contribution is negligible.  
 769

770 **Drift velocity, saturation velocity and mobility** The charge carriers drift through  
 771 the diamond bulk with a drift velocity  $v_{\text{drift}}(E)$  [], which is proportional to the electric  
 772 field  $E$  at low electric fields:  $v_{\text{drift}} = \mu E$ . The proportionality factor  $\mu$  is defined as  
 773 the mobility in  $\text{cm}^2 \text{V}^{-1} \text{s}^{-1}$ .

774 For higher fields, however, the velocity saturates as the carriers lose more energy to the  
 775 lattice at a higher velocity. They induce increasingly more lattice vibrations (phonon  
 776 transport). There is a velocity limit above which the carriers cannot reach – velocity  
 777 saturation. Paper [] defines this velocity to be  $v_{\text{sat}}^e = v_{\text{sat}}^h = (14.23 \pm 0.12) \times 10^6 \text{ cm/s}$   
 778 for both positive and negative charge carriers.

779 The final equation for  $v_{\text{drift}}$  is therefore

$$v_{\text{drift}}(E) = \mu(E)E = \frac{\mu_0 E}{1 + \frac{\mu_0 E}{v_{\text{sat}}}} \quad (2.11)$$

780 where  $\mu_0$  is the low field mobility and  $v_{\text{sat}}$  is saturation velocity. The drift velocity can  
 781 be retrieved experimentally via the transit time measured with the Transient Current  
 782 Technique (TCT). This technique enables the measurement of transit time  $t_t$  of the  
 783 carriers through the sensor with the thickness  $d$ .

$$v_{\text{drift}}(E) = \frac{d}{t_t(E)}. \quad (2.12)$$

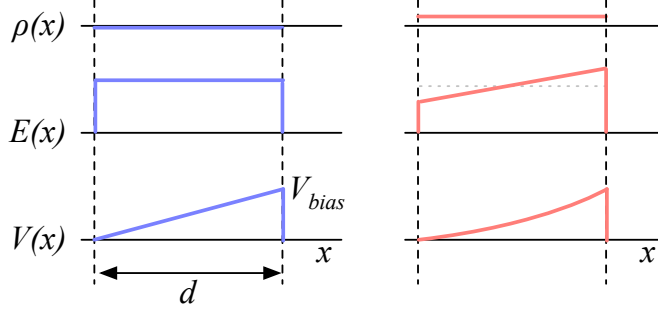


Figure 2.6: Left figure shows a profile of a diamond sensor only with an externally applied electric field. In the figure on the right a uniformly distributed space charge is added in the diamond, contributing to the internal electric field distribution. The induced current signal is proportional to the electrical field.  $d$  is the thickness of the diamond sensor.

784 The velocities for holes and electrons usually differ. In diamond, the holes travel  
 785 30 % faster than electrons []. The measurements in chapter 3 empirically confirm this  
 786 statement.

787 **Space charge** Poisson's equation shows that

$$\frac{d^2\Phi(x)}{dx^2} = \frac{dE(x)}{dx} = \frac{\rho(x)}{\epsilon} \quad (2.13)$$

788 where  $\rho(x)$  is the space charge distribution,  $E$  is the electrical field and  $\Phi$  is the  
 789 voltage potential. In an ideal diamond, the externally applied high voltage potential  
 790 on the two electrodes decreases linearly through the bulk. The electrical field is  
 791 therefore constant throughout the sensor and the space charge distribution across it  
 792 equals 0. However, space charge may be introduced in the bulk either by means of  
 793 accumulating of charge carriers in the lattice (i.e. charge trapping) or already during  
 794 sensor production. The space charge can be either permanent or changing – sometimes  
 795 it is possible to reduce it, as is shown in chapter 3. All in all, it is very important to  
 796 reduce it because it affects the shape of the electrical signal. Since the drift velocity  
 797 of the charge carriers is proportional to the electrical field, the charges change their  
 798 velocity while drifting through the space charge region. Figure 2.6 compares the  
 799 voltage potential, electrical field, space charge for an ideal sensor and for that with a  
 800 uniformly distributed positive space charge.

801 **Radiation damage** The bonds in the diamond lattice are very strong. However,  
 802 when highly energetic particles hit the diamond, they can damage the crystal struc-  
 803 ture. Figure 2.7 shows several examples of lattice damage:

- 804 a) foreign interstitial (e.g. H, Li),  
 805 b, c) foreign substitutional (e.g. N, P, B),

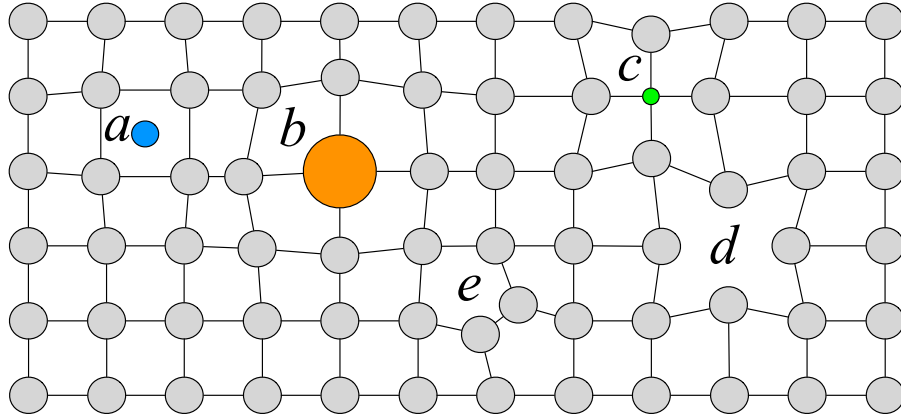


Figure 2.7: Impurities and non-uniformities in the crystal lattice due to radiation damage.

806 d) vacancy and

807 e) self interstitial.

808 These non-uniformities form new energy levels in the forbidden gap – the separation  
 809 between the conductive and valence band in which the electrons. These intermediate  
 810 levels are referred to as charge traps. The drifting charge carriers are stopped in these  
 811 traps. The energy level of the trapped carriers is reduced from the conduction band  
 812 to the energy level of the trap. Different types of lattice damage have different energy  
 813 levels. The carriers trapped in an energy level close to the conduction band have a  
 814 high probability of being thermally excited back into the conduction band whereby  
 815 they continue drifting towards the electrode. Their activation energy is therefore low.  
 816 Those trapped in a deep trap close to the middle of the forbidden gap need a much  
 817 higher activation energy, which in turn increases the average time to their release.

818 The trapped carriers do not contribute to the overall induced current on the elec-  
 819 trodes. The more charges are trapped along their drift path, the lower the induced  
 820 current.

## 821 2.3 Electronics for signal processing

822 This section describes the electronics of a detector, starting with a description of  
 823 signal amplifiers and then discussing the digitisation and signal processing. All these  
 824 stages are necessary to extract information from the sensor. First, the signal has to be  
 825 amplified. Then it is digitised and finally processed in a specially designed processor  
 826 or a logic unit.

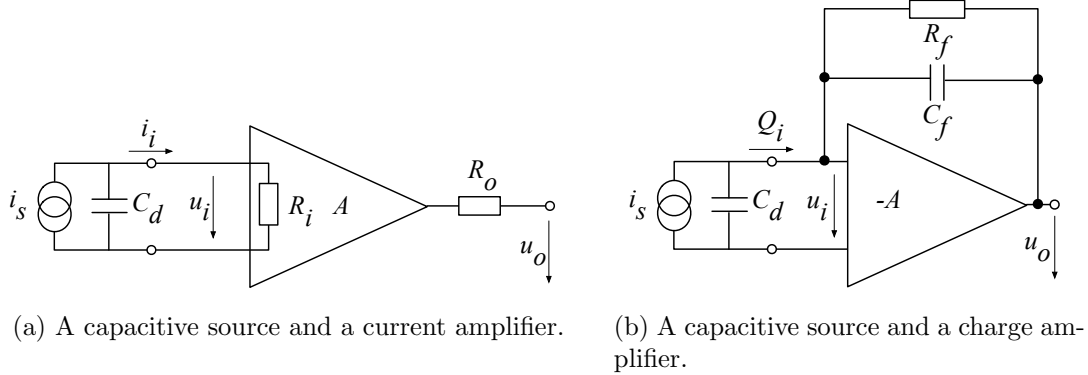


Figure 2.8: Simplified equivalent circuits of a current and charge amplifier.

### 827 2.3.1 Signal preamplifiers

828 The signal charge generated in the sensor by a single highly energetic particle or  
 829 photon is of the order of fC. The induced current is ranging between  $10^{-8}$  A ( $\beta, \gamma$   
 830 radiation) and  $3 \times 10^{-7}$  A ( $\alpha$  radiation). Signals as low as these have to be pre-  
 831 amplified before processing. Depending on the measurement, several types of signal  
 832 amplifiers can be used. The preamplifiers are designed to minimise electronic noise  
 833 while maximising gain, thus maximising the signal-to-noise ratio (SNR). In addition, a  
 834 high bandwidth limit is preferred to minimise the information loss due to signal shape  
 835 deformation. A critical parameter is the total capacitance, i.e. the sensor capacitance  
 836 together with the input capacitance of the preamplifier. The SNR improves with a  
 837 lower capacitance. Several types of amplifiers can be used, all of which affect the  
 838 measured pulse shape. They behave differently for resistive or capacitive sources.  
 839 This thesis focuses on semiconductors as capacitive sources. Two preamplifiers are  
 840 used most commonly, a current and a charge amplifier. Both are described below in  
 841 detail.

#### 842 2.3.1.1 Current-sensitive amplifier

843 Figure 2.8a shows the equivalent circuit of a capacitive source and a current amplifi-  
 844 er. An amplifier operates in current mode if the source has a low charge collection  
 845 time  $t_c$  with respect to the  $R_i C_d$  time constant of the circuit. In this case the sensor  
 846 capacitance discharges rapidly and the output current  $i_o$  is proportional to the in-  
 847 stantaneous current  $i_i$ . The amplifier is providing a voltage gain, so the output signal  
 848 voltage  $u_o$  is directly proportional to the input voltage  $u_i$ :

$$u_o(t) = A \cdot R_i \cdot i_s(t). \quad (2.14)$$

849 The detector capacitance  $C_{det}$  together with the input resistance of the amplifier  $R_i$   
 850 defines the time constant of the signal, as shown in figure 2.9. The higher the  $C_{det}$ ,  
 851 the slower is the response of the amplifier. For the case of the diamond sensor, which

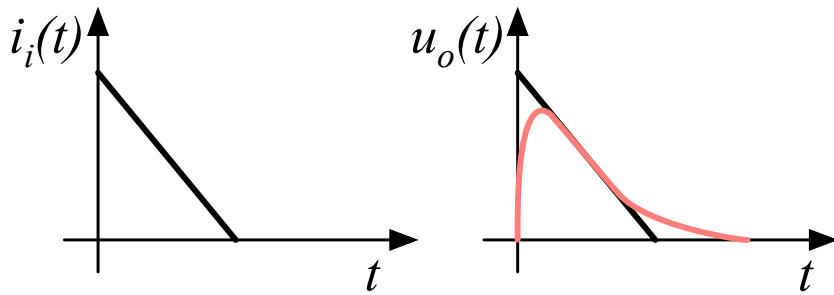


Figure 2.9: Input and output signal of the current amplifier.

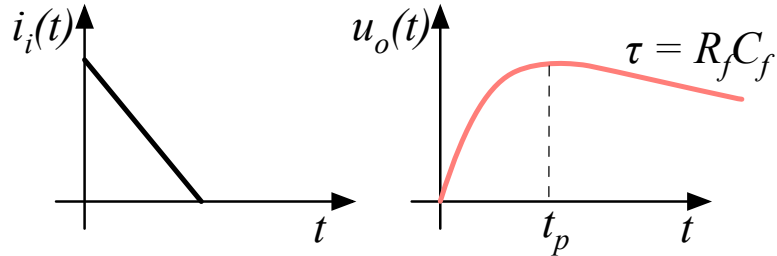


Figure 2.10: Input and output signal of the charge amplifier.

852 has the capacitance of the order of 2 pF and the input resistance of  $50 \Omega$ , the resulting  
 853 time constant is  $\tau = 10^{-10}$  s. This yields the signal rise time  $t_r \sim 2.2\tau = 2.2 \times 10^{-10}$  s.  
 854

### 855 2.3.1.2 Charge-sensitive amplifier

856 In order to measure integrated charge in the sensor, a feedback loop is added to the  
 857 amplifier, as shown in figure 2.8b. The feedback can be used to control the gain and  
 858 input resistance, as well as to integrate the input signal. The charge amplifier is in  
 859 principle an inverting voltage amplifier with a high input resistance.

860 In an ideal amplifier the output voltage  $u_o$  equals  $-Au_i$ . Therefore the voltage  
 861 difference across the capacitor  $C_f$  is  $u_f = (A + 1)u_i$  and the charge deposited on the  
 862 capacitor is  $Q_f = C_f u_f = C_f(A + 1)u_i$ . Since no current can flow into the amplifier,  
 863 all of the signal current must charge up the feedback capacitance, so  $Q_f = Q_i$ .

864 In reality, however, charge-sensitive amplifiers respond much slower than is the  
 865 duration of the current pulse from the sensor. In addition, a resistor is added to the  
 866 feedback line in parallel to the capacitor. The resistor and capacitor define the decay  
 867 time constant of the pulse, as shown in figure 2.10. This is necessary to return the  
 868 signal to its initial state and ready for a new measurement.

869 **2.3.1.3 Analogue electronic noise**

870 Electronic noise determines the ability of a system to distinguish signal levels. The  
 871 analogue signal contains a lot of information, which can quickly be erased or altered  
 872 if the signal properties change. It is therefore instrumental to understand the noise  
 873 contributions to the signal to qualify the information it carries. There are several  
 874 noise contributions, of which the important ones are listed below. The thermal noise  
 875 is the dominant noise contribution in the use case for diamond detector signal ampli-  
 876 fication and therefore defines the limitations of the detector system. Thermal noise  
 877 or Johnson–Nyquist [] noise is generated by the random thermal motion of charge  
 878 carriers in the conductor. The frequency range of the thermal noise is from 0 to  
 879  $\infty$  with a more or less uniform distribution. Therefore this is nearly a white noise.  
 880 The resulting signal amplitude has a Gaussian distribution. The RMS of the noise  
 881 amplitude is defined as

$$u_{\text{RMS}} = \sqrt{4k_B RT \Delta f} \quad (2.15)$$

882 where  $k_B$  is the Boltzmann constant,  $R$  is the input resistance of the amplifier,  $T$  its  
 883 temperature and  $\Delta f$  the frequency range. This equation shows that it is possible to  
 884 reduce the noise RMS by either (1) reducing the frequency range, (2) reducing the  
 885 resistance of the conductor or (3) cooling the conductor.

886 Contributions of shot noise, flicker noise and burst noise and other types are not  
 887 significant relative to the thermal noise. However, the contributions of external factors  
 888 can severely deteriorate the signal. This means the noise produced by capacitive or  
 889 inductive coupling with an external source, which causes interference in the signal.  
 890 These effects can be reduced by shielding the electronics and avoiding ground loops.

891 **2.3.2 Analogue-to-digital converters**

892 An analogue-to-digital converter (ADC) is a device that converts the analogue elec-  
 893 trical signal on the input to its digital representation - a series of digital values. This  
 894 involves a quantisation – *sampling* of the signal at a defined sampling period, resulting  
 895 in a sequence of samples at a discrete time period and with discrete amplitude values.  
 896 The resolution of the ADC is the number of output levels the ADC can quantise to  
 897 and is expressed in bits. For instance, an ADC with a resolution equal to  $n = 8$  bit  
 898 has a dynamic range of  $N = 2^n = 256$  steps. The resulting voltage resolution  $Q_{\text{ADC}}$   
 899 at the input voltage range of  $V_{\text{ADC}} = \pm 50$  mV is then equal to

$$Q_{\text{ADC}} = \frac{V_{\text{ADC}}}{2^n} = \frac{100 \text{ mV}}{2^8 \text{ bit}} = 0.39 \text{ mV/bit.} \quad (2.16)$$

900 With a sampling period of  $t_s = 1$  ns the sampling rate is  $f_s = 1$  GSPS (gigasample per  
 901 second).

902 **Quantisation error and quantisation noise** (or a round-off error) is a contribu-  
 903 tion to the overall measurement error due to digitisation (rounding). It is defined as  
 904 a difference between the actual analog value and the closest digitised representation

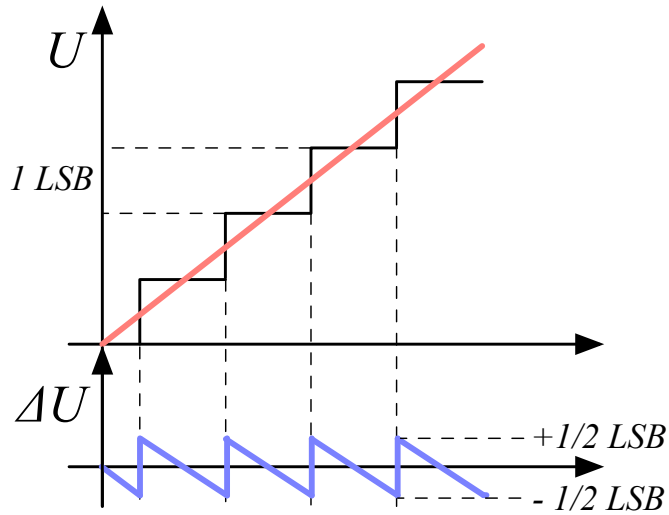


Figure 2.11: Input signal digitisation and quantisation error.

of this value. The error is defined by the least significant bit (LSB), as seen in figure 2.11. Typically, the input signal amplitude is much larger than the voltage resolution. Therefore the quantisation error is not directly correlated with the signal and has an approximately uniform distribution []:

$$\Delta Q_{\text{ADC}} = \frac{1}{\sqrt{12}} \text{ LSB} \sim 0.289 \text{ LSB.} \quad (2.17)$$

For the example above the quantisation error equals  $\Delta Q_{\text{ADC}} = 0.289 \cdot 0.39 \text{ mV} = 0.11 \text{ mV}$ . The error depends strongly on the linearity of the ADC, but this is out of scope of this document as the devices used have ADCs with a linear response.

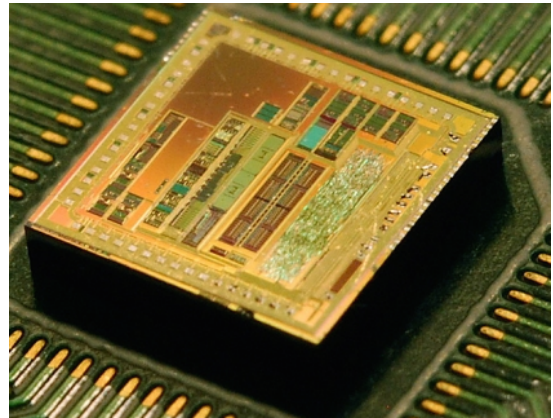
### 2.3.3 Digital signal processing

The digitised signal can be processed to extract useful information. Therefore after the signal amplification and digitisation the signal is routed in a device which handles the digital analysis. The signal can either be processed immediately (in real time) or it can be saved to a data storage for analysis at a later stage (offline). The devices carrying out the processing can be multipurpose (e.g. Field Programmable Gate Arrays) or dedicated (e.g. Application-Specific Integrated Circuits).

**Field Programmable Gate Array** (FPGA) is an integrated circuit designed to be reprogrammable and reconfigured after manufacturing. It consists of a set of logic gates that can be interconnected in numerous combinations to carry out a set of logic operations. Many such logic operations can take place in parallel, making the FPGA a powerful tool for signal processing. FPGAs are often used during system



(a) Xilinx Virtex 5 FPGA [13].



(b) ASIC [1].

Figure 2.12: An example of an FPGA and an ASIC chip.

development or in systems in which the requirements might change with time. They can be reprogrammed in the order of seconds. In addition, the logic design only needs minor changes when migrating to a newer version of the FPGA chip of the same vendor. The FPGAs also offer faster time-to-market with comparison to application-specific solutions, which have to be developed. On the other hand, the price per part can be significantly higher than for the application-specific solutions. Also, their other major disadvantages are a high power consumption and a relatively low speed as compared to more application-specific solutions. However, today's solutions are capable of clock speeds higher than 500 MHz. Together with the integrated digital signal processing blocks, embedded processors and other modules, they are already very powerful and versatile. All in all, FPGAs are a good choice for prototyping and limited production, for projects with limited requirements for speed and complexity.

**Application-Specific Integrated Circuit** (ASIC) is an integrated circuit designed for a specific use. The design cannot be modified after chip production, as is the case with FPGAs. On the other hand, the ASICs can be optimised to perform a required operation at a high speed and at a low power consumption. In addition, due to the specific design the size of the chip can be much smaller. ASICs can be designed as hybrid chips, containing both a digital and an analog part. To update the chip, the design has to be submitted to a foundry, which produces the new chips with a turnover time of 4–6 weeks. The costs of a submission start at \$ 50 000, but the price per part can be reduced significantly with a high volume. To sum up, ASICs are used for high volume designs with well defined requirements where some stringent constraints in terms of power consumption and speed have to be met.

947

# Chapter 3

948

## Experimental results

949

### *Diamond irradiation study*

950 This chapter contains the measurement results of data taken with diamond sensors.  
951 First the measurement setup is described (section 3.1). Then the measured particle  
952 spectra are shown in 3.2. This is followed by a study of effects of irradiation damage  
953 on the electrical signal of the diamond detector and its lifetime. The last section  
954 shows the results of the measurements of irradiated diamond samples at cryogenic  
955 temperatures. The aim of these studies is to find the operational limitations of dia-  
956 mond detectors for spectroscopy and tracking applications. The studies compare the  
957 experimentally acquired data with the theory from the previous chapter and define  
958 limitations of the diamond detectors in terms of noise, radiation and temperature.

959 Diamond sensors are mainly used for two types of measurements: particle counting  
960 and spectroscopy. The first type of measurements depends on the sensor efficiency –  
961 its ability to detect all or at least a known percentage of incident particles. The energy  
962 of the particles is not so important; what bears the information is the rate and the  
963 spatial distribution. Here the particles do not necessarily stop in the bulk, but rather  
964 continue their way. In spectroscopy, on the other hand, the particles stop within the  
965 sensor, depositing all their energy. This energy is then measured by collecting the  
966 freed charge carriers. The aim of the experiments described in this chapter is to:

- 967 1. Quantify the efficiency of the sCVD diamond in counting mode,
- 968 2. Quantify the degradation of efficiency as a function of the received radiation  
dose,
- 970 3. Quantify the macroscopic effects on charge carrier behaviour as a function of  
the received radiation dose and
- 972 4. Define limitations for use in spectroscopy.

973 The results discussed here show that there are several limitations for using diamond  
974 as a measurement device. All of them need to be taken into account when designing  
975 a new measurement device. The first step is to build a setup that is insensitive to

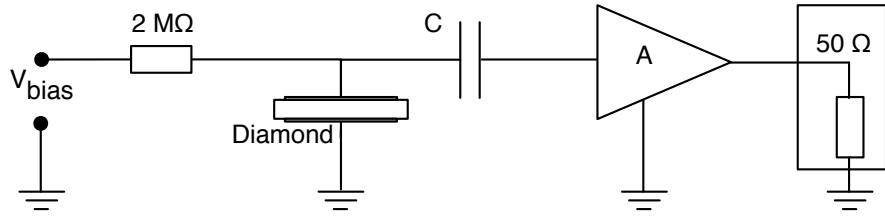


Figure 3.1: Diagram of a diamond detector readout chain.

976 external electromagnetic interferences and minimises electrical noise in the system.  
 977 The setup needs to be calibrated before use. Then the measurement conditions have to  
 978 be defined, such as the temperature, the type of radiation and its flux. This allows for  
 979 an estimation of the lifetime of the detector and a prediction of the longterm signal  
 980 degradation as a function of the dose. The degraded signal can then be corrected  
 981 during data analysis.

## 982 3.1 Measurement setup

983 A measurement setup has to be designed to minimise noise. Shielding has to be  
 984 applied wherever possible. For instance, aluminium foil can be wrapped around  
 985 the exposed parts of the system to shield them from external radio-frequency (RF)  
 986 interferences. In addition, the sensors have to be covered to prevent the light from  
 987 shining directly onto them. The incident photons can deposit enough energy to  
 988 increase the leakage current of the detector, which produces unwanted results.

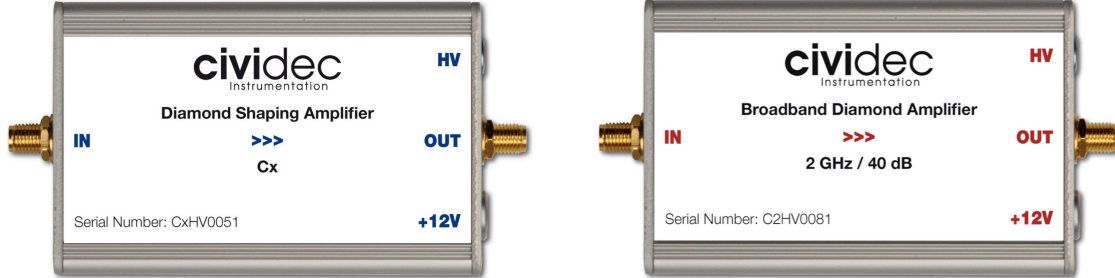
989 The measurements using diamond that are explained in these chapters have been  
 990 carried out using several measurement setups, but they are all similar in terms of  
 991 the electrical signal chain. The measurement chain consists of three main parts: a  
 992 diamond sensor, a signal preamplifier and a readout device, as seen in figure 3.1. The  
 993 signals propagating along the analogue chain are fast – in the GHz bandwidth range  
 994 – and with low amplitudes – of the order of tens of  $\mu\text{V}$ . This gives rise to importance  
 995 of RF shielding. Also, the connection between the carrier and the preamplifier has  
 996 to be as short as possible to avoid capacitive signal losses in the transmission line.  
 997 Finally, the system needs to be grounded properly.

### 998 3.1.1 Preamplifiers

999 Two preamplifiers are used for the measurements, one sensitive to charge and the  
 1000 other to current. *CIVIDEC Cx* (figure 3.2a) is a charge sensitive amplifier. Its high  
 1001 SNR due to a low equivalent noise charge of  $300 + 30 \text{ pF}^{-1} \text{ e}^-$  and a reported gain  
 1002 of  $\sim 12 \text{ mV/fC}$  makes it a good choice for spectroscopic measurements with diamond  
 1003 sensors. *CIVIDEC C2* (figure 3.2b) is a fast current preamplifier with a 2 GHz  
 1004 bandwidth limit. It is used for TCT measurements because if its fast response and

### 3.1. MEASUREMENT SETUP

---



(a) Cx charge sensitive preamplifier.

(b) C2 fast charge preamplifier.

Figure 3.2: Amplifiers used for the charge and current measurements.

1005 a good SNR. Both are embedded in an RF-tight aluminium box to reduce the noise  
1006 pickup. Both have an AC coupled input and an output with a  $50\ \Omega$  termination.

#### 1007 3.1.1.1 Calibration

1008 The amplifiers have to be calibrated before use to determine their gain. Both are  
1009 calibrated using a square signal generator with a known amplitude step of  $U_{in} =$   
1010  $(252 \pm 5)$  mV. A 2 GHz oscilloscope with a 10 GS/s sampling is used to carry out  
1011 these measurements.

1012 In the case of the Cx charge sensitive amplifier, the signal is routed through a  
1013 capacitor with a calibration capacitance  $C_{cal} = (0.717 \pm 0.014)$  pF and then to the  
1014 input of the amplifier. The pulse area behind the capacitor is  $a_{cal} = (5.0 \pm 0.5)$  pVs,  
1015 with the signal amplitude on the output amounting to  $U_{Cx} = (1.95 \pm 0.05)$  V. The  
1016 input voltage step combined with the calibration capacitance yields a calibration  
1017 charge  $Q_{cal} = C_{cal} \cdot U_{in} = (181 \pm 5)$  fC. The gain of the Cx amplifier is therefore  
1018  $A_{Cx}^Q = \frac{U_{Cx}}{Q_{cal}} = (9.3 \pm 0.4)$  mV/fC or  $A_{Cx}^a = \frac{U_{Cx}}{a_{cal}} = (390 \pm 40)$  mV/pVs. The area-based  
1019 amplification factor has a higher uncertainty ( $\sim 10\%$ ) than the amplitude-based  
1020 factor ( $\sim 4\%$ ) due to the measurement limitations of the oscilloscope. Nevertheless,  
1021 it can be used as an estimate for the integrated charge of a current pulse.

1022 To calibrate the C2 current amplifier, only the amplitude gain has to be measured.  
1023 The input signal amplitude has to be such that it keeps the output amplitude within  
1024 the amplifier's linear range, that is  $\pm 1$  V. The signal from the generator is therefore  
1025 routed through a 36 dB attenuator to decrease its amplitude to  $U_{inAtt} = (3.95 \pm$   
1026  $0.05)$  mV. Two amplifiers with different gains have been measured, because both are  
1027 used for the measurements. The output of the first amplifier amounts to  $U_{C2-1} =$   
1028  $(860 \pm 5)$  mV. This yields the amplification gain equal to  $A_{C2-1} = \frac{U_{inAtt}}{U_{C2-1}} = (217 \pm 3)$ .  
1029 The second amplifier has the output equal to  $U_{C2-2} = (632 \pm 5)$  mV with the resulting  
1030 gain of  $A_{C2-2} = (152 \pm 3)$ .

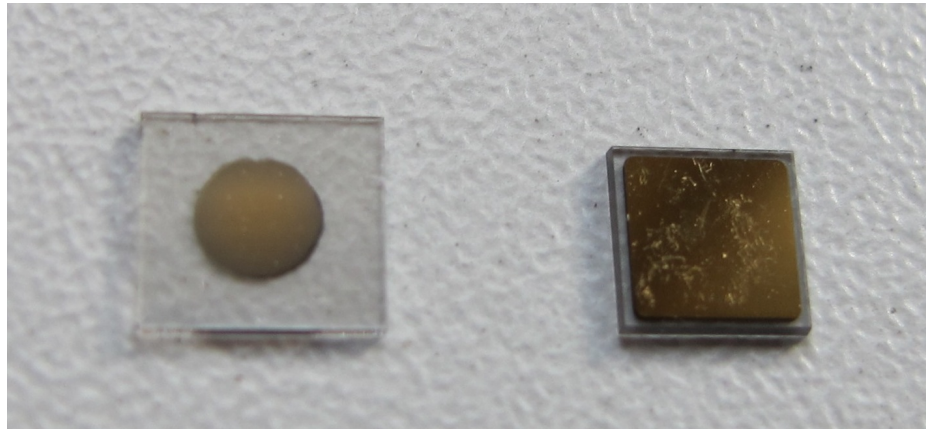


Figure 3.3: Two scCVD diamond samples: A IIa 1scdhq (left) and an E6 S37 (right).

### 3.1.2 Diamond samples

Detector-grade diamonds are very difficult to produce, mostly because it is very difficult to ensure a high enough purity of the lattice. The sensor samples used for these studies have been bought at Element Six (E6) [5]. They all have the same standard dimensions. sCVD diamonds with dimensions  $4.7 \times 4.7 \text{ mm}^2$  are already sufficiently large for most of the beam monitoring applications and still affordable. One of the samples with dimensions of  $5.6 \times 5.3 \text{ mm}^2$  produced by IIa Singapore [7] has also been sent to CERN to be characterised. The target thickness for all the samples is  $500 \mu\text{m}$ . Diamonds this thick yield a high enough signal-to-noise ratio for MIPs to be measured by the available electronics. Table 3.1 shows all the samples used for this study. Two of them are measured before and after irradiation with 300 MeV pions and then compared. Irradiation doses for damaging the material need to be high – above  $10^{12}$  particles per  $\text{cm}^2$  to be able to observe a significant change in behaviour of a diamond sensor.

1045	Name	Type	Producer	Dimensions [ $\text{mm}^2$ ]	Thickness [ $\mu\text{m}$ ]	Electrode	Irradiated
	S37	sCVD	E6	$4.7 \times 4.7$	548	Cr/Au	no
	S50	sCVD	E6	$4.7 \times 4.7$	537	Cr/Au	no
1046	S52	sCVD	E6	$4.7 \times 4.7$	515	Cr/Au	$1 \times 10^{14} \pi \text{ cm}^{-2}$
	S79	sCVD	E6	$4.7 \times 4.7$	529	Cr/Au	$3.63 \times 10^{14} \pi \text{ cm}^{-2}$
	ELSC	sCVD	E6	$4.7 \times 4.7$	491	Cr/Au	no
	1scdhq	sCVD	IIa	$5.6 \times 5.3$	460	Cr/Au	no

Table 3.1: Diamond sensor samples used.

The diamond samples have quoted impurity densities of  $\leq 2 \times 10^{14} \text{ cm}^{-3}$  and nitrogen incorporation of  $\leq 1 \text{ ppb}$ . The electrodes were added by various companies and institutes. For instance, S52 was metallised by a company DDL (now defunct) while the Physics Department of the University of Firenze, Italy metallised the S79. There are also several techniques for producing the electrodes. The DDL contacts

### **3.1. MEASUREMENT SETUP**

---

1053 consist of three layers: DLC (diamond-like carbon)/Pt/Au with 4/10/200 nm thick-  
1054 nesses, respectively. The metallisation for S79, on the other hand, is made up of  
1055 Cr/Au with a total thickness of  $\sim$ 400 nm. The area coverage also differs from sample  
1056 to sample. Diamonds must not be metallised until the very edge as the proximity of  
1057 contacts with a high potential may lead to sparking. However, the areas not covered  
1058 by the metallisation are less efficient because the fringe fields at the edges are not  
1059 as strong as in between the electrodes. This effectively reduces the sensitive area of  
1060 the sensors. In the diamonds used here the effective area is anywhere from 9 mm<sup>2</sup> to  
1061 18 mm<sup>2</sup>. The leakage current through the bulk is below 1 ns, but increases for the  
1062 irradiated samples. The capacitance is of the order of (2.0 $\pm$ 0.3) pF.

#### **1063 3.1.3 Readout devices**

1064 Electrical signals in diamond detectors are in the GHz frequency range. To preserve  
1065 the information in the signals, the readout device with a high bandwidth limit must  
1066 be used. For instance, a 250 MHz limit is enough for the spectroscopic measurements  
1067 with the Cx charge amplifier, but might be insufficient for the current measurements  
1068 with the C2 amplifier.

1069 Two devices are used take data shown in this chapter. The first choice is a 2 GHz  
1070 LeCroy WaveRunner 204MXi-A. This specific model has a sufficiently high bandwidth  
1071 limit for the fast current preamplifier signals. It offers a versatile solution for analogue  
1072 signal readout – fast to set up and reliable, hence convenient for use in laboratory tests  
1073 and for experiments where limited amounts of data are taken and where speed is not  
1074 crucial. However, its slow acquisition speed is a bottleneck in a test beam experiment.  
1075 Its initial 100 Hz readout rate decreases to a mere 20 Hz within 20 minutes, because  
1076 every single trigger is saved as a separate file and the Windows operating system  
1077 is not capable of handling 10000+ files in a single directory easily. This is why it  
1078 has been exchanged with a DRS4 [4], an analogue readout device developed by PSI,  
1079 Switzerland. This compact device is capable of recording up to four waveforms at a  
1080 time at a steady rate of up to 500 Hz. Its 700 MHz bandwidth limitation is sufficient  
1081 for the signal from the charge amplifier.

#### **1082 3.1.4 Setup for the efficiency study using $\beta$ particles**

1083 The efficiency study of the diamond sensors has been carried out at CERN in the  
1084 North Hall test beam facility. There a straight high-energy particle beam of  $\pi_{120}$  GeV is  
1085 provided to the users to calibrate their detectors. The beam has a transverse spread  
1086 of  $\sigma = 10$  mm in both axes. The particle rate is of the order of  $10^4 \pi \text{ cm}^{-2} \text{ s}^{-1}$ .  
1087 A diamond sensor embedded in a PCB carrier has been placed in the beam spot  
1088 perpendicular to the beam and connected via an SMA connector directly to a charge  
1089 amplifier. The amplified signal is read out using a LeCroy oscilloscope and a DRS4  
1090 analogue readout system. A computer is used as a controller and data storage for  
1091 the readout device. A beam telescope is used as a reference detector. It is a device

that helps to cross-check the measurements of the devices under test (DUTs) and to carry out spatially resolved studies on the DUTs. It consists of several pixellated sensor planes placed in series, which can track a particle's trajectory with a precision of a few  $\mu\text{m}$ . The sensor planes are positioned in front of the DUT and behind it. Then the beam telescope acts as a trigger system – it triggers the readout of both the telescope data and DUT data when both the planes in front and behind the DUT record a hit by an incident particle. A particle detected by all the planes within the DUT window and the DUT itself counts towards its efficiency whereas a hit missed by the DUT means that the DUT is not 100 % efficient. To discard the hits that miss the DUT completely, a region of interest (ROI) can be chosen in the beam telescope planes. The equation for calculating the sensor efficiency is therefore

$$\epsilon = \frac{N_{\text{DUT}} \wedge N_{\text{telescope}}}{N_{\text{telescope}}} \quad (3.1)$$

for an ROI smaller than the sensitive region of the diamond.

### 3.1.5 Room temperature $\alpha$ -TCT setup

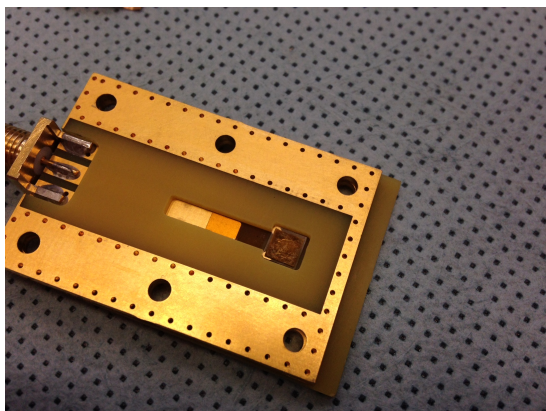
This TCT study is a follow-up of an extensive diamond TCT study at cryogenic temperatures [28]. The room-temperature TCT measurements have been carried out in the laboratory. The setup consists of a diamond sensor embedded in a PCB carrier, a current amplifier and an oscilloscope. To measure  $\alpha$  particles, their energy loss during their trajectory has to be minimised. Therefore the diamond is placed inside a vacuum chamber. The chamber is a steel tube with a diameter of 5 cm. On one side it is connected to a vacuum pump via a steel hose. A feedthrough with an SMA connector is placed on the other side. A C2 current amplifier is connected directly onto the feedthrough. The amplified output is connected to the oscilloscope via an SMA cable. An  $^{241}\text{Am}$  source with a diameter of 2 cm and a height of 0.5 cm is fixed onto the sensor carrier (figure 3.4a, figure 3.4b). Then the carrier is inserted in the chamber and fixed in place using an air-tight clamp. The pump can then be switched on. It is capable of providing the inside pressure as low as  $10^{-4}$  mbar after approximately one hour of operation, but measurements can take place even after five minutes of evacuation, at around  $10^{-3}$  mbar. The most important thing is to switch the bias voltage of the sensor OFF during the process of evacuation. This is due to gas becoming more conductive at the pressure of the order of  $10^{-1}$  mbar, which is at the bottom of Paschen's curve [21]. A failure to switch the bias voltage off may cause a spark between the signal and ground line, destroying the amplifier.

### 3.1.6 Cryogenic $\alpha$ -TCT setup

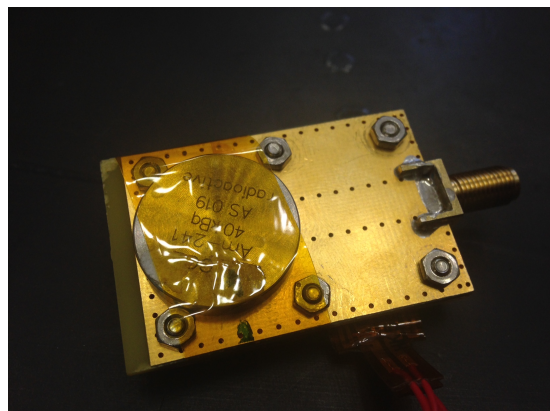
The experiment at cryogenic temperatures has been carried out in the Cryolab at CERN. The room-temperature TCT setup has to be modified to allow for measurements at temperatures as low as 2 K. It consists of three parts:

### 3.1. MEASUREMENT SETUP

---



(a) PCB carrier with an embedded diamond sample.



(b) Radioactive source over the carrier.

Figure 3.4: Positioning of the  $\alpha$ -source on top of the sensor carrier.

- 1128 1. a cryostat – a thermally insulated cylinder containing liquid helium,
- 1129 2. an inlet – an air-tight mechanical tube with valves and feedthroughs at the top  
1130 that is lowered in the liquid helium and
- 1131 3. the diamond sample embedded in a PCB carrier with a fitted temperature  
1132 sensor, a heater and cables leading to the feedthroughs.

1133 The setup is described in detail in [28].

1134 When the diamond sample is placed in the PCB carrier and the  $^{241}\text{Am}$  source is in  
1135 place, the inlet is sealed and lowered in the empty cryostat. Then the inside volume  
1136 of the inlet is evacuated down to  $10^{-5}$  mbar while the liquid helium is flowing into  
1137 the cryostat. To improve the thermal contact between the diamond and the coolant,  
1138 a small amount of helium gas is added inside the evacuated inlet, setting the vacuum  
1139 to around  $10^{-3}$  mbar. This value changes with time, because the gas condenses on  
1140 the walls of the inlet, reducing the number of floating particles. For this reason the  
1141 helium gas has to be added on an irregular basis. Every addition causes a significant  
1142 undershoot of the sample temperature, which has to be corrected for using a heater  
1143 placed on the back of the PCB carrier. Also, the added gas deteriorates the vacuum  
1144 inside the inlet. It is very important to monitor the pressure so as not to let it rise  
1145 above  $10^{-2}$  mbar. The gas at this pressure is significantly more conductive and can  
1146 cause a short circuit between the two diamond plates or in the SMA connectors,  
1147 destroying the amplifier. Furthermore, at approximately 60 K the helium gas has to  
1148 be evacuated from the inlet to avoid a potential explosion due to the expansion of  
1149 the gas with temperature.

1150 When the sample is cooled to the minimum temperature achievable by means of  
1151 liquid helium without over-pressurising it (4.2 K), the measurements can begin. A  
1152 temperature sensor placed on the back of the PCB carrier is used to measure the  
1153 temperature of the sample. After every temperature data point, the current through

the heater placed in the PCB next to the diamond sample is increased, increasing the sample. The initial temperature time constant of the order of tenths of seconds at low temperatures increases with temperature. Even more so when helium is evacuated from the inlet at 60 K, removing the thermal bridge between the wall of the inlet and the diamond sample. At the room temperature (RT), the time constant is already of the order of minutes.

## 3.2 Charged particle pulses and spectra

In previous chapter the ionisation profiles for different types of radiation were discussed. It is known that  $\beta$  and  $\gamma$  radiation induces a triangular electric pulse whereas  $\alpha$  radiation induces a rectangular one. However, their amplitude, width and rise/fall time depend heavily on the type of interaction with the diamond, the purity of the diamond and the bandwidth of the amplifier and the oscilloscope. This section shows the signal pulses of  $\alpha$ ,  $\beta$  and  $\gamma$  radiation with their respective energy distributions for the case of a diamond detector. This is followed by a discussion of effects of noise on these measurements.

A CIVIDEC C2 current amplifier together with the LeCroy oscilloscope (both with a bandwidth limit of 2 GHz) is used to record the pulse shapes whereas the Cx charge amplifier is used for charge measurements. A 2 GHz bandwidth limit defines the minimum rising time equal to  $t_r \simeq \frac{0.34}{BW} = \frac{0.34}{2 \times 10^9} = 170$  ps, therefore the system is capable of measuring pulses with a minimum FWHM  $\simeq 170$  ps. This already makes it impossible to measure the initial peak in the  $\alpha$  response due to the two opposite charge carriers travelling. If a charge carrier travelling through the bulk takes  $t_{t1} \sim 6$  ns to reach the electrode on the opposite side ( $d_1 \sim 500$   $\mu\text{m}$ ), the carrier with the opposite charge and a shorter path to the closer electrode – max.  $d_2 \sim 10$   $\mu\text{m}$  – only takes  $t_{t2} \sim \frac{d_2}{d_1} t_{t1} = 120$  ps. A drift time this short induces a current pulse that is too narrow for the C2 amplifier or the oscilloscope to be able to observe.

Figure 3.5 shows a set of pulses and an averaged pulse for  $\alpha$ ,  $\beta$  and  $\gamma$  radiation using an  $^{241}\text{Am}$ ,  $^{90}\text{Sr}$  and  $^{60}\text{Co}$  source, respectively. The particles are measured with the non-irradiated sCVD diamond S37.  $\alpha$  particles always produce the same signal pulse, but with a high noise RMS. The averaging suppresses the noise while retaining most the information. It does, however, smear the rising and falling edge, increasing the rising and falling time. The  $t_r$  is now of the order of 0.5 ns. Both  $\beta$  and  $\gamma$  pulses look similar - triangular and with a wide range of amplitudes. Here the pulse count is low, so the pulses with a high amplitude are not recorded. A trigger set very high would be needed to “catch” them with the oscilloscope.

### 3.2.1 Noise limitations

Noise is a major limiting factor in particle detection. It defines the minimum measurable particle energy and the minimum measurement resolution. It is hence important to minimise the electric noise in the detector signal. The major noise contribution

### 3.2. CHARGED PARTICLE PULSES AND SPECTRA

---

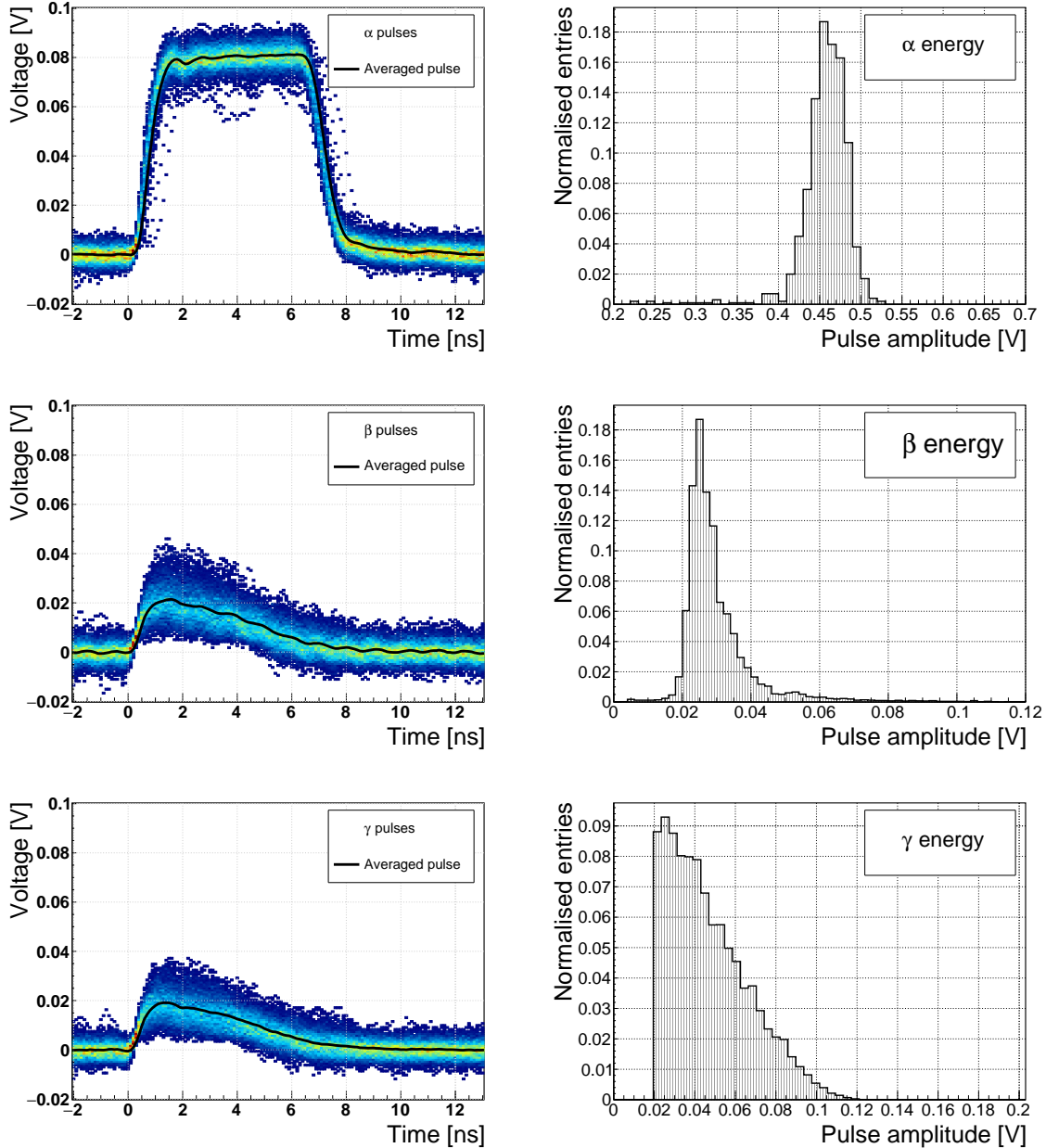


Figure 3.5: Superimposed and averaged pulses (left figures, current amplifier) and distributions of deposited energy (right figures, charge amplifier) for three types of radiation. Note the scale on the X axis of the distributions.

comes from poor shielding from external electromagnetic sources. These often cause ringing whereby the signal oscillates with a frequency defined by the external source. The ringing makes high-frequency measurements impossible. Another source of noise is the sensor itself. In the case of silicon, natural light increases the number of thermally excited free charge carriers, increasing the leakage current. This is not the case for diamond, which is with its high energy band gap insensitive to visible light.

1199 Nevertheless, any noise produced by the sensors is amplified by the signal amplifiers,  
1200 which add an additional noise of the analogue electrical circuit to the amplified  
1201 signal. Finally, the digitisers add the quantisation noise to the digitised signal. If  
1202 the measurement range is significantly higher than the actual measured signal, the  
1203 quantisation noise can be a significant contributor to the decrease of the overall mea-  
1204 surement resolution.

### 1205 3.3 Radiation limitations

1206 Exposure to ionising radiation degrades sensors. It deforms the lattice by displacing  
1207 the atoms. Various types of lattice defects can be created in diamond, similar to those  
1208 in silicon: vacancies, interstitials etc. [31] These deformations introduce new discrete  
1209 energy levels between the valence and conduction band. Charge carriers drifting in  
1210 their vicinity can get trapped, their energy falling to the energy level of the trap.  
1211 Their emission back to the conduction band depends on how deep the trap is (how  
1212 far away from the conduction band it is). The carriers caught in the shallow traps  
1213 of the order of 100 meV below the conduction band are excited back up already by  
1214 means of thermal excitation. This phenomenon has a short time constant, dependant  
1215 on the environmental temperature. Those stopped by deep traps near the middle  
1216 of the band gap need more energy and thus more time to be emitted to either the  
1217 conduction or valence band. Some charge carriers remain trapped for long periods.  
1218 If they build up in a certain region of the diamond, their charge starts affecting the  
1219 surrounding electric field – this is referred to as formation of space-charge. It can  
1220 either help or counteract the field, depending on the polarity of the trapped carriers.

1221 The energy band jumping goes the other way, too. The carriers in the valence band  
1222 may use the intermediate energy levels as “stepping stones” to jump to the conduction  
1223 band and start drifting in the externally applied electric field. This occurrence is  
1224 referred to as the leakage current.

1225 The electrons and holes stopped in these traps cause a decrease of the induced  
1226 current on the electrodes. This yields a lower integrated charge in an irradiated  
1227 sensor than that in a non-irradiated one. The charge collection efficiency is therefore  
1228 correlated with the level of irradiation.

1229 This section contains a study of the effects of pion ( $\pi_{300 \text{ MeV}}$ ) irradiation on the  
1230 charge collection efficiency of sCVD diamond detectors. To carry out this study,  
1231 two diamond samples have been irradiated to doses of  $1 \times 10^{14} \pi \text{ cm}^{-2}$  (S79) and to  
1232  $3.63 \times 10^{14} \pi \text{ cm}^{-2}$  (S52). A test beam campaign has to be carried out to observe  
1233 the charge collection efficiency at different bias voltage settings. The efficiency values  
1234 acquired are used to determine the effective drop in efficiency with as a function of re-  
1235 ceived radiation dose. This is to test if the collected charge  $Q$  is inversely proportional  
1236 to the received dose  $\Phi$ . A procedure defined by a collaboration researching diamond  
1237 behaviour RD42 has been applied to the measured values to extract the damage fac-  
1238 tor. The next subsection contains measurements and results of a long-term stability  
1239 study using  $\alpha$  and  $\beta$  particles. In particular, the charge collection efficiency as a

### 3.3. RADIATION LIMITATIONS

---

function of time is measured during the measurements with  $\beta$  and  $\alpha$  radiation. To investigate this effect on the scale of charge carriers, the change of TCT (transient current technique) pulses with time is observed. Finally, a procedure that improves the pulse shape and with it the charge collection is proposed.

#### 3.3.1 Quantifying radiation damage in diamonds

Radiation damage varies with the type of radiation and its energy. There are several models existing [27, 26] that try to explain the impact of irradiation and to provide *hardness factors* to compare the radiation damage between different particles. The standard way is to convert the damage into *neutron equivalent* [14]. Some models have been extensively verified with simulations and with experiments. In these experiments the charge collection in sensors is measured before and after irradiation. This procedure is repeated several times, with a measurement point taken after every irradiation. When a set of measurements of charge collection is plotted against the radiation dose received by a specific particle at a specific energy, a damage factor  $k_\lambda$  can be extracted. Damage factors have to be measured across a range of energies and types of radiation to properly quantify the damage in the sensors. They are then compared against the simulations to verify that the experimental observations are in line with the theory.

Diamond is an expensive material and the technology is relatively new as compared to silicon. Therefore not many institutes are carrying out diamond irradiation studies. To join the efforts, the RD42 collaboration [11] has been formed. It gathers the experimental data from diamond irradiation studies. Unlike with silicon, the experimental results so far show no significant correlation with the NIEL (non-ionising energy loss) model [27], which correlates detector efficiency with the number of lattice displacements. Therefore an alternative model was proposed [26], correlating the diamond efficiency with the number of displacements per atom (DPA) in the bulk. The idea is that if the recoil energy of an incident particle is higher than the lattice binding energy (42 eV for diamond), the atom is displaced from its original position. The newly formed vacancy acts as a trap for drifting charge carriers. The more displacements that form in the bulk, the higher is the probability that a drifting carrier gets trapped. However, different types of particles interact differently with the bulk. In addition the mechanisms of interaction at low energies are different to those at high energies. To assess the damage for individual particles at a range of energies, simulations need to be run first. The simulation shown in [26] shows the DPA model for a range of energies of proton, pion and neutron irradiation in diamond. Figure 3.6 contains the simulation results as well as the superimposed empirical results of several irradiation studies. According to the figure, a 300 MeV pion beam damages the diamond bulk twice as much as a 24 GeV proton beam. The data points obtained by RD42 are also added to the figure. They have been normalised to damage by 24 GeV protons. Finally, the data point measured in the scope of this thesis has been added for comparison. The derivation is done below.

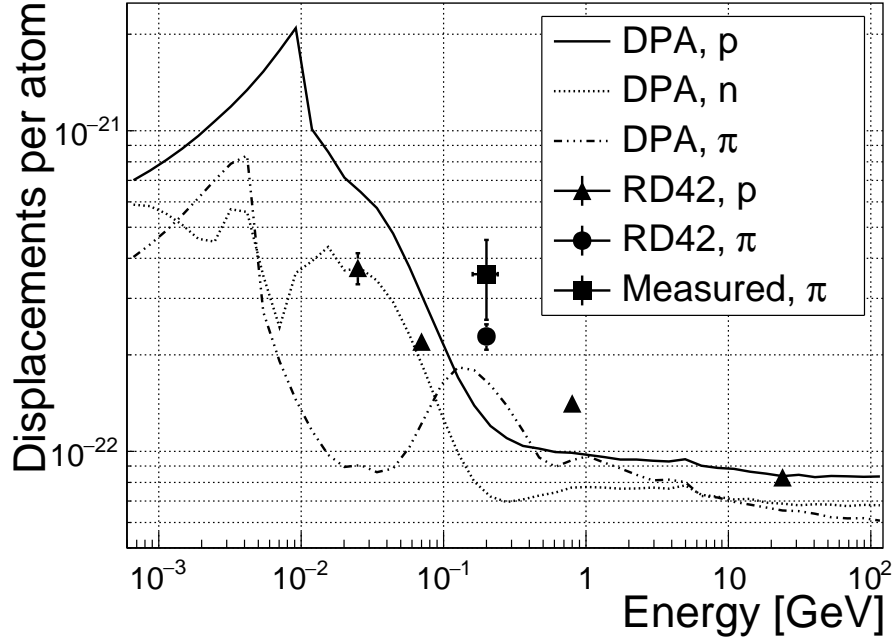


Figure 3.6: Diamond radiation damage - a model based on displacements per atom [26]. Added are data points for protons and pions by RD42 [35] and one data point for pions measured in the scope of this study.

1281 **3.3.1.1 Irradiation with a  $\pi_{300 \text{ MeV}}$  beam**

1282 The samples were irradiated at the Paul Scherrer Institute (PSI) [10] by means of a  
 1283 beam of pions with an energy of 300 MeV (kinetic energy 191.31 MeV) and with a  
 1284 flux of up to  $1.5 \times 10^{14} \pi \text{ cm}^{-2}$  per day. The system has a 10 % uncertainty on the  
 1285 beam energy. In addition, their quoted uncertainty on the measurement has an error  
 1286 of  $\pm 20 \%$ . Looking at the pion damage curve in figure 3.6,  $\pi_{300 \text{ MeV}}$  point sits on a  
 1287 steep section of the DPA curve. This means that a deviation in beam energy can  
 1288 have a significant effect on the damage.

1289 Two diamond samples, S52 and S79, were put in the  $\pi_{300 \text{ MeV}}$  beam in the 2014  
 1290 PSI irradiation campaign; S52 to  $(1 \pm 0.21) \times 10^{14} \pi \text{ cm}^{-2}$  and S79 to  $(3.63 \pm 0.77) \times$   
 1291  $10^{14} \pi \text{ cm}^{-2}$ . During the process, the golden electrodes got slightly activated, but the  
 1292 activation decayed in two weeks.

1293 **3.3.1.2 Charge collection efficiency and charge collection distance**

1294 Three diamonds – non-irradiated S37 and irradiated S52 and S79 – were tested in a  
 1295  $\pi_{120 \text{ GeV}}$  test beam in the SPS North Experimental Area at CERN [18] before and  
 1296 after irradiation. The goal was to estimate the charge collection efficiency (CCE) and  
 1297 charge collection distance (CCD) as a function of irradiation dose. The samples were  
 1298 primed (pumped) prior to data taking using a  ${}^{90}\text{Sr}$  radioactive source. The data were  
 1299 then taken at a range of bias voltages ranging from 30 V to 900 V, yielding between

### 3.3. RADIATION LIMITATIONS

---

1300 0.06 V/ $\mu\text{m}$  and 1.8 V/ $\mu\text{m}$  electrical field in the bulk. Every data point contained  
 1301 approximately  $5 \times 10^4$  measured particles. The charge deposited by the particles  
 1302 was measured using a CIVIDEC Cx charge preamplifier. As expected, the integrated  
 1303 amplitude spectrum followed a landau distribution. Its most probable value (MPV)  
 1304 is used to calculate the most probable collected charge  $Q_i$ :

$$Q_i [e^-] = \frac{Q_i [fC]}{1.6 \times 10^{-4}} = \frac{MPV [mV]}{A [mV/fC]} \cdot 6.241 \times 10^4 \quad (3.2)$$

1305 where  $A = 9.3 \text{ mV/fC}$  is the preamplifier gain factor. The CCD can then be calculated  
 1306 using the average number of electron-hole pairs produced per micrometer in diamond  
 1307  $\delta_d = 36 \text{ e-h } \mu\text{m}^{-1}$  (from table 5.2):

$$CCD = \frac{Q_i}{\delta_d}. \quad (3.3)$$

1308 The resulting CCD for the three measured samples at bias voltages ranging from  
 1309 0.2–1.6 V  $\mu\text{m}^{-1}$  is shown in figure 3.7a. S37 exhibits a full collection distance already  
 1310 at 0.4 V  $\mu\text{m}^{-1}$  whereas the irradiated samples have a more gentle increase of CCD  
 1311 with increasing bias voltage. It is evident that at 1 V  $\mu\text{m}^{-1}$  the maximum CCD has  
 1312 not been reached in the case of S79 and S52. Nevertheless, to compare the measured  
 1313 data point with those provided by RD42, the CCD at 1  $\mu\text{m}$  has to be taken.

#### 1314 3.3.1.3 Irradiation damage factor

1315 The irradiation damage factor  $k_\lambda$  is a way to quantify irradiation damage of a specific  
 1316 particle at a specific energy. Via this factor different types of irradiation can be  
 1317 compared. It is obtained experimentally by measuring the CCD of a number of  
 1318 samples at various irradiation steps and fitting the equation 3.5 to the data.  $\lambda$  is the  
 1319 measured CCD,  $\lambda_0$  is the CCD of a non-irradiated sample and  $\Phi$  the radiation dose.  
 1320 As a reference, the damage factor for 24 GeV protons is set to  $1 \times 10^{-18} \mu\text{m}^{-1} \text{ cm}^{-2}$ .

$$\frac{1}{\lambda} = \frac{1}{\lambda_0} + k_\lambda \cdot \Phi \quad (3.4)$$

$$\lambda = \frac{\lambda_0}{k_\lambda \lambda_0 \Phi + 1} \quad (3.5)$$

1321 The data points with the maximum CCD obtained in the test beam measurements  
 1322 are plotted against radiation dose received in figure 3.7b. Equation 3.5 is fitted to  
 1323 the data points and a damage factor  $k_\lambda = (4.4 \pm 1.2) \times 10^{-18} \mu\text{m}^{-1} \text{ cm}^{-2}$  can be  
 1324 obtained. The value is for a factor of two higher than the damage factor obtained by  
 1325 RD42. This could be due to an insufficient priming time ahead of the measurement.  
 1326 In addition, the diamond samples have not been polished and re-metallised after  
 1327 irradiation, as is the case for the RD42. Also, with only two samples measured, the  
 1328 statistical uncertainty is high. Nevertheless, it can be concluded that the 300 MeV  
 1329 pions damage the diamond bulk significantly more than the 24 GeV protons.

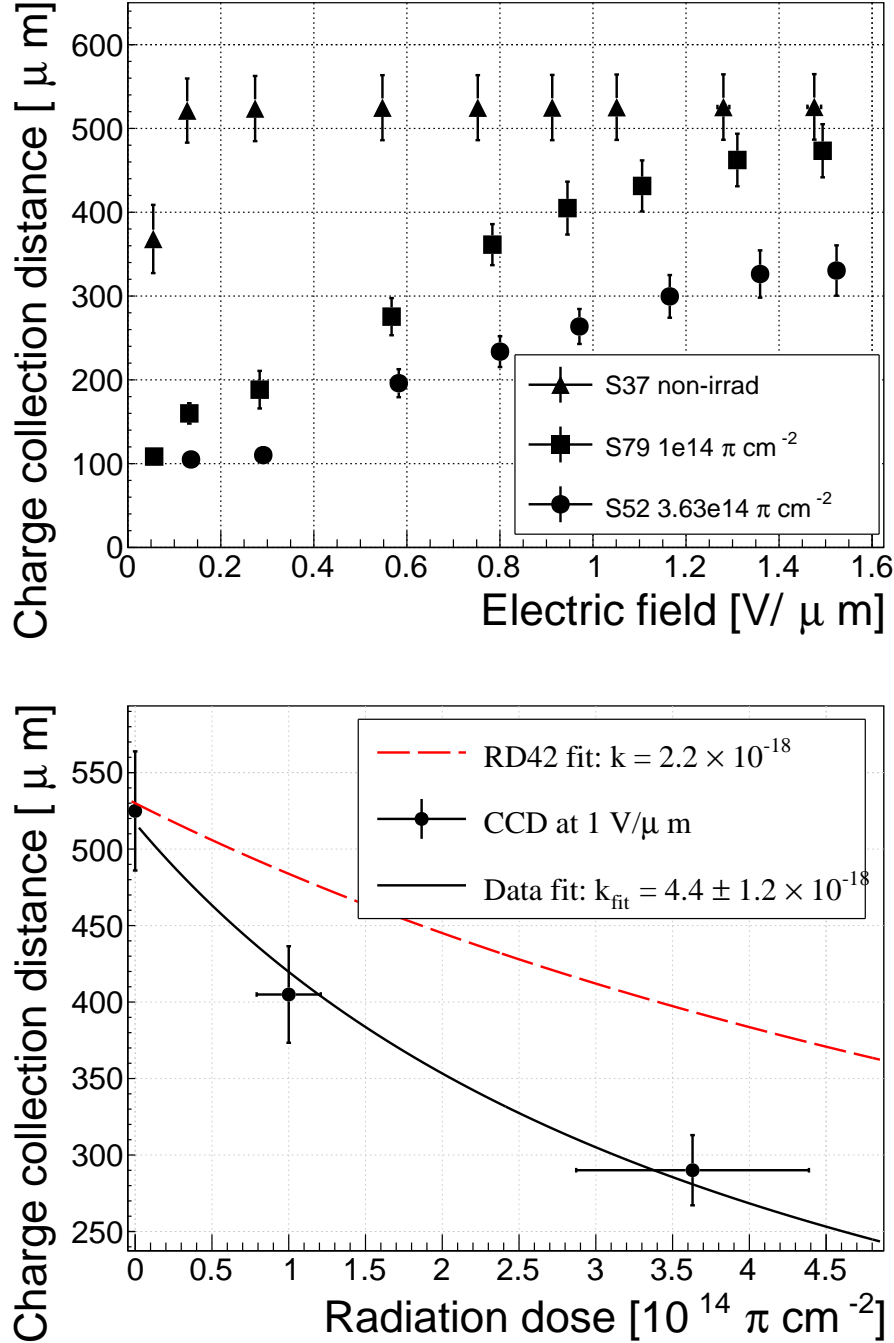


Figure 3.7: First figure shows the CCD for S37, S79 and S52 at a range of bias voltage settings. The charge collection distance at  $1 \text{ V}/\mu\text{m}$  bias voltage for the three diamond samples is then compared to the RD42 data for pion irradiation in the second figure. The data points are about 15–25 % lower than expected from the RD42 data [35].

### <sup>1331</sup> 3.3.2 Long-term measurement stability

<sup>1332</sup> An important requirement for particle detectors is a stable performance over long  
<sup>1333</sup> periods of time. For instance, the charge collection for a defined radiation type and

### **3.3. RADIATION LIMITATIONS**

---

1334 quantity must not change over time or has to change in a predicted way. Diamonds  
1335 are stable as long as their environment and their operating point does not change  
1336 significantly. The stability of diamond detectors depends on many factors: material  
1337 purity, polishing process, electrode material, irradiation damage etc. The aim is  
1338 to study the behaviour of diamond under controlled conditions, with the goal to  
1339 understand its limitations. One of these limitations is the received radiation dose as  
1340 it can affect the long-term stability of the sensor during operation.

1341 The three diamond samples (S37, S79 and S52) have been exposed to two different  
1342 types of ionising radiation for a longer period to see if their behaviour changes over  
1343 time. Two parameters have been observed in particular:

- 1344     1. Charge collection of  $\beta$  particles and
- 1345     2. Charge collection and ionisation profile of  $\alpha$  particles.

1346 The results in this and in the following section show that priming plays an important  
1347 role in improving the diamond measurement stability in both cases.

#### **1348     3.3.2.1 $\beta$ long-term stability**

1349 The diamond samples have undergone a long-term stability test using  $\beta$  radiation.  
1350 This has been done using a  $^{90}\text{Sr}$  source emitting  $\sim 2$  MeV electrons at a rate of  
1351 approximately  $10^4 \text{ e}^- \text{ cm}^{-2}$ . To simulate the initial conditions in HEP experiments,  
1352 the sensors must not be primed before starting the measurements. The measurement  
1353 setup consists of a diamond sample (S37, S52 or S79) with the Cx spectroscopic  
1354 amplifier, a silicon diode with a C6 amplifier for a trigger and a  $^{90}\text{Sr}$  source on top.  
1355 A particle emitted by the source traverses the sensor bulk and hits the silicon diode,  
1356 triggering the analogue signal readout. The source is left on the top for the course  
1357 of the experiment. The measurements, however, are taken at discrete times. For  
1358 every data point, approximately  $10^4$  triggers have to be recorded. The offline analysis  
1359 of the recorded signal pulse amplitudes yields a landau distribution for every data  
1360 point. The most probable value (MPV) of the distribution is proportional to the  
1361 collected charge by the diamond sensor. The resulting graph of charge collection  
1362 over time in figure 3.8 shows that the charge collection efficiency improves when the  
1363 diamond sensor is primed with a  $\beta$  source. This is especially evident in the case of  
1364 the two irradiated samples. S79 achieves close to a full efficiency whereas S52 reaches  
1365 about 50 %. Both increases are significant. At a received dose of approximately  
1366  $4 \times 10^6$  particles the signal stabilises. As expected, the signal of the non-irradiated S37  
1367 does not change with priming – this pure sCVD diamond sample has the maximum  
1368 collection distance from the start of the measurement.

1369 The  $\sim 2.28$  MeV electrons emitted by this source are not MIPs; their charge depo-  
1370 sition is higher than that of an electron MIP, according to the Bethe-Bloch distribu-  
1371 tion [16]. Nevertheless, for the purpose of these measurements this energy is adequate  
1372 since only the relative change in charge collection is of interest.

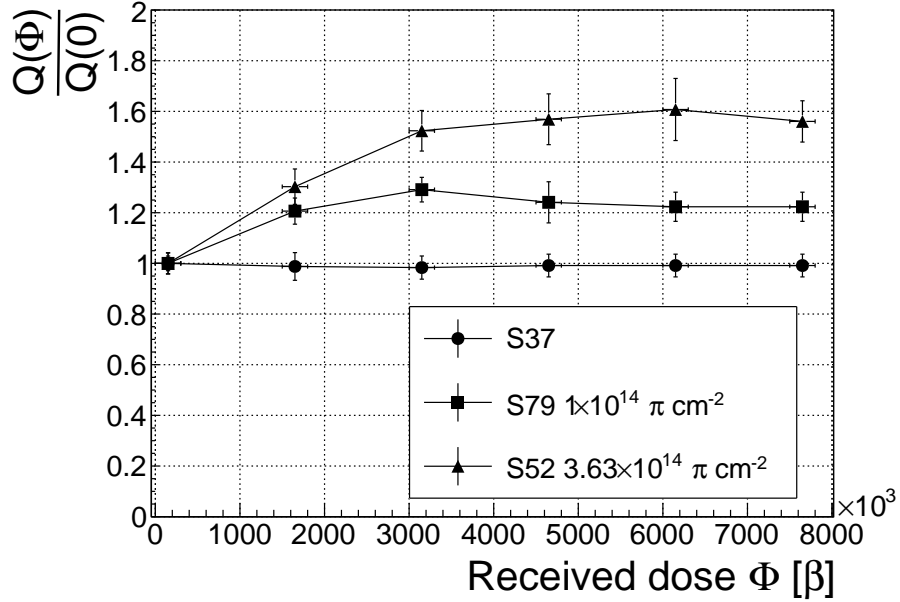


Figure 3.8: Relative increase of charge collection over time due to priming with the  $^{90}\text{Sr}$  radioactive source. The charge collection for the non-irradiated S37 stays constant. The bias voltage for this measurement is 1 V/ $\mu\text{m}$ .

To sum up, diamond is a good choice for  $\beta$  radiation detection. Even if damaged by radiation, it reaches a stable charge collection at a received dose of  $\sim 4 \times 10^6$  MIP particles. The efficiency decreases with a high irradiation dose (effects visible above  $10^{12}$  MIP  $\text{cm}^{-2}$ ). However, the decrease can be accounted for if the damage factor and the rate and energy of the particles are known.  $\gamma$  radiation has a similar impact on the diamond as the  $\beta$ . The incident photons, if they interact with the diamond, prime the bulk, increasing the charge collection efficiency. The difference, however, is that the interaction probability (cross-section) is lower for gammas [41, 25].

### 3.3.2.2 $\alpha$ long-term stability

This part discusses the stability of irradiated diamond sensors during  $\alpha$  measurements. An  $^{241}\text{Am}$  source is used, emitting  $\alpha$  particles with a mean energy of 5.5 MeV. It is safe to assume that they affect the diamond differently than when subject to  $\beta$  radiation. This is due to the point-like charge carrier creation; an  $\alpha$  particle penetrates the bulk and stops at a depth of  $\sim 14$   $\mu\text{m}$  (for a 5.5 MeV particle). The deposited energy produces  $\frac{5.5 \text{ MeV}}{13.6 \text{ eV}} = 4 \times 10^5$  e-h pairs. Compared to a MIP, which produces an MPV of  $500 \mu\text{m} \times 36 \text{ e-h } \mu\text{m}^{-1} = 18 \times 10^3$  e-h pairs in a 500  $\mu\text{m}$ , the collected charge is for a factor of 22 higher. In addition, the energy is deposited in a small volume – 14  $\mu\text{m}$  in depth and  $\sim 20$  nm radially [28]. This dense distribution of charge carriers affects their behaviour at the start of the drift. Furthermore, carriers of only one polarity drift through the sensor while those of the opposite polarity almost instantly

### 3.3. RADIATION LIMITATIONS

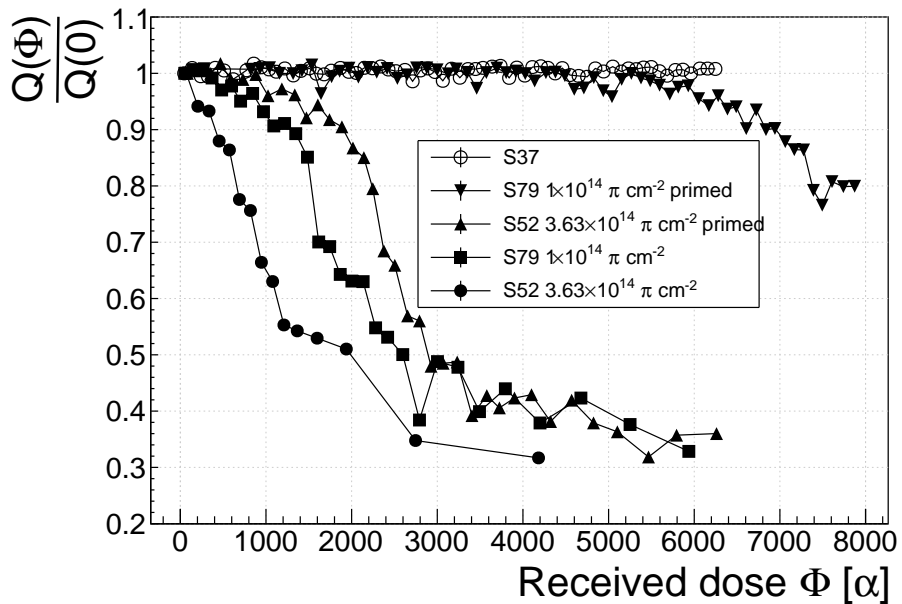


Figure 3.9: Relative decrease of collected charge with time for non-irradiated and irradiated diamond samples.

recombine with the adjacent electrode. Taking into account that the diamond bulk has been damaged by irradiation, these two phenomena might have an effect on the operation of the detector.

The first test has been carried out using the Cx spectroscopic amplifier, with the bias voltage of the samples set to +500 V. Figure 3.9 shows the results of 6500 recorded hits at a rate of  $\sim 7$  particles per second. The collected charge  $Q(\Phi)$  for the non-irradiated sample is stable as compared to the initial collected charge  $Q(0)$  (plotted as a relative value  $\frac{Q(\Phi)}{Q(0)}$ ). It is expected that the irradiated samples have a lower charge collection efficiency than the non-irradiated sample. However, their initial efficiency suddenly drops after a certain period of time. The initial efficiency after priming with  $\beta$  particles is higher than that without priming, but eventually it also deteriorates. In addition, the spread of measured energies increases significantly. Finally, the particle counting rate decreases with a decreased efficiency.

To investigate this sudden drop in efficiency, the current pulse shapes using a C2 current amplifier have to be observed, as shown in figure 3.10. The shape of the pulse holds more information about the charge carrier properties in the sensor than solely the value of the integrated charge. This time only the primed S79 sample has been tested. Both the hole and the electron collection are observed to determine whether they behave differently or not. The sample has been measured long enough for the pulse shapes to start changing. The data in figures 3.10 show that the initially stable pulses start deteriorating – suddenly several different shapes start appearing, some still very similar to those from the beginning while the others with almost zero amplitude.

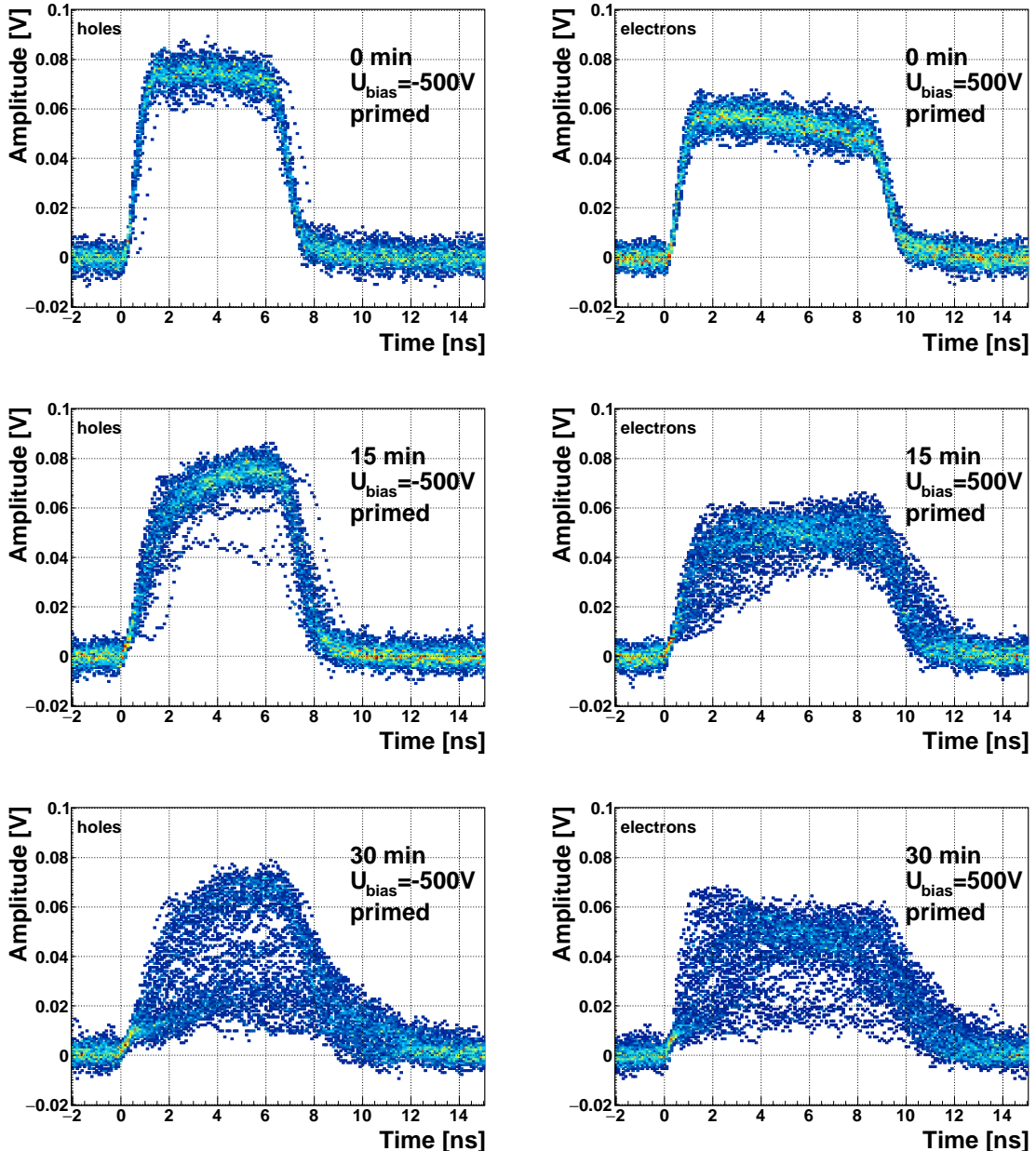


Figure 3.10: The signal of the irradiated and primed S79 deteriorates with time for both polarities. Every plot contains 60 superimposed pulses.

1416 Some charges get stopped in the charge traps in the bulk for a long time, building  
 1417 up regions of space charge. The built up space charge affects the electric field, making  
 1418 it non-uniform. The non-uniform field in turn affects the drifting carriers, slowing  
 1419 them down or speeding them up, depending on the field gradient. Since the movement  
 1420 of the carriers is inducing the electric current, the field gradient can be observed in  
 1421 the signal.

1422 The second test with the C2 current amplifier has been carried out as follows: at

### 3.3. RADIATION LIMITATIONS

---

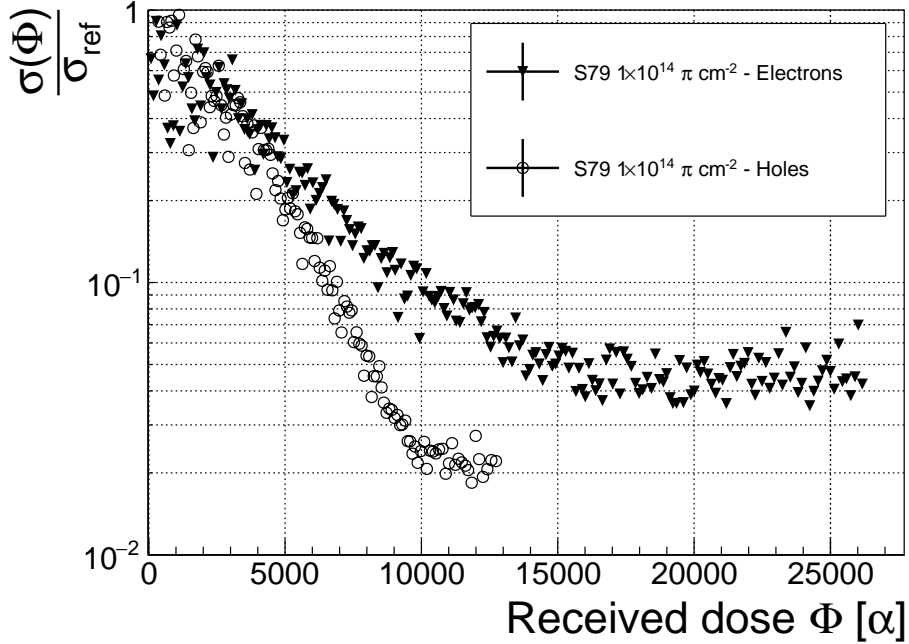


Figure 3.11: Deterioration of the pulse shapes with time.

the beginning of the test when the diamond is still operating stably, 60 pulses are recorded. An average pulse is calculated. This is a reference pulse for the subsequent measurement points. Then an RMS of the single pulses with respect to the reference pulse is calculated and the resulting RMS values are summed together ( $\sigma_{\text{ref}}$ ).

All the subsequent data points also consist of a set of 60 pulses. At every data point the summation of the RMS values of the individual pulses with respect to the initial averaged pulse is calculated ( $\sigma$ ). The ratio between the initial  $\sigma_{\text{ref}}$  and discrete values  $\sigma$  gives a measure of change of the pulse shape with respect to the reference pulse at the start of the measurement. Figure 3.11 shows the ratio  $\frac{\sigma_{\text{ref}}}{\sigma(\alpha \text{ dose})}$ . From the data obtained it can be concluded that the initial pulse shape quickly starts deteriorating. In fact, the deterioration of the shape follows an approximate exponential decay function, which can be fitted to the data. The resulting decay constants for electrons and holes are  $\tau_e = (4400 \pm 150) \alpha^{-1}$  and  $\tau_h = (3300 \pm 140) \alpha^{-1}$ . The electrons retain the initial shape for longer. The deteriorated shapes also seem to be for a factor of 2 better than those of the holes.

**Restoring the pulse shapes** Finally, an effort has been made to find a way for the pulse shapes to return to their initial state. Five methods are listed:

1. Removing the source and leaving the bias voltage switched on,
2. Removing the source and switching the bias voltage off,
3. Priming with  $\gamma$  at a rate of  $400 \text{ s}^{-1} \text{cm}^{-1}$  without applied bias voltage,
4. Priming with  $\beta$  at a rate of  $1000 \text{ s}^{-1} \text{cm}^{-1}$  with applied bias voltage and

<sup>1444</sup> 5. Priming with  $\beta$  at a rate of  $1000 \text{ s}^{-1}\text{cm}^{-1}$  without applied bias voltage.

<sup>1445</sup> The diamond sample S79 is first primed using a  $^{90}\text{Sr}$  source for approximately one  
<sup>1446</sup> hour. Then the bias voltage is switched on and an  $^{241}\text{Am}$  source is put on top. The  
<sup>1447</sup> pulses produced by the incident  $\alpha$  particles have a proper rectangular pulse at the  
<sup>1448</sup> beginning, but then start changing – first gradually and later increasingly more in  
<sup>1449</sup> an erratic way, as described in the text above. After approximately 30 minutes, one  
<sup>1450</sup> of the methods is tested. When a “healing” procedure is started, a set of 60 pulses  
<sup>1451</sup> is taken at irregular points of time to observe the change in the pulse shape and to  
<sup>1452</sup> assess the quality of the “healing” procedure. Then the bias voltage is switched off  
<sup>1453</sup> and the sample is primed again to reset its state before starting with the next run.

<sup>1454</sup> The results depicted in figure 3.12 show that the methods (3) and (5) improve the  
<sup>1455</sup> shape, method (2) helps slowly, (1) does not show any change with time and (4) at first  
<sup>1456</sup> improves, but then significantly degrades the shape. The effect observed in method  
<sup>1457</sup> (4) has already been described in [32]. The “healing” process therefore depends on  
<sup>1458</sup> the rate of radiation, the bias voltage and the time of exposure. The ionising radiation  
<sup>1459</sup> creates free charges, which quickly recombine close to the place of generation. It is  
<sup>1460</sup> likely that they also release the charges trapped during the measurement, reducing the  
<sup>1461</sup> overall effect of the space charge. The traps get filled with both flavours of carriers,  
<sup>1462</sup> thus they are neutralised. The pulse shape gradually returns to its initial state.

	Procedure	Source	Bias voltage	Effectiveness
<sup>1463</sup>	1	/	ON	no
	2	/	/	slow
	3	$^{60}\text{Co}$	/	YES
	4	$^{90}\text{Sr}$	ON	no
	5	$^{90}\text{Sr}$	/	YES

<sup>1464</sup> Table 3.2: Effectiveness of healing procedures.

<sup>1465</sup> In summary, the shape of the pulses caused by  $\alpha$  radiation changes with time  
<sup>1466</sup> for irradiated samples. The shape of the pulses gets distorted and becomes erratic.  
<sup>1467</sup> Charge collection decreases and its spread increases. This happens even faster for  
<sup>1468</sup> non-primed diamonds. To “heal” the diamond – to bring the pulse shapes back to  
<sup>1469</sup> their initial shape – the sample must be primed using a  $\beta$  or a  $\gamma$  source for several  
<sup>1470</sup> minutes at a bias voltage of 0 V. Switching to the inverse polarity for a few seconds  
<sup>1471</sup> helps a bit, but in a long run distorts the signal, which cannot return to its initial  
<sup>1472</sup> shape.

### <sup>1473</sup> 3.4 Temperature limitations

<sup>1474</sup> A test has been carried out to evaluate the effect of temperature changes on the  
<sup>1475</sup> output signal of the diamond sensors. A cryostat filled with liquid helium is used to  
<sup>1476</sup> cool down the sensor during the measurement process. The current signal response

### 3.4. TEMPERATURE LIMITATIONS

---

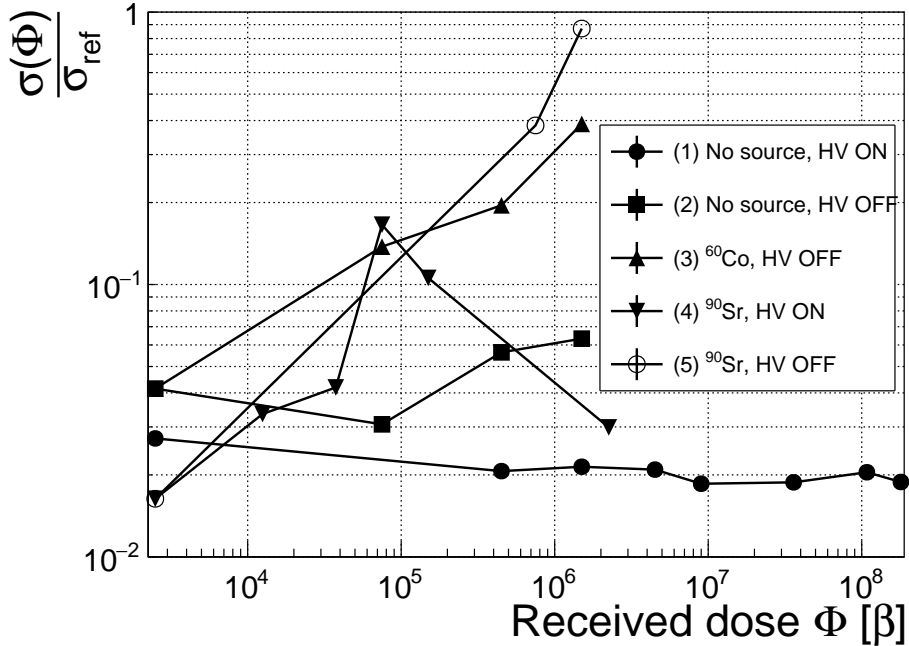


Figure 3.12: Comparison of the five procedures for the “healing” process for an irradiated diamond that had been exposed to  $\alpha$  radiation with a rate of  $10^1 \text{ s}^{-1}$ , with the bias voltage switched on, for at least 30 minutes.

to  $\alpha$ -particles is measured at 18 temperature points between 4 K and 295 K. At every temperature point a set of 300 pulses is read out at various bias voltages. Resulting data show that the charge collection is stable from RT down to 150 K where it starts decreasing. It stabilises again at about one third of the initial value at 75 K. This behaviour was first measured and discussed by H. Jansen [28].

The band gap energy in diamond is equal to  $E_g = 5.5 \text{ eV}$  while the average energy to produce an electron-hole pair is  $E_{e-h} = 13.25 \text{ eV}$ . This means there is excessive energy deposited in the diamond bulk. The incident  $\alpha$ -particle stops within  $\sim 10\text{--}15 \mu\text{m}$  of the bulk, transferring all its energy to the lattice during deceleration. A part of this energy directly ionises the carbon atoms, creating free electron-hole pairs. The positively charged hole and the negatively charged electron in the hole attract each other via the Coulomb force and may undergo a bonding process during which an exciton is emitted.

The remaining energy, however, is converted into lattice vibrations (phonons [45, 28]). This means that the lattice within the ionisation volume (approximately  $\sim 15 \mu\text{m} \times \sim 2 \text{ nm}$  in size) is briefly heated up. The hot plasma then cools down to the temperature of the surrounding material by heat dissipation, (i.e. phonon transport).

The free electron binds with the free hole into a bound state (not recombination) – the exciton [33]. The exciton binding energy is 80 meV. At higher temperatures the lattice provides enough energy to thermally excite the electron from the exciton state back to the conduction band. At lower temperatures, however, the exciton lifetime

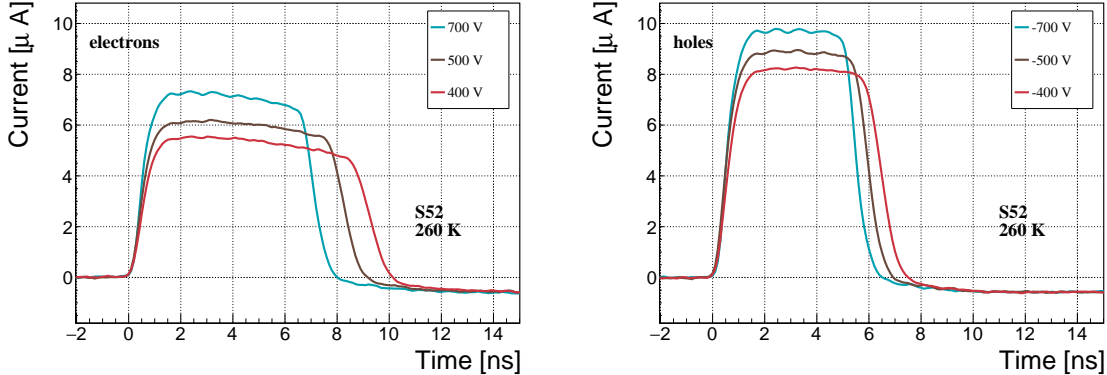


Figure 3.13: Varied bias voltage at a fixed temperature.

increases, which means that it takes a longer time for the electrons to get re-excited to the conduction band. The re-excitation lifetime at room temperature is  $\sim 30$  ps, increasing to  $\sim 150$   $\mu$ s at 50 K [28]. This means that some of the bound electrons do not even start drifting within the period of  $\sim 10$  ns, which is the expected carrier drift time. When they are finally freed, the current they induce is already hidden in the electronics noise. The effective area of the observed current pulse is therefore smaller than that of a pulse induced by all the carriers drifting at the same time. This in effect reduces the measured collected charge. The longer the time constant, the lower the measured collected charge, as shown in figure 3.17.

### 3.4.1 Temperature-variant $\alpha$ -TCT before irradiation

Three sCVD diamond samples have been tested at a range of temperatures using the  $\alpha$ -TCT technique. At each temperature point, the bias voltage is set to several positive and negative values. A set of 300 pulses is recorded at every data point and averaged offline. The resulting averaged pulses of sample S37 at the 260 K temperature point and a bias voltage of  $\pm 400$  V,  $\pm 500$  V and  $\pm 700$  V are shown in figure 3.13. The pulses induced by holes as charge carriers are shorter than those induced by electrons, which means that holes travel faster in diamond. The area of the pulse, however, is the same for both polarities, which corresponds to the fact that the same amount of charges is drifting in both cases.

Figure 3.14 shows pulses at a bias voltage set to  $\pm 500$  V across the range of temperatures between 4 K and 295 K. Several conclusions can be drawn by observing their shape. First, the pulse shapes change with decreasing temperature. The pulse time gets shorter, hinting at the faster carrier drift velocity  $v_{\text{drift}}$ . Second, between 150 K and 75 K there is a significant change in shape - the time constant of the rising edge increases significantly and the pulse area decreases. From 75 K down to 4 K there is no significant change. Last, the top of the pulse at the S52 is not flat, which means that a portion of the drifting charge is lost along the way. This is due to charge trapping, likely by means of crystal defects or impurities.

### 3.4. TEMPERATURE LIMITATIONS

---

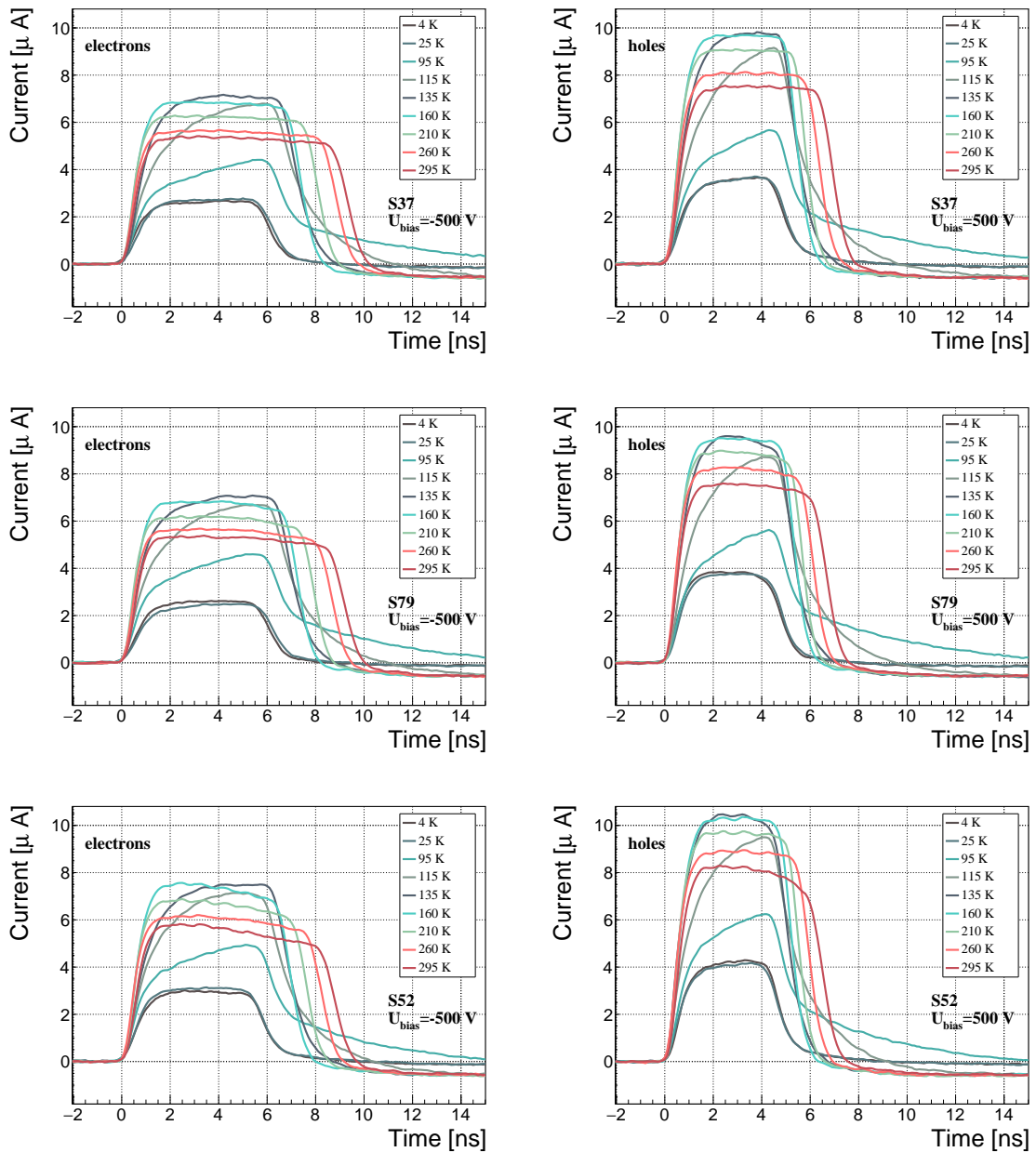


Figure 3.14: Several data points between 4 K and 295 K at a bias voltage of  $\pm 500$  V.

1526 **3.4.2 Temperature-variant  $\alpha$ -TCT after irradiation**

1527 The irradiated S79 and S52 have been re-tested in the cryostat after irradiation. The  
1528 aim is to observe how their pulse shapes change with decreasing temperature, in  
1529 particular the decaying top of the pulses, as shown in figure 3.15. The decay time  
1530 gives information on trapping of charge carriers while travelling through the diamond  
1531 bulk. A variation of the decay time constant as a function of temperature might  
1532 help to reveal the type and depth of the charge traps. To observe these effects or  
1533 lack thereof, a number of requirements have to be met. First, the diamond samples  
1534 are intentionally not primed prior to the experiment because priming would improve  
1535 the pulse shapes and possibly change the decay time constant of the signal. Second,  
1536 keeping in mind that the pulse shape of irradiated diamonds changes with time, the  
1537 duration of the measurement of an individual data point has to be short – of the  
1538 order of 30 seconds. Last, the sequence of the bias voltage settings is important, the  
1539 reason for which is explained below.

1540 Unfortunately it is not possible to avoid temporal pulse changes. For instance,  
1541 one measurement point takes approximately one minute. After the measurement, the  
1542 bias voltage polarity is swapped for a few seconds to bring the diamond back into its  
1543 initial state. But a few seconds with respect to a minute are not enough. Therefore  
1544 when the bias voltage is set to the next value, there is still some residual effect of  
1545 the previous measurement. Similar to the effects of polarisation, this effect is also  
1546 decreasing the pulse height. This can be observed in figure 3.15, which shows the  
1547 resulting pulses of S52 for bias voltages of  $\pm 200$  V,  $\pm 300$  V,  $\pm 400$  V and  $\pm 500$  V at  
1548 230 K and 260 K. In this case the measurement sequence is: 230K (200 V, 300 V,  
1549 400 V, 500 V, -500 V, -400 V, -300 V), 260 K (-200 V, -300 V, -400 V, -500 V,  
1550 500 V, 400 V, 300 V). The changes in pulse shapes for holes at 230 K and 260 K  
1551 cannot be attributed to the temperature change. Instead, the explanation could lie  
1552 in diamond “polarisation”. This means that, when exposed to an electric field with  
1553  $\alpha$  measurements ongoing, an internal electric field of inverse polarity builds up in the  
1554 diamond, which effectively reduces the overall electric field. This internal field does  
1555 not dissipate when the external bias voltage is switched off. The diamond becomes  
1556 “polarised”. When switching the polarity of the external bias voltage, the internal  
1557 and external electric field point in the same direction at the beginning, increasing the  
1558 overall electric field and with it the pulse height. In figure 3.15 this happens when  
1559 switching from 500 V (figure 3.15a) to -500 V (figure ??) at 230 K. The built up  
1560 polarisation contributes to the pulse having a sharp rising edge and a high amplitude.  
1561 This effect decays during the next two voltage points. There would be a handful of  
1562 ways to avoid this polarisation effect in the data:

- 1563 1. After every data point invert the bias voltage and leave it to return to a neutral  
1564 state for the same amount of time,
- 1565 2. Make a hysteresis of data points, going from minimum negative to maximum  
1566 positive bias several times,

### 3.4. TEMPERATURE LIMITATIONS

---

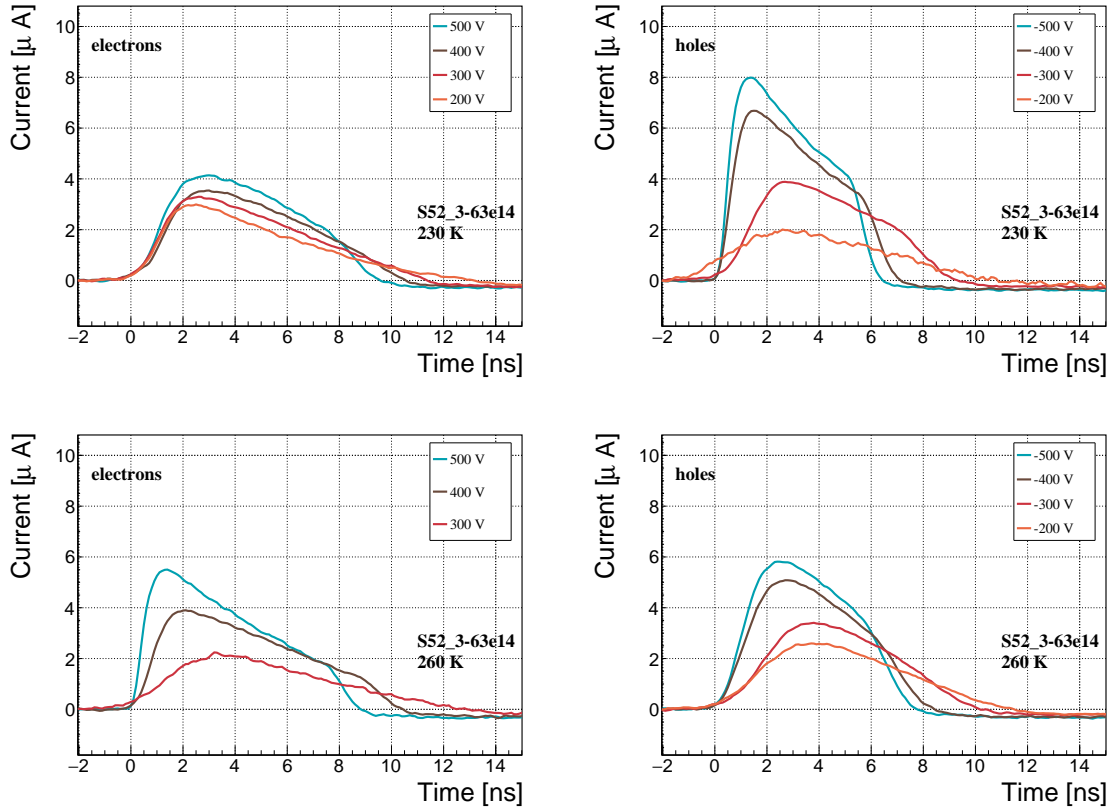


Figure 3.15: Varied bias voltage at a fixed temperature for an irradiated sample.

1567 3. Reduce the measurement time at every bias voltage setting.

1568 Unfortunately, options (1) and (2) are very time consuming and would increase the  
 1569 overall experiment time to over one day. The third option would worsen the resulting  
 1570 averaged pulses. In the end an alternative option has been chosen: alternating the  
 1571 starting bias voltage and the sequence at every temperature point. With this option,  
 1572 a meaningful systematic error in analysing the pulse shapes can be attained.

1573 Figure 3.16 shows the irradiated S52 and S79 as well as the non-irradiated S37  
 1574 for comparison, all at a bias voltage of  $\pm 500$  V and at several temperature points  
 1575 between 4 K and RT. It is evident that the radiation damage affects the shape of the  
 1576 pulses across all temperatures.

#### 1577 3.4.2.1 Collected charge as a function of temperature

1578 The area below the current pulse is proportional to the charge collected by the dia-  
 1579 mond detector. The collected charge is observed as a function of temperature. First,  
 1580 the amplitude values of the averaged pulses at a bias voltage of  $\pm 500$  V and across the  
 1581 temperature range between 4 K and 295 K have to be integrated. Then a calibration  
 1582 factor is used to derive the charge for all data points. This factor is obtained using a

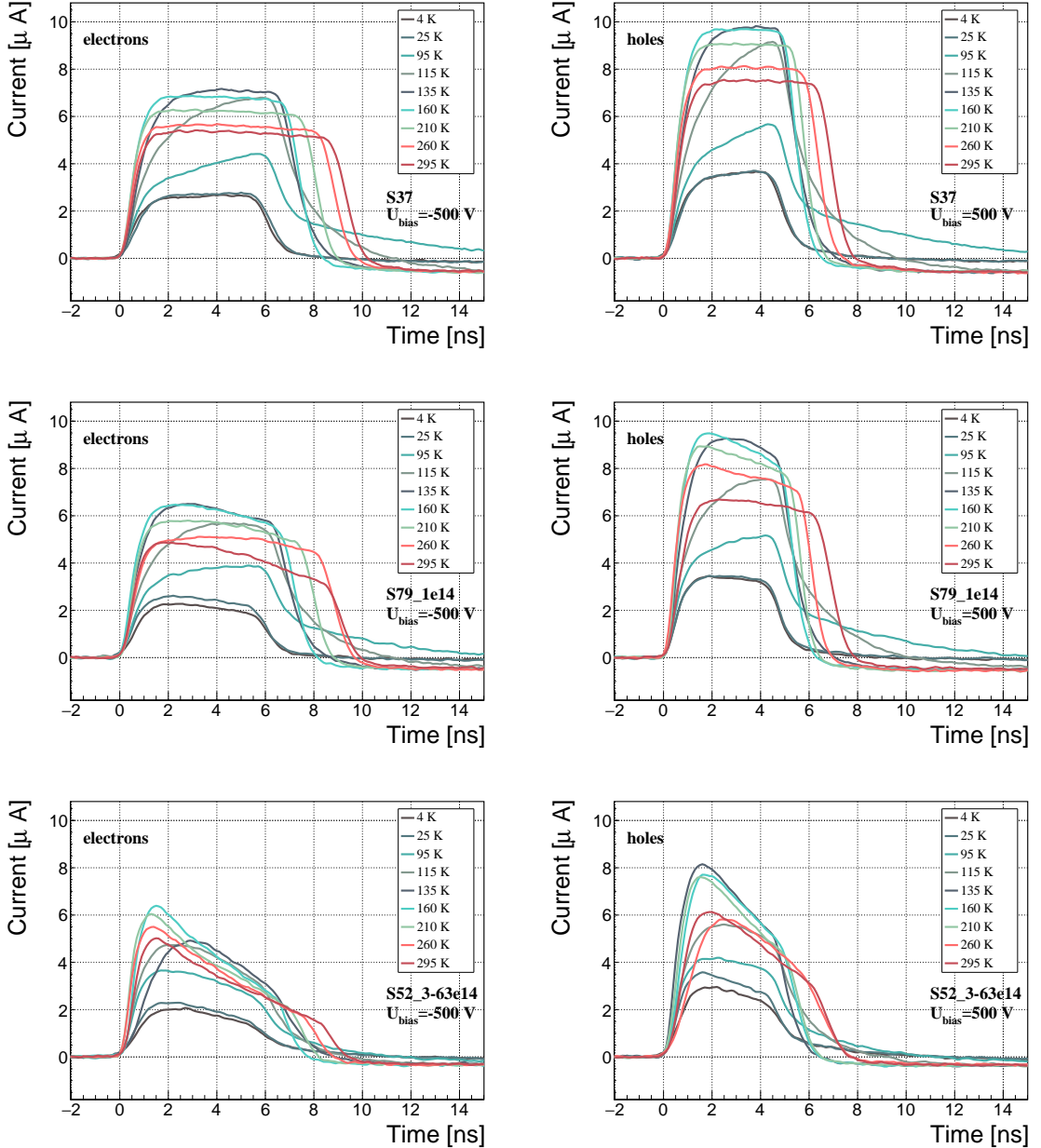


Figure 3.16: After irradiation: several data points between 4 K and 295 K at a bias voltage of  $\pm 500$  V.

Cx charge-sensitive amplifier. The resulting values for electrons and holes are plotted in figures 3.17a and 3.17b, respectively. Thesis [28] proposes a model that explains the drop in charge below 150 K. The new contribution are the data points for the irradiated samples. The values for them are lower than the those of non-irradiated samples, which is expected.

The values for all samples are fairly stable in the range between 4 K and 75 K and between 150 K and 295 K. However, in the values for the irradiated S52 some

### 3.4. TEMPERATURE LIMITATIONS

---

1590 excursions can be observed. This is due to the sequence of the measurement steps,  
1591 which introduces a hysteresis effect and is explained in the preceding text.

1592 The collected charge drops significantly from 150 K down to 75 K. In the non-  
1593 irradiated samples the values in the lower temperature range are approximately 30 %  
1594 of the values at the high range. For the irradiated ones this difference is lower –  
1595 35 % for S79 and 50 % for S52. An interesting detail is that the ratio between the  
1596 values for non-irradiated samples and their irradiated counterparts at the lower range  
1597 is different than at the higher range. Looking at the values for the electron collection  
1598 in figure 3.17a: for S52 the lower ratio is equal to 128 % and the higher equal to  
1599 170 %. For S79 these ratios are 100 % and 109 %, which means that the difference  
1600 in charge collection between 4 K and 75 K before and after irradiation is negligible.

#### 1601 3.4.2.2 Charge trapping

1602 The carriers drifting through the bulk get stopped by the charge traps with a certain  
1603 probability. This trapping happens uniformly throughout the diamond, decreasing  
1604 the number of carriers in the charge cloud. Therefore the absolute number of trapped  
1605 carriers decreases. At the same time the absolute number of trapped carriers per unit  
1606 of length decreases. The resulting function for the number of drifting carriers per  
1607 unit of length is a decaying exponential function:

$$I(t) = I(0) \cdot e^{-\frac{t-t_0}{\tau}} + I_0, \quad (3.6)$$

1608 where  $I(0)$  is the initial induced current,  $I_0$  is the end current,  $t$  is time,  $t_0$  is temporal  
1609 displacement of the pulse and  $\tau$  is the decay time constant. This value tells how long  
1610 it takes before the amplitude of the pulse decreases to 63 % of its initial height.

1611 The decaying exponential function is fitted to the decaying top of the averaged  
1612 pulses at bias voltages of  $\pm 400$  V and  $\pm 500$  V across all temperatures excluding the  
1613 transitional range between 75 K and 150 K. The resulting decay time constants  $\tau$   
1614 for an individual temperature point are not equal, which stems from the fact that  
1615 the pulses change with time due to “polarisation”. This counts as a systematic error.  
1616 Therefore the fitted  $\tau$  for  $\pm 400$  V and  $\pm 500$  V are averaged into one value representing  
1617 the measurement at that temperature point. Figure 3.18a shows the fitted  $\tau$  for the  
1618 five samples between 4 K and 295 K. In principle the time constants should be infinite  
1619 for a perfect and non-irradiated sample. Here a slightly tilted top of the pulse due to  
1620 space charge is already successfully fitted with an exponential function (a pitfall in  
1621 an automatic analysis), resulting in a  $\tau$  of the order of  $(200 \pm 20)$  ns $^{-1}$ . Consequently  
1622 the fitting method is not adequate for non-irradiated samples. For the irradiated  
1623 samples the fit becomes increasingly more meaningful. As seen in figure 3.18a, the  
1624 fitted values of the irradiated samples are fairly stable across all temperatures. There  
1625 is a slight increase in the decay time constant of the S52 from  $(6.0 \pm 0.5)$  ns $^{-1}$  above  
1626 150 K to  $(8.5 \pm 0.9)$  ns $^{-1}$  below 75 K. On the other hand, this step is not observable  
1627 in the S79 data. With only one sample exhibiting this behaviour, the effect is not  
1628 significant enough. Judging by the data acquired, the samples would need to be

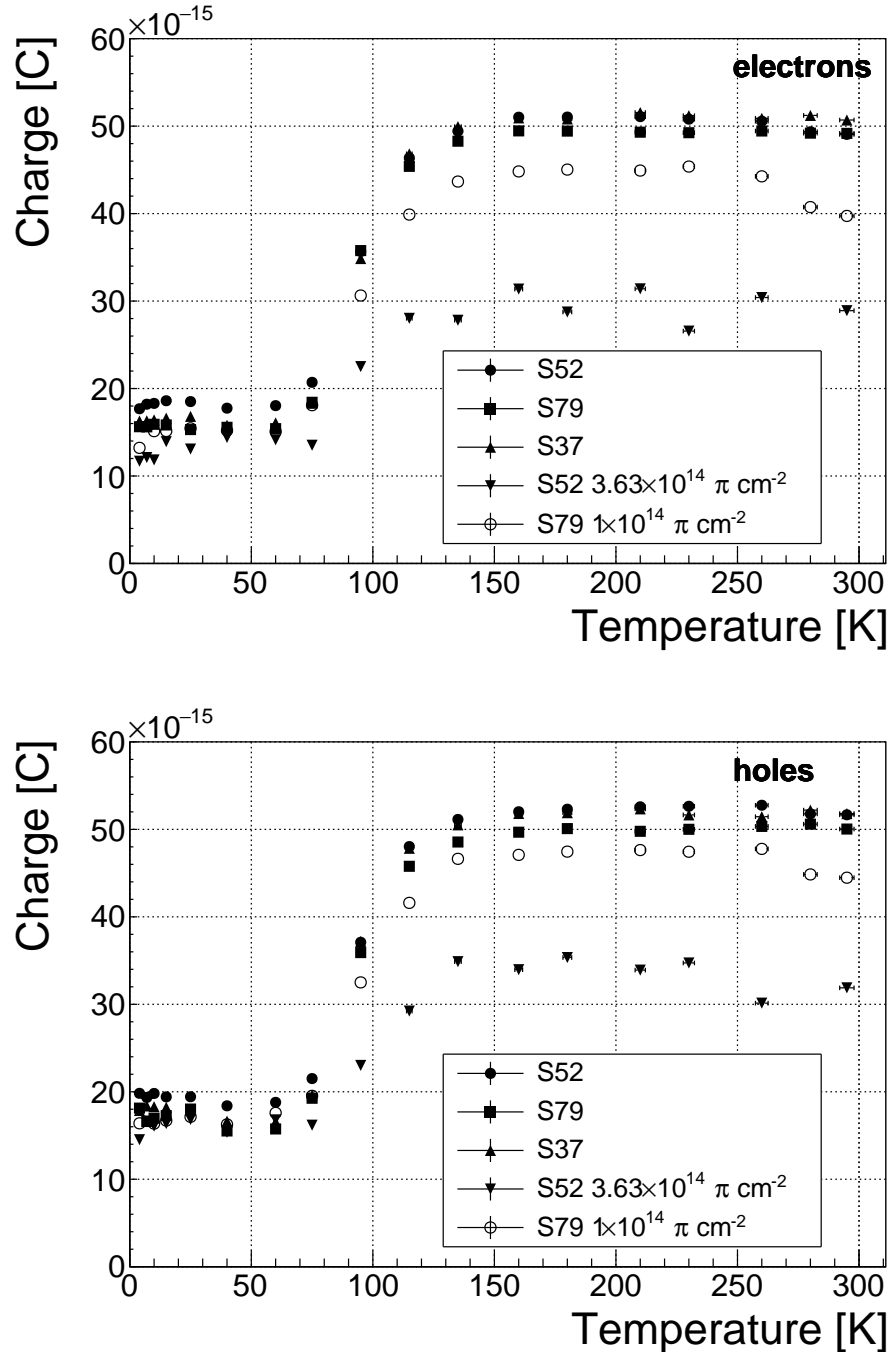


Figure 3.17: Collected charge as a function of temperature.

irradiated to doses above  $1 \times 10^{14} \pi \text{ cm}^{-2}$  to quantify this effect in detail. So far this effect is not regarded as significant for the scope of this thesis. Building on this assumption, the conclusion is that the signal decay time constant for irradiated sCVD diamond is constant across the temperature range between 4 K and 295 K, excluding the transitional range between 75 K and 150 K.

### 3.4. TEMPERATURE LIMITATIONS

Taking into account the discussion above, all the values can be averaged into one decay constant. Figure 3.18b shows these values for all samples as a function of the received  $\pi_{300 \text{ MeV}}$  radiation dose. To estimate the carrier lifetime with respect to the radiation dose received, a similar model is used than that in section 3.5. This model states that the inverse of the carrier lifetime is linearly decreasing with increasing radiation dose:

$$\frac{1}{\tau} = \frac{1}{\tau_0} + \kappa_\tau \cdot \Phi \quad (3.7)$$

$$\tau = \frac{\tau_0}{\kappa_\tau \tau_0 \Phi + 1} \quad (3.8)$$

where  $\tau_0$  is the lifetime for a non-irradiated sample (real lifetime, therefore of the order of  $400 \text{ ns}^{-1}$ ),  $\tau$  is the lifetime of an irradiated sample,  $\Phi$  is the received radiation dose and  $\kappa_\tau$  the lifetime degradation factor. For these data the fitted factor is equal to  $\kappa_\tau = (3.6 \pm 0.8) \times 10^{-16} \text{ s cm}^2 \pi_{300 \text{ MeV}}^{-1}$ . Using this factor, the steepness of the decay in the pulse shape as a function radiation dose can be estimated. This can help when designing a system where current pulse shape is an important factor.

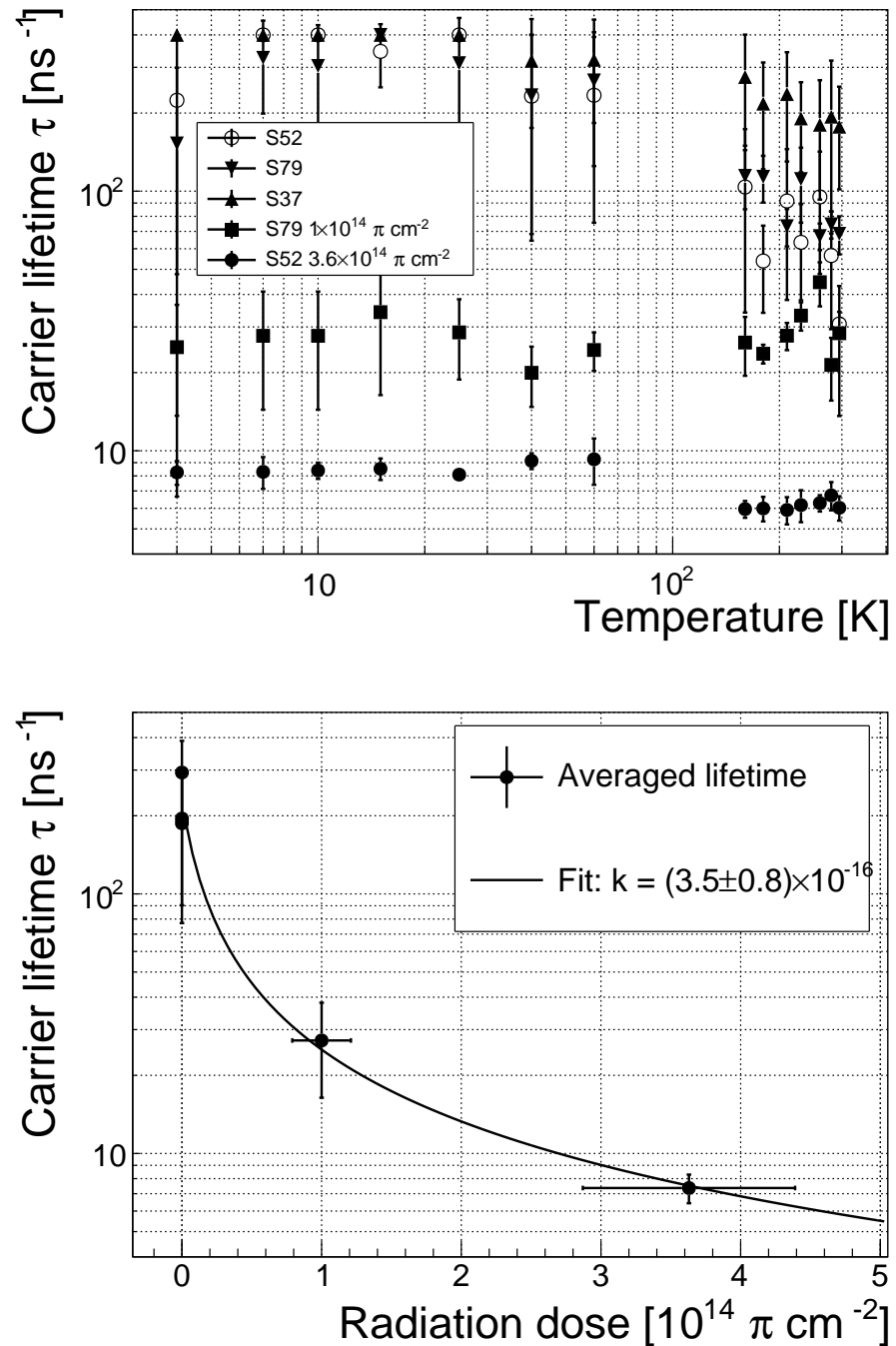


Figure 3.18: Charge carrier lifetime decreases with irradiation, but is stable across the range of temperatures between 4 K – 75 K and 150 K – 295 K. The first figure shows the carrier lifetime as a function of temperature whereas the second figure depicts the carrier lifetime averaged over all temperatures and plotted as a function of the  $\pi$  irradiation dose.

### **3.5. CONCLUSION**

---

## **3.5 Conclusion**

1648 This chapter gives an overview of the capabilities and limitations of diamond as  
1649 a particle detector. Three effects on diamond are studied – noise, radiation and  
1650 temperature, the focus being on the latter two.

1651 Two sCVD diamond detectors were irradiated with 300 MeV pions. They were  
1652 tested alongside a non-irradiated sample to observe the changes in the ability to detect  
1653  $\alpha$ ,  $\beta$  and  $\gamma$  radiation. Their charge collection efficiency was measured in a test beam  
1654 facility. The results were compared to the results from the RD42 collaboration and  
1655 a DPA model. A radiation damage factor  $k_\lambda = (4.4 \pm 1.2) \times 10^{-18} \mu\text{m}^{-1} \text{cm}^{-2}$  was  
1656 obtained for  $\pi_{300 \text{ MeV}}$  particles. The data point was not in agreement with the data  
1657 provided by RD42 nor with the model. However, the irradiation process and the low  
1658 number of tested samples hold a relatively high statistical uncertainty. In addition,  
1659 there was no diamond surface treatment done in between the measurements, as is  
1660 the case in the study conducted by RD42. The results obtained in the course of  
1661 these measurements are going to be fed into the existing pool of data in the RD42  
1662 collaboration.

1663 The next step was to test the long-term capabilities for  $\alpha$  detection. The shape  
1664 of the ionisation profile was investigated to determine the behaviour of the charge  
1665 carriers in the irradiated diamond. An exponential decay was observed in the pulses  
1666 of irradiated samples, proving that there are charge traps in the bulk that were created  
1667 during irradiation. Then a long-term stability test was carried out. The results show  
1668 that the irradiated diamond detectors do not provide a stable and reliable long-term  
1669 measurement of  $\alpha$  particles. This might be due to a space-charge build-up in the  
1670 bulk, which changes the electric field, affecting the charge carriers. A procedure to  
1671 improve the pulse shape using  $\beta$  and  $\gamma$  radiation was proposed.

1672 Finally, the diamond sensors were cooled down to temperatures between 4 K and  
1673 295 K. Their response to  $\alpha$  particles was observed. The results of the non-irradiated  
1674 and irradiated samples were compared. The effect of reduction for the number of  
1675 drifting charges due to exciton recombination was observed in both sets of data.  
1676 The second set had a superimposed effect of charge trapping during the drift, which  
1677 was represented by an exponential decay in the signal. The decay time constant  
1678 did not change with temperature. Therefore all temperature points for individual  
1679 samples were averaged and the decay time constants were plotted against the received  
1680 radiation dose. A lifetime degradation factor  $\kappa_\tau = (3.5 \pm 0.8) \times 10^{-16} \text{ s cm}^2 \pi_{300 \text{ MeV}}^{-1}$   
1681 for non-primed diamonds was defined.

1682

# Chapter 4

1683

## Charge monitoring

1684

### *The ATLAS Diamond Beam Monitor*

1685 Particle detectors in high energy physics experiments need to meet very stringent  
1686 specifications, depending on the functionality and their position in the experiment.  
1687 In particular, the detectors close to the collision point are subject to high levels of  
1688 radiation. Then, they need to operate with a high spatial and temporal segmentation  
1689 to be able to precisely measure trajectories of hundreds of particles in very short  
1690 time. In addition, they need to be highly efficient. In terms of the structure, their  
1691 active sensing material has to be thin so as not to cause the particles to scatter  
1692 or get stopped, which would worsen the measurements. This also means that they  
1693 have to have a low heat dissipation so that the cooling system dimensions can be  
1694 minimised. Finally, they need to be able to operate stably for several years without  
1695 an intervention, because they are buried deep under tonnes of material and electronics.

1696 The material of choice for the inner detector layers in the HEP experiments is  
1697 silicon. It can withstand relatively high doses of radiation, it is highly efficient (of the  
1698 order of  $\sim 99.9\%$ ) and relatively low cost due to using existing industrial processes  
1699 for its production. Its downside is that, with increasing irradiation levels, it needs to  
1700 be cooled to increasingly low temperatures to ensure a stable operation. This is not  
1701 the case with diamond. In addition, diamond has a lower radiation damage factor,  
1702 which means it can operate in a radiation-heavy environment for a longer period.

1703 The ATLAS Diamond Beam Monitor (DBM) [] is a novel high energy charged  
1704 particle detector. Its function is to measure luminosity and beam background in the  
1705 ATLAS experiment. Given its position in a region with a high radiation dose, di-  
1706 amond was chosen as the sensing material. The monitor's pCVD diamond sensors  
1707 are instrumented with pixellated FE-I4 front-end chips. The pCVD diamond sensor  
1708 material was chosen to ensure the durability of the sensors in a radiation-hard envi-  
1709 ronment and the size of its active area. The DBM is not the first diamond detector  
1710 used in HEP, but it is the largest pixellated detector installed thus far, as shown in  
1711 figure 4.1. It was designed as an upgrade to the existing luminosity monitor called the  
1712 Beam Conditions Monitor (BCM) [] consisting of eight diamond pad detectors, which

#### 4.1. LUMINOSITY MEASUREMENTS

---

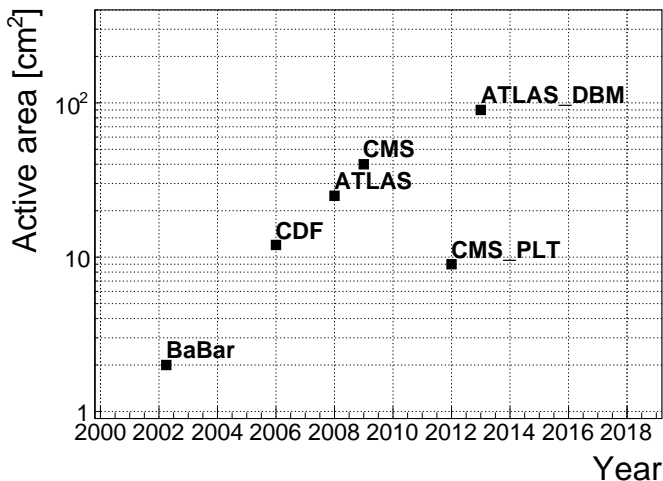


Figure 4.1: Diamond detectors installed in high-energy physics experiments in the last decade, sorted by the active sensor area. The first four detectors from the left are radiation monitors whereas the right two are pixel trackers.

is able to perform precise time-of-flight (ToF) measurements. The DBM complements the BCM's features by implementing tracking capability. Its pixelated front-end electronics significantly increase the spatial resolution of the system. Furthermore, the DBM is able to distinguish particle tracks originating in the collision region from the background hits. This capability is a result of its projective geometry pointing towards the interaction region. This chapter first describes the principles of luminosity measurements. It then explains how the DBM carries out this task. Finally, some results from tests and from the real collisions are presented.

When a particle traverses a sensor plane, a hit is recorded in the corresponding pixel. Thus, a precise spatial and timing information of the hit is extracted. With three or more sensors stacked one behind the other, it is also possible to define the particle's trajectory. This is the case with the DBM. Its projective geometry allows the particles to be tracked if they traverse the sensor planes. The DBM relates the luminosity to the number of particle tracks that originate from the collision region of the ATLAS experiment. Particles that hit the DBM from other directions are rejected as background radiation.

## 4.1 Luminosity measurements

Luminosity is one of the most important parameters of a particle collider. It is a measurement of the rate of particle collisions that are produced by two particle beams. It can be described as a function of beam parameters, such as: the number of colliding bunch pairs, the revolution frequency, the number of particles in each bunch and the transverse bunch dimensions. The first four parameters are well defined. However, the transverse bunch dimensions have to be determined experimentally

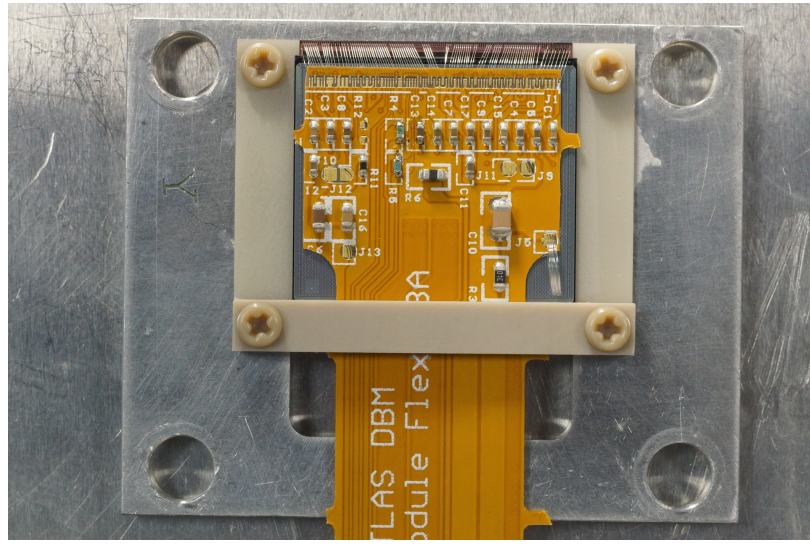


Figure 4.2: DBM module, top-down view. Visible is the flexible PCB with signal and power connections, the silicon sensor and a part of the FE-I4. Wire bonds from the PCB to the FE-I4 and to the sensor are also visible.

1736 during calibration. The ATLAS experiment uses the *van der Meer scan* [] during  
1737 low-luminosity runs to calibrate the luminosity detectors. This scan is performed  
1738 by displacing one beam in a given direction and measuring the rate of interactions  
1739 as a function of the displacement. Transverse charge density of the bunches can be  
1740 estimated on the basis of the interaction rate. The calibrated luminosity detectors  
1741 can then operate during high-luminosity runs.

1742 One approach to luminosity monitoring is to count the number of particles pro-  
1743 duced by the collisions. The luminosity is then proportional to the number of detected  
1744 particles. A detector has to be capable of distinguishing individual particles that fly  
1745 from the interaction point through the active sensor area. If the detector has at least  
1746 three layers, it can reconstruct the particles' tracks, which in turn yields more infor-  
1747 mation on their trajectory. This is one reason why detectors with a high timing-  
1748 and spatial segmentation are more suitable for these applications. The second reason  
1749 is that, with a high spatial segmentation, the detector does not saturate even at high  
1750 particle fluencies.

## 1751 4.2 Diamond pixel module

1752 The two most important parts of the diamond pixel module, which is shown in fig-  
1753 ure 4.2, are the sensor, which detects ionising radiation, and the pixellated front-end  
1754 chip, which collects the ionised charge with a high spatial segmentation, processes the  
1755 recorded data and sends them to the readout system. This section describes these  
1756 two main parts of the module and their interconnection.

## 4.2. DIAMOND PIXEL MODULE

---

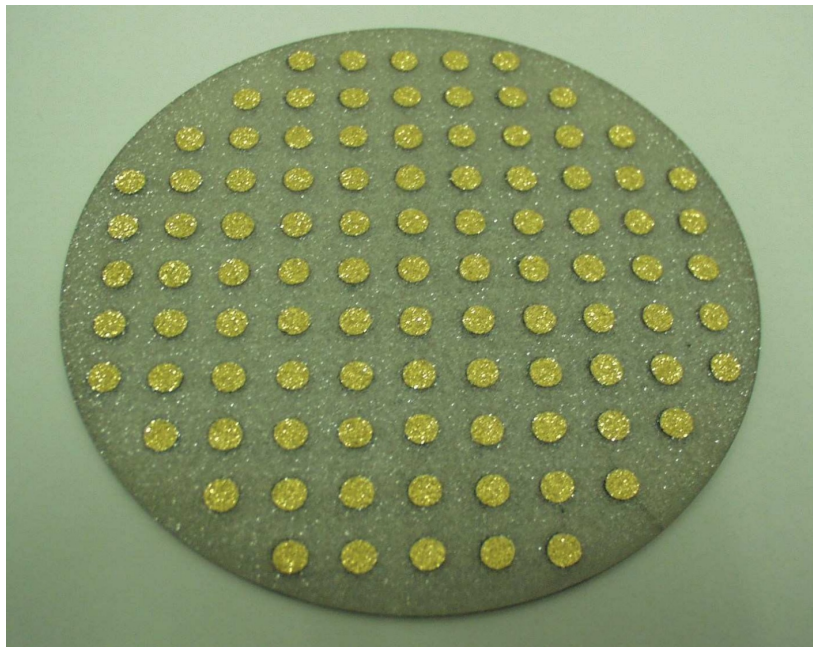


Figure 4.3: A pCVD wafer. The golden dots on the surface are the electrodes that are applied during the qualification test. The wafer is measured across the surface to find the regions with the highest efficiency.

### 1757 4.2.1 Sensors

1758 The DBM modules are instrumented with two types of sensors – pCVD diamond and  
1759 silicon. The silicon sensors are used as a fallback solution because there were simply  
1760 not enough high-quality diamond sensors available. In addition, a comparative study  
1761 of irradiation damage between silicon and diamond can be made with such a hybrid  
1762 system.

1763 **Diamond sensors** The target material for this application is pVCD diamond. The  
1764 reason for this is that the active area of an individual sensor must be approximately  
1765  $4 \text{ cm}^2$ , which is too large for the sCVD diamond. pCVD material is also a bit  
1766 cheaper, which makes a detector with a large active area more feasible to build. The  
1767 material is provided by three companies: DDL, E6 and II-IV and it is grown in  
1768 15 cm wafers, as seen in figure 4.3. The target thickness of the wafers is 500  $\mu\text{m}$  and  
1769 the minimum required charge collection efficiency is 40 % ( $\text{CCD} \geq 200 \mu\text{m}$ ). They  
1770 need to be operated at bias voltages between 600–1000 V. On one side there is a  
1771 single gold electrode applied across the entire surface. On the other side a pixellated  
1772 metallisation is added.

1773 **Silicon sensors** are standard  $n^+ - in - n$  planar sensors with a 200  $\mu\text{m}$  thickness  
1774 and were mostly fabricated at CiS [], a company from Ertfurt, Germany. They are  
1775 designed to have nearly a 100 % efficiency when non-irradiated. Their bulk resistivity  
1776 is between 2–5  $\text{k}\Omega\text{cm}$  and they were diffusion oxygenated at 1150 °C for 24 hours to

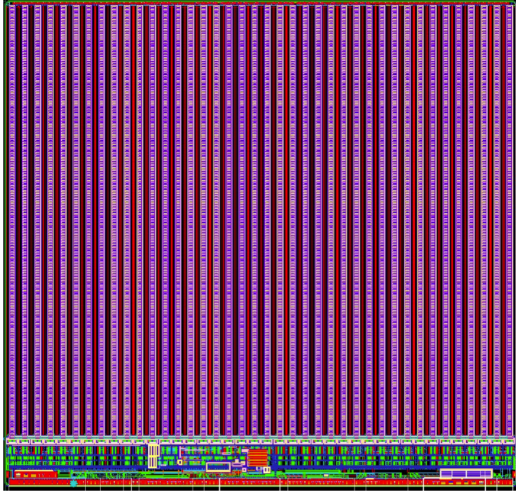


Figure 4.4: FE-I4 layout, top-down view. The pink area are pixels grouped into columns, the green area below is the common logic and the red strip at the bottom are the wire bond pads.

increase their radiation hardness. One side is segmented into pixels. Guard rings at the edges of the sensor provide a controlled drop in potential, reducing the possibility of shorts at maximum design bias voltages of the order of 1000 V.

### 4.2.2 Front-end electronics

The FE-I4 (front-end version four) [1] is an ASIC pixel chip designed specifically for the ATLAS pixel detector upgrade. It is built as a successor to the current pixel chip FE-I3, surpassing it in size of the active area ( $4\times$  larger) as well as the number of channels/pixels ( $10\times$  more). 336 such FE-I4 modules are used in the newly installed pixel layer called the Insertable B-Layer (IBL) [2]. The DBM is also instrumented with these chips. The FE-I4's integrated circuit contains readout circuitry for 26880 pixels arranged in 80 columns on a  $250\text{ }\mu\text{m}$  pitch and 336 rows on a  $50\text{ }\mu\text{m}$  pitch. The size of the active area is therefore  $20.0\times16.8\text{ mm}^2$ . This fine granularity allows for a high-precision particle tracking. The chip operates at 40 MHz with a 25 ns acquisition window, which corresponds to the spacing of the particle bunches in the LHC. It is hence able to correlate hits/tracks to their corresponding bunch. Furthermore, each pixel is capable of measuring the deposited charge of a detected particle by using the Time-over-Threshold (ToT) method. Finally, the FEI4 has been designed to withstand a radiation dose up to 300 MGy. This ensures a longterm stability in the radiation hard forward region of the ATLAS experiment.

Each pixel is designed as a separate entity. Its electrical chain is shown in figure 4.5. The bump-bond pad – the connection to the outside of the chip – is the input of the electrical chain, connected to a free-running amplification stage with adjustable shaping using a 4-bit register at the feedback branch. The analog amplifier is designed to collect negative charge, therefore electrons. The output is routed through

## 4.2. DIAMOND PIXEL MODULE

---

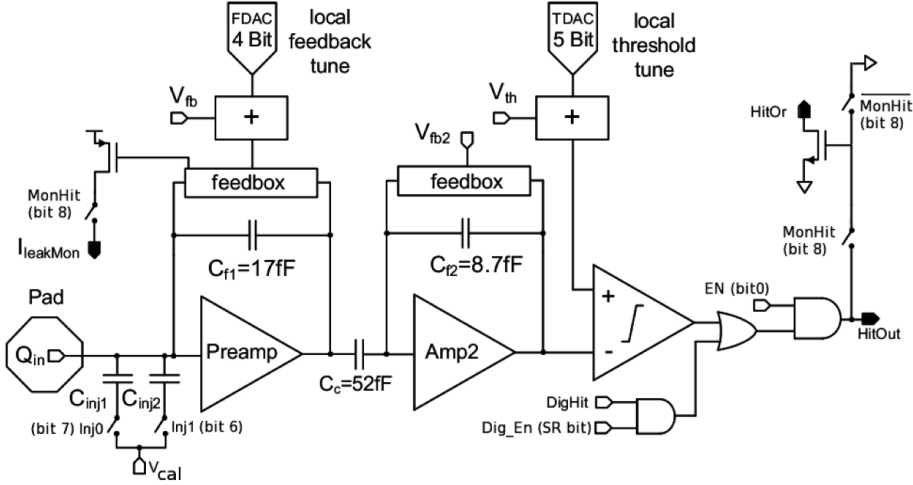


Figure 4.5: Schematic of an analog pixel. Courtesy of the FE-I4 collaboration.

1801 a discriminator with an adjustable threshold. This value in effect defines the level  
 1802 at which the circuit detects a hit. In addition, there is a counter of the clock cycles  
 1803 (25 ns sampling) during which the signal is above the discriminator threshold. The  
 1804 value of the counter is proportional to the collected charge. The logic gates at the end  
 1805 of the chain are used to enable/disable the pixel and to issue a so-called HitOr flag –  
 1806 this signal is set whenever at least one of the pixels was hit and is used as a trigger  
 1807 for the readout. The output of the chain – HitOut – is routed into the logic of the  
 1808 chip where it is buffered and eventually sent out to the readout system. The module  
 1809 receives all its commands from the system via a 40 MHz LVDS line. The commands  
 1810 are either settings for the pixel registers or triggers that start the data readout. The  
 1811 data are sent via an LVDS line at up to 320 Mbit/s, but by default at 160 Mbit/s,  
 1812 four times faster than the clock of the device. This allows the chip to clear out its  
 1813 buffers before new data are recorded, thus avoiding dead time and data pile-up. The  
 1814 FE-I4 has been successfully tested for trigger rates of up to 300 kHz.

1815 The DBM uses pCVD diamond with  $d_C = 500 \mu\text{m}$  thickness and silicon with  
 1816  $d_{Si} = 200 \mu\text{m}$  thickness as a sensor material. The resulting most probable value  
 1817 (MPV) of the deposited charge for a minimum ionising particle (MIP) is calculated  
 1818 with the formula  $Q_s = d \cdot E_{e-h}$  and equals 18000 electrons and 17800 electrons,  
 1819 respectively, at a full charge collection efficiency. Unfortunately this is not the case  
 1820 with the pCVD material, whereby the expected charge collection efficiency is of the  
 1821 order of 50 % – around 9000 e. This value further decreases with received irradiation  
 1822 dose. Therefore in order to detect the particles depositing energy on the far left side  
 1823 of the landau spectrum, the threshold has to be set to a significantly lower value.  
 1824 On the other hand, if the threshold set too low, it also detects the electronic noise  
 1825 and stores a false noisy hit. With the typical noise amplitudes being in the range of  
 1826 120–200 e, a safe threshold range would be between  $Th = 1000\text{--}3000$  e. The target  
 1827 for the DBM is to lower the threshold down to 800 e.

The analog amplifier is implemented in two stages to get a fast rise time at a low noise and a low power consumption. The output signal of the analog amplifier has a triangular shape with a fast rise time and a long decay. The shape can be adjusted by tuning the amplifier feedback loop. Its length is proportional to the collected charge, but it needs to be calibrated first. This is done by means of two injection capacitors,  $C_{\text{inj}1}$  and  $C_{\text{inj}2}$ , seen in figure 4.5 with well defined capacitances. First, the charge  $Q_{\text{cal}} = V_{\text{cal}} \cdot (C_{\text{inj}1} + C_{\text{inj}2})$  is injected into the analog chain. Then the length of the output pulse is measured and finally the feedback value is changed to either lengthen or shorten the pulse in order to get to the required duration  $t_{\text{cal}}$ . The typical values are  $Q_{\text{cal}} = 5000 - 16000$  e at the time  $t_{\text{cal}} = 5 - 10$  ToT. The target values depend on the sensor, the type of a radioactive source and the application. Therefore the initial threshold  $Th$  at 1 ToT and the calibrated value  $Q_{\text{cal}}$  at  $t_{\text{cal}}$  ToT give us a linear scale of collected charge with respect to time over threshold. However, in practice this relation is nonlinear for lower thresholds, but since the goal of the measurements is to track the particles rather than to measure their deposited energy precisely, this is sufficient.

## 4.3 Module assembly and quality control

Parts for the detector arrived separately and were assembled into modules at CERN’s DSF lab after being checked for production faults. The assembled modules underwent a series of quality control (QC) and burn-in tests to determine their quality, efficiency and long-term stability.

### 4.3.1 Assembly

A single-chip module consists of a pixel module, a flexible PCB and the supporting mechanics (a ceramic plate and an aluminium plate). The chip arrives already bump-bonded to the sensor, be it diamond or silicon. First it is glued to the ceramic plate on one side and to the PCB on the other using either Araldite 2011 or Staystik 672/472. The choice of glue was a topic of a lengthy discussion. Staystik is re-workable and has a very high thermal conductivity. The latter is important because the FE-I4 chips tend to heat up significantly and need a good heat sink. The problem is that it has a curing temperature of 160/170 °C. This temperature may cause some unwanted stress build-up between the FE-I4 and the diamond sensor due to different coefficients of thermal expansion, pulling them apart. This would disconnect the pixels, yielding large regions of the module insensitive to radiation. To avoid this, an alternative glue was tried. Araldite 2011 can be cured at lower temperatures – down to RT – but it has a lower heat conductivity. In the end Araldite is used as the safer option. However, due to the longer curing, the entire assembly process using Araldite is extended to two working days. After curing, the module is wire-bonded and attached to the aluminium plate using screws made up of a radiation-resistant PEEK plastic. They have to be tightened with a great care, because their screw head is only 0.2–0.6 mm

#### 4.3. MODULE ASSEMBLY AND QUALITY CONTROL

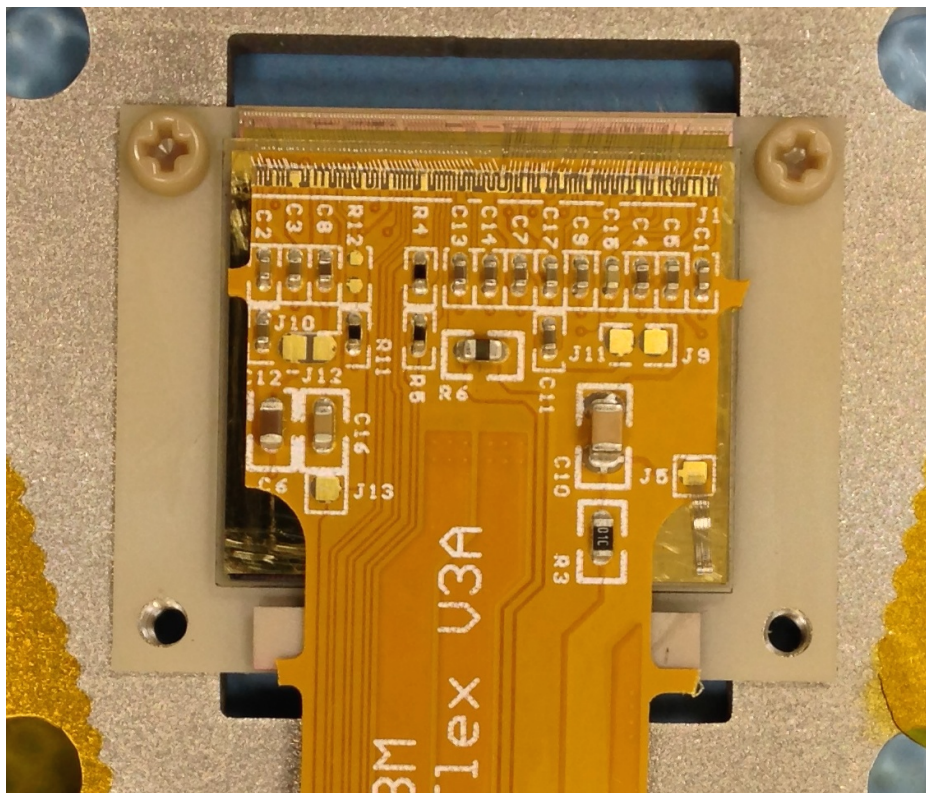


Figure 4.6: An assembled DBM module.

away from the sensor edge – the sensor displacement tolerance during gluing is of the order of 0.5 mm. Finally, the module is put in an aluminium carrier which protects it from mechanical damage or electrostatic discharges. Figure ?? shows an assembled module.

### 1871 4.3.2 Testing

1872 The modules are tested in the lab using an RCE readout system and a moving stage  
1873 with two degrees of freedom. They are placed onto the stage and connected to the  
1874 readout system and the power supplies. After ensuring the low- and high voltage  
1875 connectivity they are checked for the signal connectivity. If everything is operational,  
1876 a series of automated tests is run. Each of these tests calibrates a certain value within  
1877 a pixel, whether it is the signal threshold or the value for integrated charge. These  
1878 are tuned in a way that the response to a predefined calibration signal is uniform for  
1879 all pixels across the sensor. This procedure is referred to as *tuning*.

When the modules are tuned, they are tested using a  $^{90}\text{Sr}$  radioactive source. Two things are checked: 1) operation of all pixels and 2) sensor efficiency. The first test is carried out by moving the module slowly under the source while taking data so that the entire surface is scanned uniformly. The resulting occupancy map reveals any pixels that are not electrically coupled to the sensor via bump bonds. This is an important step in the DBM QC procedure, because it turned out that a significant

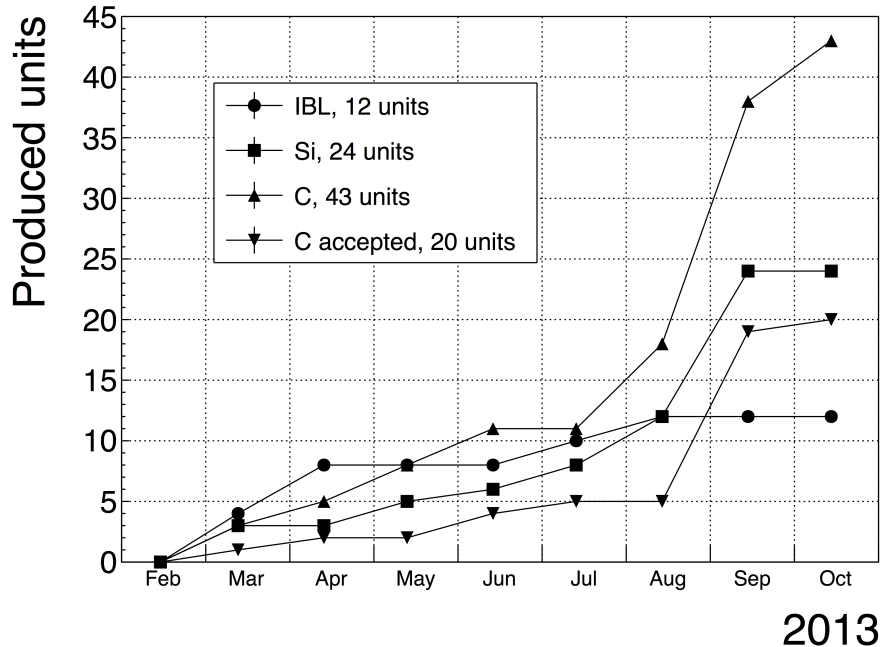


Figure 4.7: Module production with time.

portion of the flip-chipped diamond sensors exhibited very poor connectivity. The disconnected regions on the faulty modules ranged anywhere from 0.5–80 % of the overall active surface. In two cases the sensor was even completely detached from the chip. Therefore the pixel connectivity turns out to be the most important qualification factor in the QC procedure. Unfortunately the only way to check it at the moment is to fully assemble a module and test it using a radioactive source. If the module turns out to be of poor quality, it is disassembled and sent for rework. The turnover time of this operation is of the order of one month, which affected the DBM installation schedule significantly.

Only the modules that passed the pixel connectivity test undergo the second test stage in which the sensor’s efficiency was estimated. A scintillator is placed underneath the module and is used as a trigger. A particle that crosses the DBM module and hits the scintillator, triggers the module readout. In the end, the number of triggers is compared to the number of hits/clusters recorded by the module. The resulting ratio gives an estimate of the sensor’s detection efficiency. The real sensor efficiency can only be measured in a particle beam and using a beam telescope as a reference detector. Nonetheless, the *pseudo-efficiency* gives a rough estimate of the sensor’s quality.

The results for the DBM QC are shown in section 4.4. All in all, 79 modules went through the QC procedure – 43 diamond modules and 36 silicon modules, 12 of the latter only for testing purposes. Figure 4.7 shows their production with time. 18 diamond modules and 6 silicon modules were in the end chosen to be made up into DBM telescopes and installed into ATLAS.

### **4.3. MODULE ASSEMBLY AND QUALITY CONTROL**

---

1909 A very important issue is the so called erratic current. This term describes the  
1910 leakage current in a pCVD diamond that becomes unstable. It can develop gradually  
1911 or can be triggered with a  $\beta$  source. Spikes appear in the otherwise stable leakage  
1912 current. They can be up to three orders of magnitude higher than the base current.  
1913 Sometimes the current also suddenly increases for a few orders of magnitude and stays  
1914 at that level (e.g. from the initial 1 nA to 3  $\mu$ A). The amplitude differs in magnitude  
1915 from sensor to sensor. This effect is still not fully explained, but the hypothesis  
1916 is that the charges find a conductive channel along the grain boundaries, causing  
1917 discharges. These discharges are picked up by the pixel amplifiers in the FE-I4. A  
1918 single discharge can trigger a group of up to  $\sim$ 500 pixels, resulting in a *blob* on the  
1919 detector occupancy map. Sometimes the conductive channel stays in a conductive  
1920 state, making one or more pixels always to fire. These pixels only use the bandwidth  
1921 of the readout channel, so they have to be masked out during measurements.

#### **1922 4.3.3 Installation and commissioning**

1923 The DBM modules that passed the QC tests were assembled into telescopes – sets of  
1924 three modules one behind the other with a spacing of 50 mm. Of the 18 diamond and  
1925 6 silicon modules, 6 diamond and 2 silicon modules were built. A special care was  
1926 taken when choosing the sets of three diamonds. The modules with a similar pseudo-  
1927 efficiency, leakage current, maximum stable high voltage and shape of disconnected  
1928 regions were grouped together. After assembly into telescopes, the modules were  
1929 tested for their connectivity. Then the high voltage was applied and the leakage  
1930 current was observed. This was an important point to check because all three modules  
1931 shared the same high voltage channel. Any instabilities on one of the modules would  
1932 cause problems on the other two. This would for instance happen if one of the modules  
1933 had a much lower breakdown voltage.

1934 Due to time constraints, the telescopes were not built at the same time but in-  
1935 stead the production was pipelined. As soon as two telescopes were ready, they were  
1936 transported to Point 1 – the site where parts of the ATLAS detector were being put  
1937 together. There they were prepared for installation onto the pixel detector struc-  
1938 ture that had been extracted from ATLAS due to pixel detector commissioning. The  
1939 commissioning was nearing completion, so the technicians were preparing the detec-  
1940 tor for re-insertion. The cylindrical structure was being closed off by four new service  
1941 quarter-panels (nSQPs). This meant that with every day the access to the place  
1942 of installation of the DBM was more difficult. The first two telescopes were still put  
1943 into place when only one nSQP was in place. This allowed the installation process  
1944 to be carried out from both sides. This proved to be helpful, because the process  
1945 was lengthy and had to be done with great precision. It involved tightening several  
1946 screws on both sides of the telescopes, adding thermal paste on the aluminium joints  
1947 and removing the protective covers, revealing the fragile wire bonds. At the same  
1948 time the surrounding electronics and cables had to be left untouched. The lessons  
1949 learnt with the first part of the installation were helpful when installing the other tele-

scopes. The last two were fitted onto the structure when three nSQPs were already in place, leaving only a narrow opening for access. The entire procedure was carried out blind. After every installation, the telescopes were tested again. First, the low voltage connectivity was checked and a set of tests was run on the FE-I4 front-end chips. An eye diagram was made to estimate the quality of the signal transmission. Then a  $^{90}\text{Sr}$  source was used to perform a source test on three modules at the same time. Leakage current was observed during the source test. The final test included running four telescopes (all on one side) at a time. All the tests were successful and the DBM was signed off.

## 4.4 Performance results

This section gives an overview of the performance results of the DBM modules achieved during the QC and the test beam campaign. The source tests were performed to check for disconnected regions in the sensors and to measure the diamond's pseudo-efficiency. Only the modules with minimal disconnected regions and maximum pseudo-efficiency were chosen for installation.

### 4.4.1 Source tests

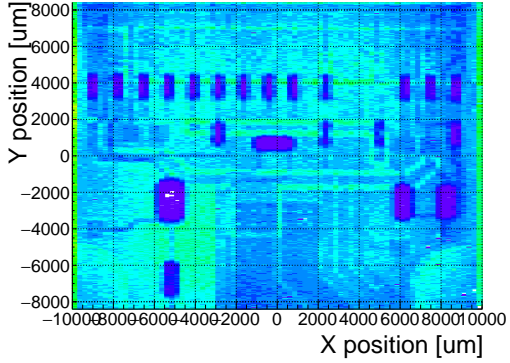
All modules went through the same procedure when tested using a  $^{90}\text{Sr}$  source – to check for disconnected regions and to measure the pseudo-efficiency.

The setup consisted of a placeholder for the  $^{90}\text{Sr}$  source, an X-Y moving stage with a holder for the module and a scintillator with a photomultiplier placed below the source and the module. The scintillator was used as a trigger – when it detected a particle, it triggered the readout of the module. If the module was placed in between the source and the scintillator, the particle had to traverse the module to hit the scintillator. Therefore, in the case of a module with a 100 % efficiency the triggered data read out by the module would need to contain at least one hit in the module. In reality the  $\beta$  particles scatter around the setup and sometimes hit the scintillator from other directions, without incident the module. This produces empty triggers. The phenomenon sets the limitation of measuring with a radioactive source as compared to the measurements in a test beam, in which the particles in principle always travel in one direction and their scattering is minimal.

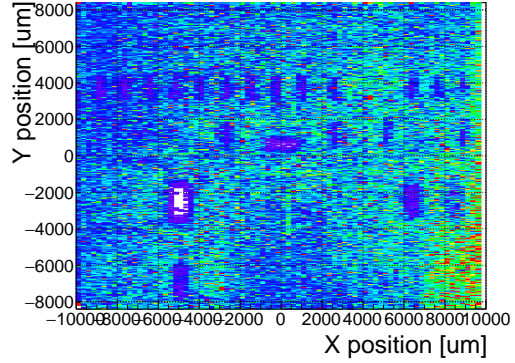
The test for disconnected regions was carried out by moving the module under the source in X and Y direction so that the exposure over the entire plane was uniform. This resulted in an occupancy scan seen in figures 4.8a and 4.8b. The silicon module had a very uniform occupancy plot. So much so that the features of the overlaying flexible PCB can be observed. The rectangular shadows are the passive components whereas the lines are the traces in the PCB. Furthermore, a circular-shaped edge of the PCB can be seen on the bottom right side of the plot. These darker areas are such because fewer electrons can penetrate the material with a high density. In the case of the diamond, the features of the PCB can be observed as well, but are much

#### 4.4. PERFORMANCE RESULTS

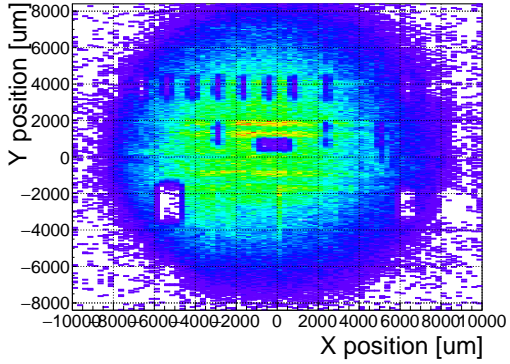
---



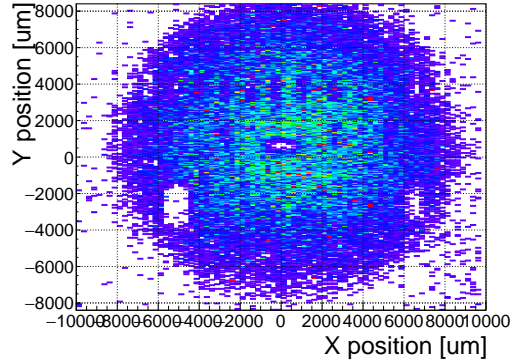
(a) Occupancy scan for MSBM-34.



(b) Occupancy scan for MDBM-23.



(c) Pseudo-efficiency scan for MSBM-34.



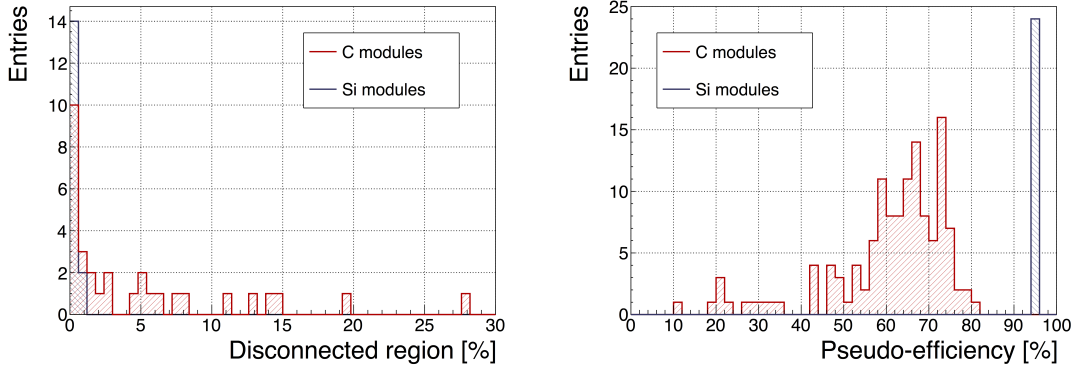
(d) Pseudo-efficiency scan for MDBM-23.

Figure 4.8: Occupancy and pseudo-efficiency scans for the silicon (left) and diamond sensor (right) to check for disconnected regions and estimate the sensor's efficiency. Shadows of the electronic components are clearly visible because fewer electrons were able to traverse through such a higher amount of material.

1989 less distinguishable. In principle, the plot is much more granulated – less uniform.  
 1990 This high variance in the diamond's detection ability is due to the grain boundaries  
 1991 in the pCVD material which trap the drifting charges, rendering some regions much  
 1992 less efficient.

1993 The pseudo-efficiency test was carried out by placing the module directly below the  
 1994 source and collimating the particles so that their trajectory was incident the module  
 1995 in the middle. For every trigger by the scintillator, a script checked whether there  
 1996 was a hit recorded in the module or not. The resulting ratio between the number  
 1997 of triggers and number of hits recorded in the module is a pseudo-efficiency – an  
 1998 estimation of the sensor's efficiency. It cannot give a precise value due to the triggers  
 1999 produced by scattered particles, but at least gives a rough estimate.

2000 Figure 4.9a shows the distribution of disconnected regions across all tested mod-  
 2001 ules. Silicon modules were performing as expected, with a minimum number of dis-  
 2002 connected pixels. The majority of the silicon modules yielded the pseudo-efficiency  
 2003 of  $(94.3 \pm 0.2)\%$ . Silicon sensors being 99.99 % efficient, this value was underesti-



(a) Disconnected regions for all modules derived from the occupancy scans. (b) Pseudo-efficiencies for all modules at various threshold and voltage settings.

Figure 4.9: Measurements of pseudo-efficiency and disconnected regions for all modules that went through the QC procedure.

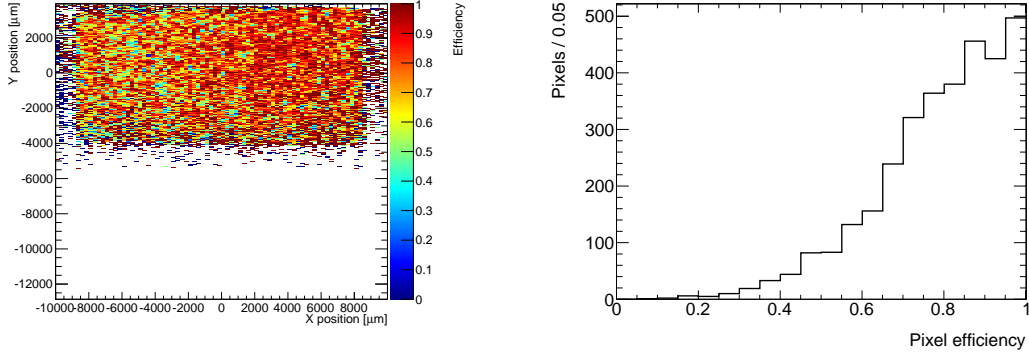
mated by about 5 %. The measured pseudo-efficiency of the diamond modules was (65  $\pm$  7) %, with outliers down to 10 %. The value depended on the diamond quality, the set threshold and the applied bias voltage. The latter two settings were varied to check the behaviour of the modules under various conditions.

#### 4.4.2 Test beam results

The first two assembled prototype DBM modules, MDBM-01 and MDBM-03, were tested at DESY, Hamburg, in a test beam facility. The aim of the measurements was to measure their efficiency, the spatial distribution of the efficiency and the effect of the beam on the disconnected regions. A silicon module MSBM-02 was measured to crosscheck the measurements. Since the silicon module is almost 100 % efficient, it was used as an “anchor” – the efficiency of the diamond module was measured relative to that of the silicon module. Two beam telescopes were used as reference systems: Kartel [], built by JSI institute from Ljubljana, and EUDET Aconite []. Both are instrumented with six Mimosa26 pixel planes and capable of tracking particles with a 2  $\mu\text{m}$  pointing resolution.

The test beam prototypes did not meet the acceptance criteria for production DBM modules in the following areas: first, the stated CCDs were slightly below 200  $\mu\text{m}$ , which would be the DBM minimum. Secondly, the applied bias voltages ranged from 1–2 V/ $\mu\text{m}$ . In addition, the threshold cut could only be set to 1500 electrons, which is higher than the DBM minimum (1000 e). Nonetheless, the resulting module efficiencies were still in the range between 70–85 %.

To analyse the test beam data, Judith [] software framework was used. Judith is capable of synchronising data streams from several detector systems only connected via a trigger system, reconstructing tracks and calculating efficiency for the DUTs. It was also used to reconstruct and analyse the acquired Kartel test beam data together



(a) This is an efficiency distribution. Each bin corresponds to a single pixel. The triggering scintillator of the Kartel telescope was smaller than the DUT. Hence, the recorded hits can only be seen in the top half of the sensor.

(b) Pseudo-efficiencies for all modules at various threshold and voltage settings.

Figure 4.10: An efficiency study of a prototype DBM diamond module in a test beam. The statistics are low ( $\sim 10$  hits/pixel) as the data was collected during a short run.

2029 with the silicon and diamond module as DUTs. A sample of the analysed data is  
2030 shown in figures 4.10a and 4.10b.

## 2031 4.5 Operation

### 2032 4.5.1 Positioning

2033 The DBM is placed in the forward region of the ATLAS detector very close to the  
2034 beam pipe, as shown in figure 4.12. The mechanical structure that holds the sensor  
2035 planes is, due to its shape, referred to as a DBM telescope. A telescope is a system  
2036 that consists of several pixel sensors placed in series one behind the other. Each  
2037 DBM telescope houses three diamond pixel modules. Eight DBM telescopes reside  
2038 approximately 1 m away from the collision region, four on each side. They are tilted  
2039 with respect to the beam pipe for 10°. This is due to a specific phenomenon con-  
2040 nected to erratic (dark) currents in diamond. Studies have shown [] that the erratic  
2041 leakage currents that gradually develop in diamond can be suppressed under certain  
2042 conditions. For instance, if a strong magnetic field is applied perpendicular to the  
2043 electric field lines in the diamond bulk, the leakage current stabilises []. The DBM  
2044 was designed to exploit this phenomenon. The magnetic field lines in the ATLAS  
2045 experiment are parallel to the beam. Hence, an angular displacement of the sensor  
2046 with respect to the beam allows for the leakage current suppression. However, the  
2047 DBM telescopes still need to be directed towards the interaction region. Taking these  
2048 considerations into account, a 10° angle with respect to the beam pipe was chosen.  
2049 The influence of the magnetic field on the particle tracks at this angle is very low  
2050 as the field lines are almost parallel to the tracks. The tracks are therefore straight,



Figure 4.11: This photo highlights four telescopes installed onto the nSQPs and around the pipe.

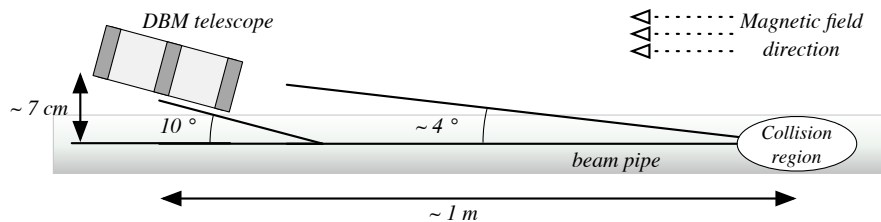


Figure 4.12: Position of the DBM in the ATLAS experiment.

2051 which reduces the track reconstruction complexity.

### 2052 4.5.2 Data taking during collisions

2053 The DBM has been commissioned in ATLAS and is now taking data. Several issues  
 2054 still need to be resolved regarding the readout systems. Unfortunately, due to issues  
 2055 with the low voltage power supply regulators, six out of 24 modules were damaged  
 2056 during operation: four silicon and two diamond modules. The system configured  
 2057 the modules into an unsteady state whereby they drew twice as much current as the  
 2058 allowed maximum. This current most probably fused the wire bonds within minutes.

## 4.5. OPERATION

---

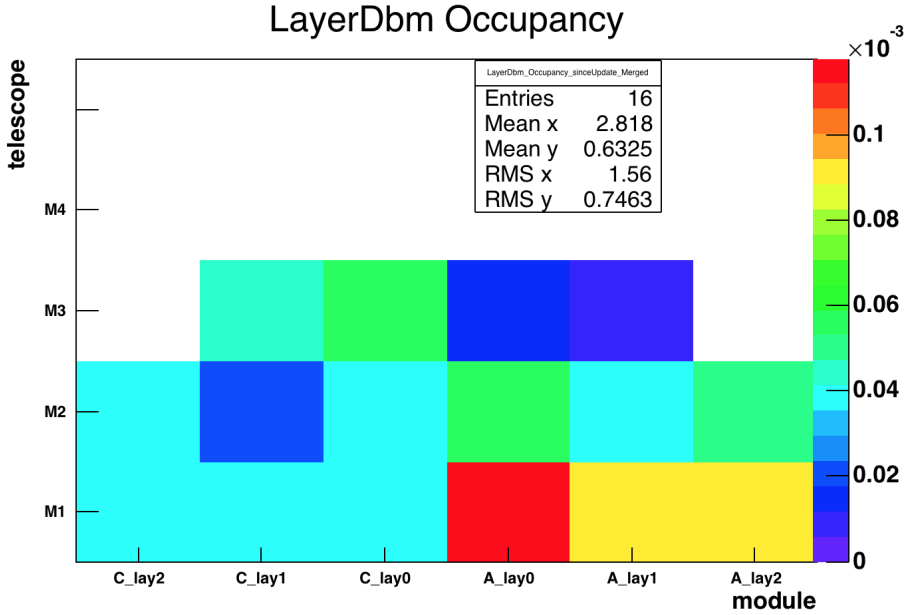


Figure 4.13: Occupancy of individual modules during collisions. Only 16 modules were taking data.

2059 This has left only five diamond telescopes fully operational. The preliminary data  
 2060 obtained using the remaining telescopes show that the background rejection could  
 2061 indeed work.

2062 The first step of the system test was to take data during collisions and check  
 2063 the occupancy in the individual modules. The occupancies were plotted side by side  
 2064 for comparison. Figure 4.13 shows some of the occupancy values. At the time, the  
 2065 readout system was not yet configured to read out all telescopes in parallel.

2066 The second step was to test the detector's capability of particle tracking. Only one  
 2067 telescope was used to take data with the beam. If all three planes of the telescope  
 2068 were hit during a bunch crossing, a linear line was fitted to the hits. This line  
 2069 represented the particle's trajectory. It was projected towards the interaction point.  
 2070 Two parameters were calculated where the line is the closest to the interaction point:  
 2071 the radial distance and the longitudinal distance between the line and the interaction  
 2072 point, as shown in figure 4.14. This was done for the events with two colliding bunches  
 2073 as well as for events with only one, non-colliding bunch. The tracks recorded during  
 2074 the events with two colliding bunches could either come from the collisions or could  
 2075 be background scattering. Tracks recorded during a non-colliding bunch, on the  
 2076 other hand, are definitely background particles since, in principle, there should be no  
 2077 collisions taking place.

2078 A comparison of the data acquired and depicted in figures 4.15a and 4.15b showed  
 2079 that, for the colliding bunches, the majority of the reconstructed tracks had the origin  
 2080 in the interaction point, with an expected spread in  $Z$  and  $R$ . For non-colliding  
 2081 bunches, the distribution is more spread out. In the  $Z_0$  plot the distribution has one

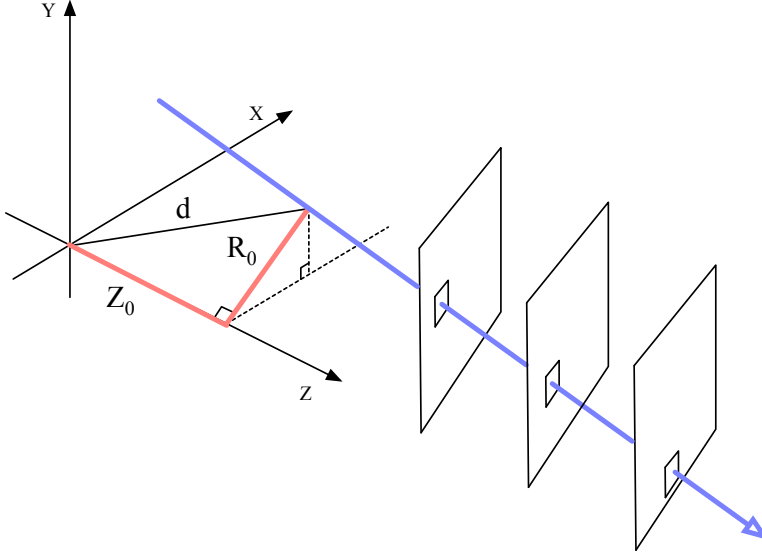


Figure 4.14: A diagram showing the radial distance  $R_0$  and longitudinal distance  $Z_0$  of the trajectory from the interaction point at the minimal distance  $d$ .  $Z$  is the axis along the beam line. Three module planes intercept a particle and reconstruct its trajectory.

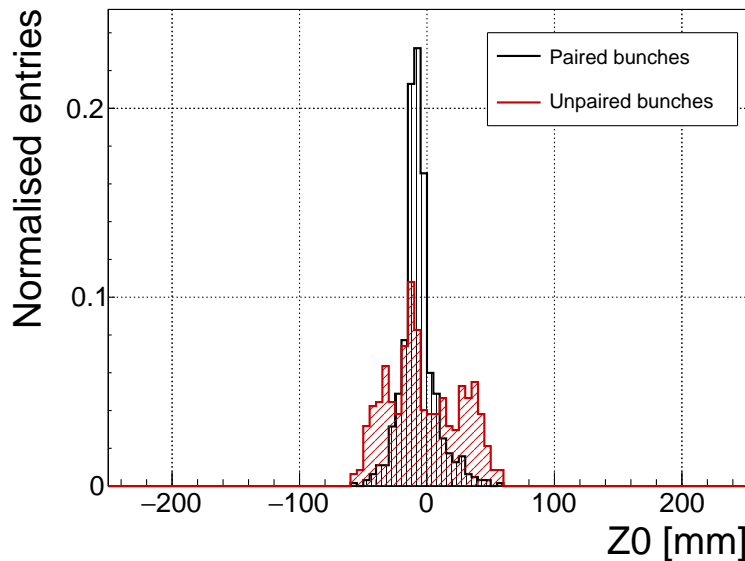
peak in the middle, which means that the empty RF buckets still held some particles. The two peaks on the sides, however, show that a significant number of tracks had their origin at the radius of the beam pipe. Therefore these tracks were made by stray protons colliding with the beam pipe. These collisions are unwanted as they do not produce any meaningful physics while still damaging the ATLAS detector by means of the scattered radiation.

## 4.6 Conclusion

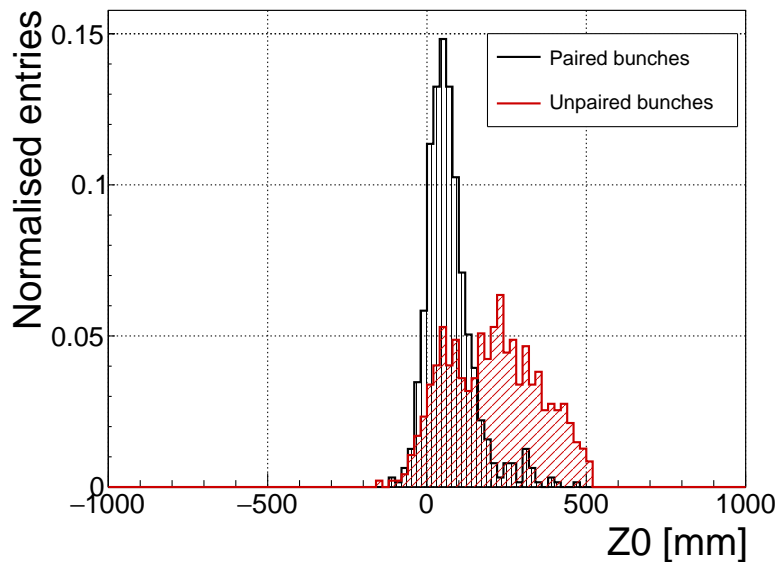
The Diamond Beam Monitor has been designed as an upgrade to the existing luminosity detectors in the ATLAS experiment. It is the first diamond pixel tracking detector installed in a high-energy physics experiment. The pixelated front-end electronic chips ensure precise spatial detection of the charged high-energy particles. The projective geometry allows for particle tracking and background rejection. The detector is placed in a high-radiation forward region of the experiment. Therefore, radiation hardness of the chosen pCVD diamond sensors is an important requirement. The tests carried out in the test beam and in the laboratory confirmed that enough detector-grade DBM modules have been built to be installed in the experiment. The DBM is now running in ATLAS during collisions. Further improvements have to be made on the readout firmware before it is included in the main readout stream.

#### 4.6. CONCLUSION

---



(a) Radial distance of the particle trajectories from the interaction point.



(b) Longitudinal distance of the particle trajectories (along the beam path) from the interaction point.

Figure 4.15: These two plots show two parameters of particle tracks recorded by one of the DBM telescopes: radial and longitudinal distance of the projected tracks from the interaction point.

2100

# Chapter 5

2101

## Current monitoring

2102

### *Real-time particle identification*

2103 Diamond sensors have a very fast signal response due to their low capacitance. The  
2104 electrical signal created by drifting charge carriers retains its shape without significant  
2105 distortion. When the sensor is used together with a fast current amplifier with a high  
2106 broadband limit ( $\sim 2$  GHz) and a readout device with a similar limit, the information  
2107 about the drifting charges is retained. For instance, a proton creates the free e-h pairs  
2108 along its trajectory. The electrons and holes start drifting immediately. Those closest  
2109 to the electrodes recombine quickly whereas those at the opposite side contribute to  
2110 the induced signal for longer. The resulting signal is therefore a triangular pulse  
2111 with a steep rising edge and a gentle falling edge. It is possible to determine the  
2112 drift velocity of the charge carriers by measuring the width of the pulse, as was done  
2113 in chapter 3. Furthermore, it is possible to determine with a certain probability  
2114 what is the type of incident radiation, judging by the shape of the induced pulse.  
2115 This, however, only applies to sCVD diamond material. Its uniform carbon lattice  
2116 allows the ionisation profiles to retain their shape, unlike in pCVD material, laden  
2117 with grain boundaries, or in even in silicon where the shape is deformed due to p-n  
2118 junction non-uniformities.

2119 This chapter describes an application that carries out particle identification by  
2120 means of the pulse shape analysis. It was developed for measuring activity of a  
2121 neutron reactor. In this case the device has to be able to filter out the photon  
2122 background with a rate several orders of magnitude higher than the neutron rate.  
2123 Overall detected rate in a neutron reactor can easily exceed  $10^8$  particles  $\text{cm}^{-2}\text{s}^{-1}$ ,  
2124 depending on the distance of the detector from the reactor core. The device has to  
2125 be able to cope with such high rates. It also needs to be dead time free or at least  
2126 close to that, to minimise the counting error. At these rates, it still has to be able to  
2127 identify the types of pulse. This type of online analysis cannot be done in software.  
2128 It has to be implemented in an FPGA.

## 5.1 MOTIVATION

---

### 5.1 Motivation

Pulse shape analysis (PSA) is a common software tool for analysing sensor response to incident particles. It is usually done by means of software that runs over big amounts of data that have been acquired and saved to storage. This offline analysis can be repeated and improved. However, the saved data take up a lot of storage space. In addition, saving raw waveform data requires a system capable of a high data throughput and fast data storing. For instance, an oscilloscope can save up to 100 signal waveforms per second. This means that there is a high measurement dead time. To avoid the high dead times, the software algorithms can be ported to the FPGA where they analyse the incoming signal in real time. The signal is then discarded and only the analysis results are saved, decreasing the storage space significantly.

The offline pulse shape analysis has already been used for particle identification with a diamond sensor [29, 24]. An effort has been made to implement an online and real time application for this analysis by porting the algorithms into an FPGA. This section first describes the device specifications Then it describes in detail the PSA algorithms and the structure of the code. Afterwards it discusses the performance results, which showcase the limitations of the device. Finally it describes the data acquired with radioactive sources and in neutron reactors.

### 5.2 Requirements

Chapter 3 shows that the shape is heavily dependent on several factors, such as environmental temperature and received irradiation dose. At temperatures lower than 150 K the signal from an  $\alpha$  starts deteriorating due to recombination of charges in the charge cloud. Sensor irradiation, on the other hand, introduces charge traps, which cause the signal to decay exponentially. These two factors are a significant limitation for particle identification. Priming can improve the charge collection and longterm stability of the pulse shapes. To improve the measurement further, a high bias voltage has to be applied, increasing the measurement SNR.

Factor	Operating range
Sensor material	sCVD diamond
Sensor thickness	500 $\mu\text{m}$
Temperature	150 K – 400 K
Radiation dose	$1 \times 10^{13} \text{ neq cm}^{-2}\text{s}^{-1}$
Charge carriers	holes
Bias voltage	$\sim 1 \text{ V } \mu\text{m}^{-1}$
Signal-to-noise	5

Table 5.1: Limitations to particle identification.

2159 **5.3 Device specifications**

2160 The ROSY box has a single BNC input with the termination  $50\ \Omega$  or  $1\ M\Omega$  with a  
2161 DC or AC coupling. The analog chain has a 250 MHz bandwidth limit. The input  
2162 range can be set from  $\pm 50\text{ mV}$  up to  $\pm 5\text{ V}$ . The signal offset can be set to any value  
2163 within this range. The ADC samples this signal with an 8-bit precision at a rate of  
2164 up to 5 GSPS. The PSA uses the highest sampling to achieve width measurement  
2165 resolution of 0.2 ns. The spectroscopic application does not need such a fine timing  
2166 resolution and therefore operates at a reduced sampling rate of 0.8 ns. The amplitude  
2167 resolution depends on the chosen input range, but at 256 ADC counts per sample, it  
2168 can be as low as  $0.39\text{ mV s}^{-1}$  at the range of  $\pm 50\text{ mV}$  and as high as  $39\text{ mV s}^{-1}$  at  
2169 the range of  $\pm 5\text{ V}$ .

2170 The logic structure of the PSA is designed using VHDL and runs on Xilinx Virtex 5. The PSA is capable of a maximum counting rate of  $1.56 \times 10^8$  pulses per second,  
2171 yielding a 6.4 ns double pulse resolution. The analysis is more time consuming; the  
2172 maximum throughput rate of the pulse shape analysis is  $\sim 5 \times 10^6$  pulses per sec-  
2173 ond. This means that after every pulse, the device has a dead time of approximately  
2174  $(200 \pm 15)$  ns, depending on the width of the pulse being analysed. Any pulse arriving  
2175 during the analysis of the previous one is counted, but not analysed. Any two pulses  
2176 with the distance between the rising edges lower than 6.4 ns are counted as a single  
2177 pulse.

2178 The device is very sensitive to noise pick-up. Therefore the setup must be designed  
2179 to minimise the pick-up by means of proper shielding, use of high-quality cables etc.  
2180 The relatively low bandwidth limit filters out some high-frequency noise, but not the  
2181 ringing or higher noise spikes. That is the task for the PSA.

2183 **5.4 Pulse parameters**

2184 A signal pulse on the input is parametrised during the analysis process. The PSA  
2185 measures its amplitude, area, width and the slope of its falling edge, as shown in  
2186 figure 5.1. The amplitude is the difference between the baseline and the highest  
2187 sample in the pulse and is given in ADC counts as an 8-bit value. The area is defined  
2188 as the sum of amplitudes of all samples between two defined boundaries within the  
2189 pulse. The width is defined as the number of samples with a value higher than a set  
2190 amplitude threshold. If the threshold is at half the maximum amplitude, the resulting  
2191 width is *full width at half maximum* (FWHM). The falling slope is the maximum  
2192 negative difference between values of two samples and is given in ADC counts per  
2193 sample. These parameters can also be used as *qualifiers* for accepting or discarding  
2194 a pulse. All four parameters limited by the low and high limit are called a *qualifier*  
2195 *set*. For instance, a rectangular pulse by an  $\alpha$  particle always has the same FWHM  
2196 and a very steep slope. In comparison, a photon has a lower falling slope value and  
2197 a narrower FWHM. Therefore the low and high cut on these two qualifiers allow for  
2198 a discrimination between the two pulses. Another qualifier is a *form factor* and is

## 5.5. APPLICATIONS

---

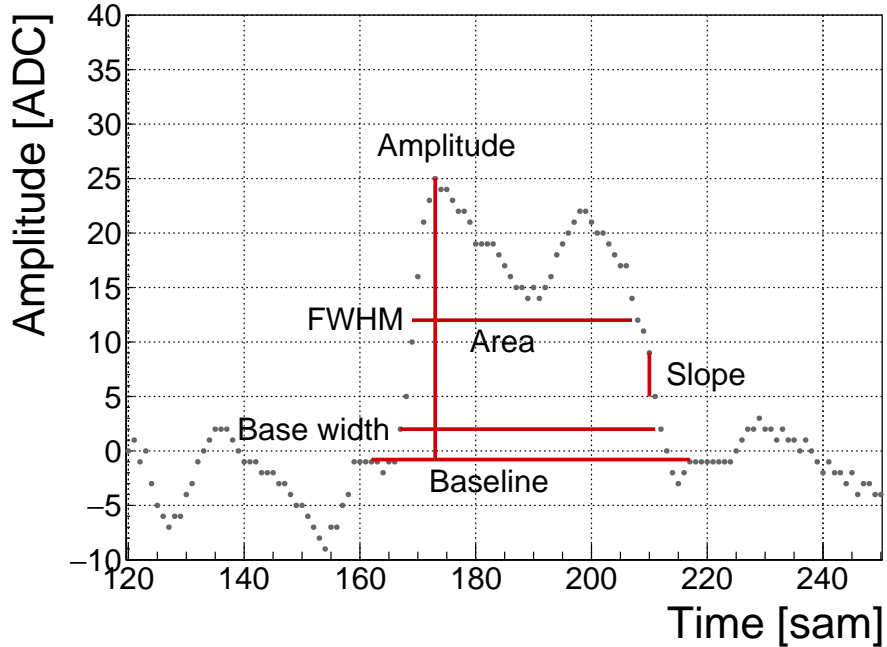


Figure 5.1: A pulse and its parameters.

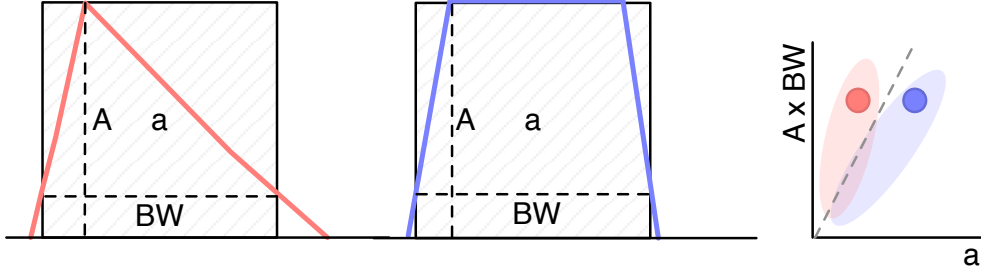


Figure 5.2: Form Factor is the ratio between the measured area ( $a$ ) and the calculated area ( $A \times BW$ ) of the pulse. The calculated area is significantly larger than the measured area for a triangular triangular pulse, but less so for the rectangular one. The red and blue dot in the right plot are the value entries of the two pulses shown. The red and blue oval shapes depict the regions for the values expected from triangular and rectangular pulses. By carefully choosing the linear qualifier (dashed line) and taking only the entries below the cut rectangular pulses can be identified.

2199 defined as the ratio between the measured area and the amplitude multiplied by the  
2200 width. By comparing the measured and the calculated area the difference between a  
2201 triangular and a rectangular pulse can be inferred, as shown in figure 5.2.

2202 **5.5 Applications**

2203 The FPGA firmware is designed for systems instrumented with CIVIDEC amplifiers  
2204 and CIVIDEC sVCD diamond detectors. Three applications are available: *Spectroscopy*,  
2205 *Pulse Shape Analysis* and *Counter*, each optimised for a specific task. Their  
2206 capabilities are described below. The firmware runs in ROSY, a readout system  
2207 produced by CIVIDEC.

2208 **Spectroscopy** is a tool for measuring energy spectra of radioactive sources. It is  
2209 used in combination with the CIVIDEC Cx spectroscopic charge amplifier. The  
2210 signal from the charge amplifier is analysed in real time. The FPGA measures the  
2211 maximum amplitude of the signal. The amplitude value is ready at the end of the  
2212 pulse and is stored in the amplitude histogram. Immediately after, the analysis is  
2213 reset and the system is ready for a new acquisition. Upon request from the software,  
2214 the histogram is read out, during which the analysis is paused. In addition to the  
2215 histogram building, the firmware can also store raw pulse waveforms, which can be  
2216 then read out by the software. The maximum allowed throughput is 1 million counts  
2217 per second.

2218 **Pulse Shape Analysis** is a tool for measuring energy spectra of radioactive sources,  
2219 with an additional feature. It can identify the type of radiation detected by the  
2220 diamond detector. By means of the pulse analysis it can subtract the background  
2221 radiation and only measure the signals from the defined radiation source. It is used  
2222 in combination with the CIVIDEC C2 fast current amplifier. The firmware receives  
2223 a current pulse from the detector and digitises it. The pulse is then analysed and  
2224 parametrised. The analysis module measures its maximum amplitude, full width  
2225 at half maximum (FWHM), baseline amplitude, falling slope and its area. Then  
2226 it compares the obtained pulse parameters with the qualifiers set by the software  
2227 and determines what type of radiation hit the diamond detector. Depending on the  
2228 qualifiers, the pulse can either be *accepted* or *rejected*. The firmware then stores the  
2229 parameters of the analysed pulse into histograms. Two histograms exist for each  
2230 parameter: one for all pulses and one for accepted pulses. In addition, there is one  
2231 2D histogram (a scatter plot), which can plot two parameters one with respect to the  
2232 other. Upon request from the software, all histograms are read out, during which the  
2233 analysis is paused. The maximum allowed throughput is 1 million counts per second.

2234 **Counter** is a tool that measures the count rate and the mean time during counts.  
2235 It is used in combination with the CIVIDEC Cx, C6 or C2 amplifier. It contains  
2236 one histogram which holds the information about the mean time during counts. The  
2237 counter is operational also during the readout of the histogram. The highest counting  
2238 rate with enabled histogram writing is  $3 \times 10^7 \text{ s}^{-1}$ .

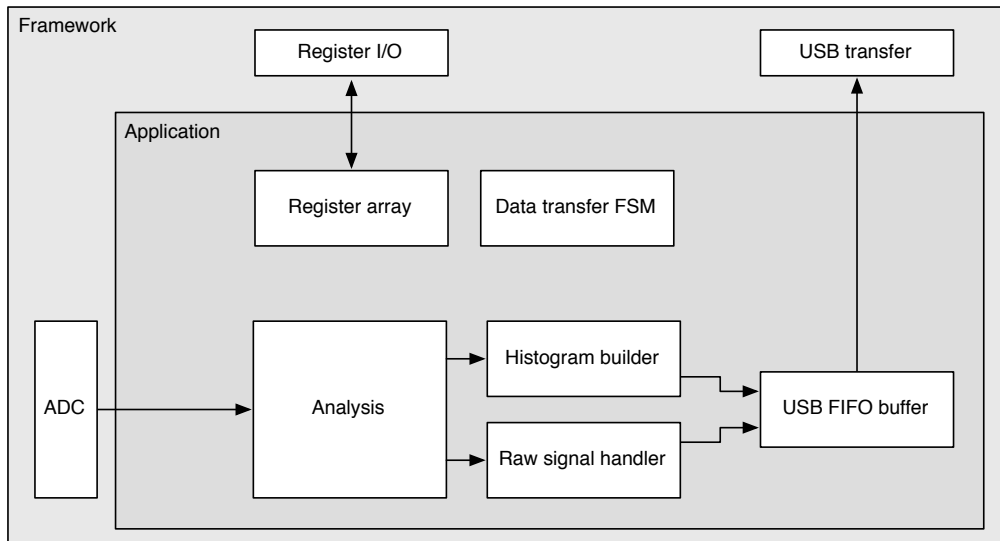


Figure 5.3: Firmware design structure.

## 5.6 Description of the firmware

The applications are built on top of the Picotech platform. The base code handles the communication between the software and the hardware. Furthermore, it provides the interface to the ADC data, the input/output registers and the USB data transfer. The applications have a set of modules that handle the data input and output and a module for signal analysis, as shown in figure 5.3. The data handling modules are very similar in all the applications to ensure compatibility of the communication between software and firmware and the readout data format. The analysis module, however, is different from one application to the other. The data handling layer is the same for all applications and consists of the final state machine (FSM), the histogram builder, the raw signal handler, the USB FIFO buffer and the register array.

The firmware is written entirely in VHDL. The diagram in figure 5.3 shows the module architecture. The ADC provides the module with 32 digitised signal samples every clock cycle (6.4 ns). The signal is routed directly to the pulse analyser and into the raw signal handler. The analyser outputs are connected to the I/O registers and to histogram buffers. Both the histogram buffers and raw signal buffers are connected to the USB FIFO through a multiplexor. The firmware communication to the controller is done via input/output (I/O) registers (control and status registers, counters) and serially via USB (histogram data, waveforms).

### 5.6.1 Design constraints

**Speed** The ADC provides 32 8-bit samples on every 6.4 ns clock cycle. It is not possible to e.g. sum all 32 values in a single cycle, because the summation takes too long to complete. This is why the summation has to be pipelined and carried out

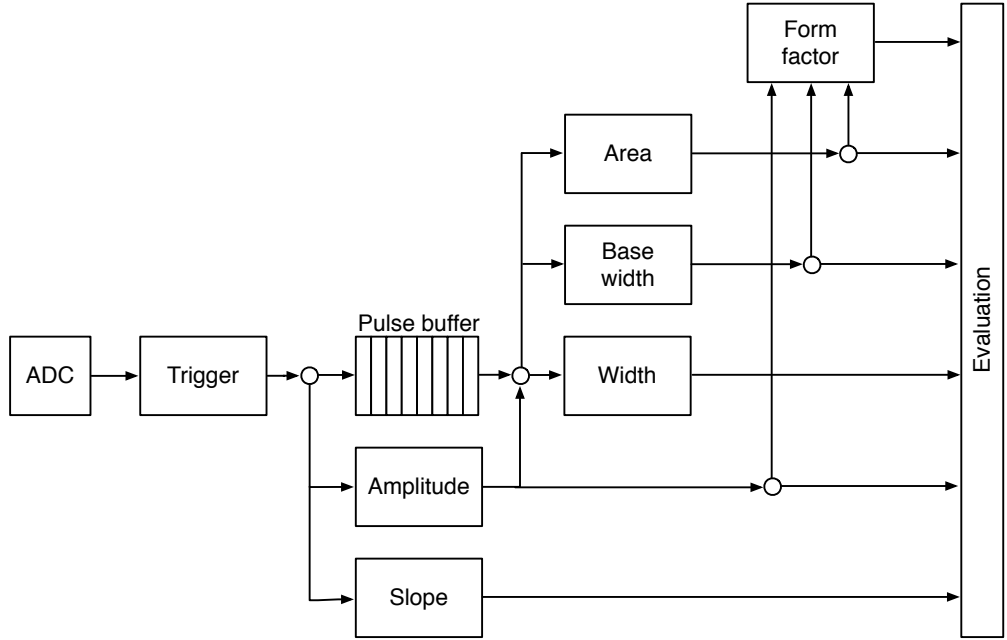


Figure 5.4: Code design plan.

in three cycles. This adds up to the analysis duration, which in turn decreases the maximum pulse rate.

**Firmware size** The PSA application makes use of a number of FIFO and RAM buffers to store the pulse waveforms and histograms. 48 32k block RAM modules have been used for the implementation, maxing out the available block RAM memory space on this FPGA. The analysis algorithm also takes up a significant portion of the FPGA. Many of the operations are carried out on 256-bit long numbers received from the ADC, which quickly fills up the available logic. This is also why the place and route procedure takes a long time.

**Power consumption** The reduction of the power consumption is not crucial for the intended applications.

## 5.6.2 Analysis module

This module is different for different applications. The Pulse Shape Analysis (PSA) application has the most complex module design. The spectroscopy application only uses a small part of that design and the Counter application an even smaller one.

The analysis (or parametrisation) is carried out in several steps, as shown in figure 5.4. The triggering block starts the readout upon signal threshold crossing. The maximum slope of the falling edge is observed. The Amplitude block calculates the pulse height and retains the maximum amplitude while pushing the signal into the pulse buffer. Then the entire pulse is clocked out of the buffer while its FWHM,

## 5.6. DESCRIPTION OF THE FIRMWARE

---

2282 baseline width and area are measured. Finally, the Form factor is calculated. At the  
2283 end the Evaluation block takes in all the parametrised information and classifies the  
2284 pulse according to user-defined cuts.

2285 **Triggering** module handles signal polarity swapping, triggering on threshold and  
2286 defining the trigger window. The real-time processing algorithm allows for a positive  
2287 or an inverted input signal. However, the PSA only handles positive-polarity pulses.  
2288 Therefore a negative signal is swapped in the *triggering* block. Signal analysis and  
2289 readout are then triggered when the signal crosses a user-defined threshold. In addition,  
2290 the signal has to be over the threshold for a defined number of samples. This is  
2291 to avoid triggering on noise spikes. A double clock cycle delay is used on the signal  
2292 to make sure that the recorded signal window includes the rising edge of the pulse as  
2293 well as some baseline before it. A *trigger active* signal marks a window that contains  
2294 the entire pulse including some baseline signal before and after it. The trigger can  
2295 be vetoed by three signals: if the pulse analysis is still taking place, if the input  
2296 signal exceeds the maximum voltage range or if the data transfer FSM is pausing the  
2297 analysis due to data transfer to the controller.

2298 **Amplitude** block calculates the pulse height from the difference between the pulse  
2299 and the baseline. It also finds the position of the maximum amplitude within the  
2300 clock cycle. It receives 32 8-bit samples from the triggering block every clock cycle.  
2301 Time delays in the logic prevent it to find the maximum value of the 32 samples  
2302 within one clock cycle (6.4 ns). Therefore the decision logic has been pipelined in  
2303 three stages, which means that the final maximum value is ready three clock cycles  
2304 after the end of the pulse.

2305 **Pulse buffer** is a FIFO that stores the signal while its amplitude is being measured.  
2306 At the end of the pulse the FIFO is read out so that the remaining measurements  
2307 can take place.

2308 **Width** block uses the maximum amplitude to determine the *half-maximum* and to  
2309 measure the FWHM. To do so, it counts the samples that are above the half-maximum  
2310 amplitude. However, this method might also count high enough noise spikes before  
2311 or after the pulse. Hence an improved method, which “cleans” the measurement of  
2312 unintentional additional noise, has been implemented. It is described in section 5.6.3.

2313 **Baseline width** block is the same as the Width block, but it measures the width  
2314 either at 50 %, 25 %, 12.5 % or 6.25 %, depending on the setting in the register. It  
2315 also makes use of the special method described in 5.6.3 to avoid overestimations due  
2316 to including noise in the measurement.

2317 **Area** block measures the pulse area by summing up the amplitude values of the sam-  
2318 ples in the pulse. The boundaries of the summation are defined with the crossing of  
2319 the amplitude above a certain threshold. Only the samples between those boundaries  
2320 are summed up. The boundaries can be set at 50 %, 25 %, 12.5 % or 6.25 % of

2321 the maximum amplitude of the pulse. The area measurement makes use of the same  
2322 routine as the FWHM and Baseline width block to remove the potential outlying  
2323 samples.

2324 **Falling slope** block measures the highest negative difference between amplitudes of  
2325 two adjacent samples, thus getting the maximum negative slope of the pulse. It is an  
2326 experimental routine, only used for academic purposes.

2327 **Form factor** block is used as a special qualifier for particle identification. It com-  
2328 pares the weighted measured area of the pulse with its weighted calculated “form”,  
2329 which is defined as the multiplication of the measured amplitude and baseline width.  
2330 The equation is as follows:

$$x \cdot a - y \cdot A \cdot BW \geq 0, \quad (5.1)$$

2331 where  $a$  is the measured area,  $A$  is the amplitude,  $BW$  is the baseline width and  $x$   
2332 and  $y$  the weighting factors for the measured and calculated area, respectively. The  
2333 output of the block is the boolean result of this equation.

2334 **Evaluation** block takes in all the parameters from the analysis blocks and compares  
2335 them against the user-defined qualifiers. If the parameters are within the bounds,  
2336 the pulse is accepted, otherwise it is rejected. The corresponding counters within the  
2337 block are incremented.

### 2338 5.6.3 Area and width measurement

2339 The routine for measuring pulse area and width must have a specific algorithm imple-  
2340 mented to carry out the measurements correctly. The core point is that the routine  
2341 precisely defines the edges of a pulse. It does so by means of *vector cleaning*, pre-  
2342 sented in figure 5.5. An important input, beside the ADC data and the measurement  
2343 threshold, is the position of the sample with the highest amplitude.

2344 The signal arrives from the ADC as a set of 32 8-bit samples every every clock cycle  
2345 with a period of 6.4 ns. All 32 samples are compared against the width measurement  
2346 threshold. If a sample value is equal or higher than this threshold, a binary 1 is set  
2347 in a 32-bit *vector* on the position corresponding to the position of the sample in the  
2348 incoming ADC data set. The resulting vector might also include some noise at the  
2349 edges of the pulse, depending on the height of the width measurement threshold. The  
2350 old routine simply counts the binary ones in this vector to get the pulse width. This  
2351 works well for measuring the FWHM because the threshold was high. However, for  
2352 width measurements at 25 %, 12.5 % or 6.25 % of the pulse height this might already  
2353 become a problem, because the noise might be counted in as well. This is why the  
2354 new routine cleans the outliers in this vector before counting the remaining ones in  
2355 the clean vector.

2356 The routine starts from the position of the maximum height. It follows the vector  
2357 in both ways and finds the first falling edge (0 at this position and 1 at the previous

## 5.6. DESCRIPTION OF THE FIRMWARE

---

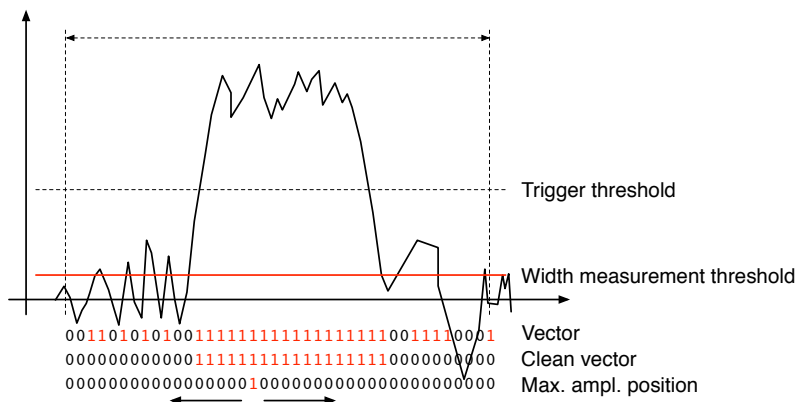


Figure 5.5: A sample pulse. The first vector shows which samples are above the width measurement height. The second vector is a clean vector. The third line shows the position of the maximum amplitude. The vector cleaning algorithm starts from the maximum amplitude and continues in both ways along the vector.

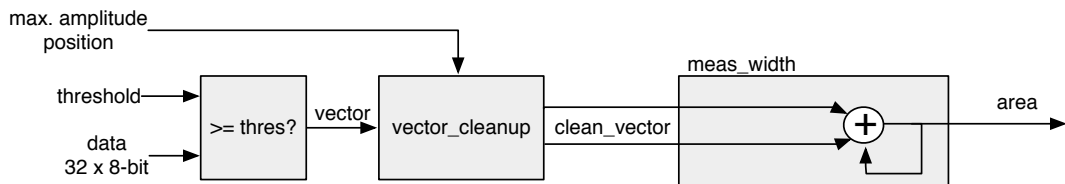


Figure 5.6: This block counts the remaining binary ones in the clean vectors and outputs this value as the pulse width.

2358 one). From there on it rewrites any binary 1 with a binary 0. The resulting clean  
 2359 vector only has one bunched set of binary ones which are summed, yielding a precise  
 2360 pulse width. The area measurement is similar - it only integrates over the samples  
 2361 marked in the clean vector. Both measurement routines, for area and for width,  
 2362 are implemented separately so that the area routine can have a different threshold set.

2363 This section explains how the algorithm is designed. First, the idea for it was  
 2364 tested using Excel and was only afterwards ported to the VHDL. The underlying  
 2365 algorithm first cleans the vector. Then it passes the cleaned vector either to the  
 2366 width or area measurement, as shown in figures ?? and ???. The width measurement  
 2367 module only sums the ones in the vector whereas the area measurement module sums  
 2368 the data samples marked by the cleaned vector. Both modules issue a *valid* signal  
 2369 when they finish the measurement.

### 2370 5.6.3.1 Vector cleaning

2371 This is the most important block. Its inputs are: *vector*, *parsing active*, *position of the*  
 2372 *max. amplitude (PA)* and its delay (*DA*). *PA* is a 32-bit binary number that shows the  
 2373 position of the sample with the maximum amplitude within the data block whereas

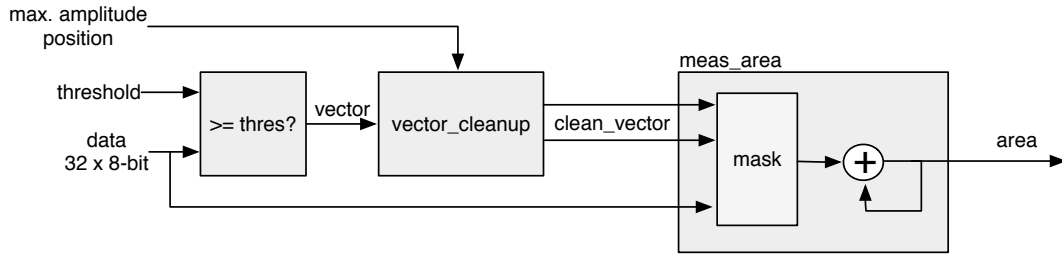


Figure 5.7: This block masks the input data with the clean vector and sums the remaining samples.

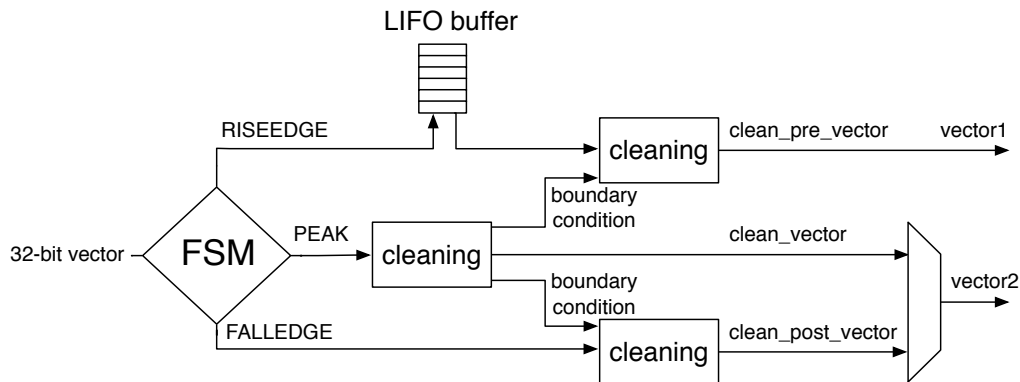


Figure 5.8: Vector cleaning routine outputs two vectors - one forward in time and one back in time from the peak of the pulse.

2374 the DA tells us how many clock cycles after the start of the parsing this PA block  
 2375 is. The vector cleaning module is designed as a final state machine (FSM) with the  
 2376 states IDLE, RISEEDGE, PEAK, FALLEDGE and READY. The FSM is idle until it  
 2377 receives the *active* signal from the external module, marking that the vector parsing  
 2378 has commenced. It switches to RISEEDGE, which starts two procedures: 1) it fills  
 2379 the vector of the pulse's rising edge into a last-in-first-out (LIFO) buffer and 2) counts  
 2380 down from the DA value. When this counter reaches 0, the FSM changes its state to  
 2381 PEAK because the current vector on the input is the one containing the maximum  
 2382 amplitude. This data block is sent through the *peak algorithm*, which cleans the  
 2383 vector. The FSM switches to FALLEDGE state. Now both the previously buffered  
 2384 vector of the rising edge and current vector of the falling edge go through the *pre-*  
 2385 *and post- algorithm* where they are cleaned, but they get their boundary conditions  
 2386 from the *peak algorithm*. The output of this module is therefore two cleaned vectors  
 2387 in parallel – one forward in time and the other backwards.

### 2388 5.6.3.2 Algorithm

2389 The underlying algorithm is sequential - it carries out a logic operation on vector bit  
 2390 on position 0, uses the output of this operation for the operation on bit on position

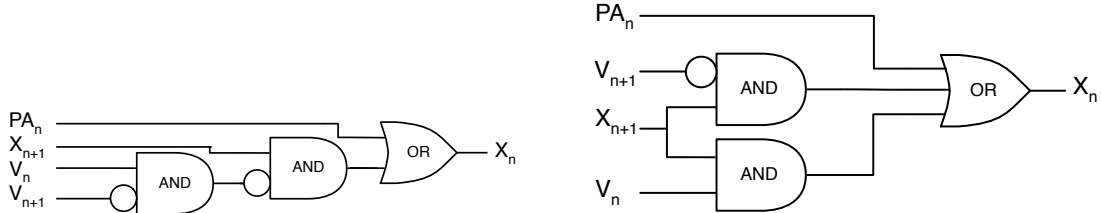


Figure 5.9: One logic step in the algorithm chain before and after Karnaugh minimisation.

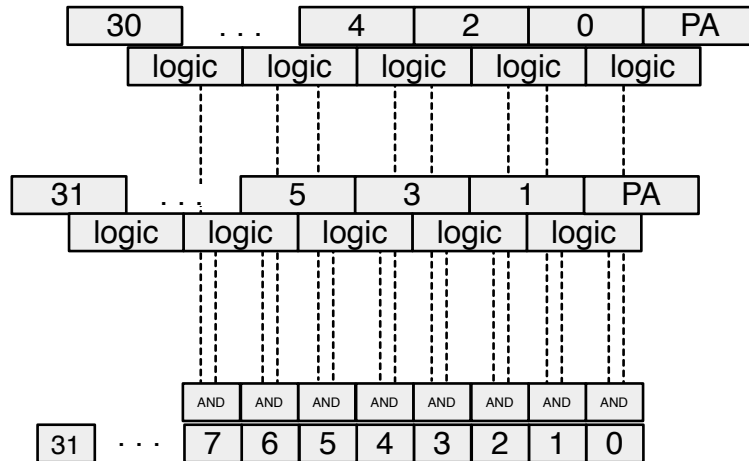


Figure 5.10: Vector is divided into two 16-bit logic chains. The algorithm logic is then run on the two chains separately. The results are then merged into one 32-bit clean vector by using a set of AND gates.

2391 1 and so on. This means that it has to carry out 32 logic operations per clock  
 2392 cycle. With each operation taking approximately 0.3 ns, the entire logic chain takes  
 2393 approximately 10 ns to complete. With only 6.4 ns per clock cycle, this means timing  
 2394 errors would occur. To fix the problem, a more complicated *decimated algorithm* has  
 2395 been designed. It consists of two parallel logic chains. Each of the two only takes  
 2396 every second bit into account (chain one: 0, 2, 4 ..., 30. Chain two: 1, 3, 5 ..., 31).  
 2397 This makes the chains effectively 16 bits long. The algorithm is run on the two chains  
 2398 and the results are merged together at the end as shown in figure 5.10. This effectively  
 2399 reduces the number of sequential logic operations to around 18, which is within the  
 2400 timing constraints.

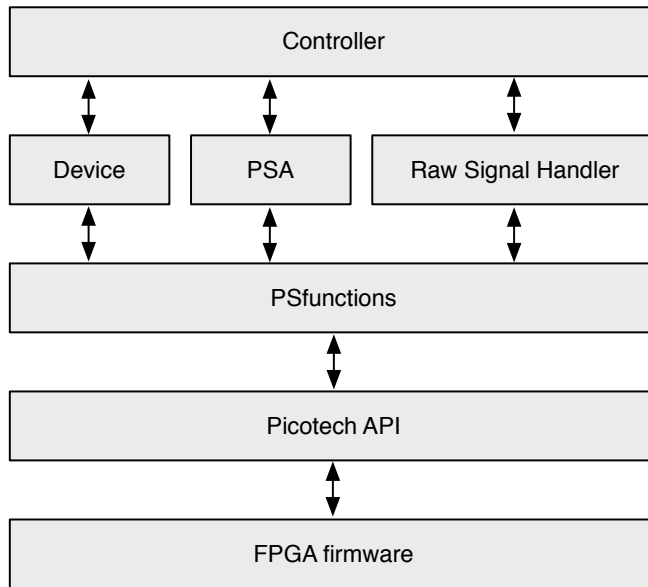


Figure 5.11: Abstraction levels of the controller software.

## <sup>2401</sup> 5.7 Control and data interface

<sup>2402</sup> Communication between the device and the controller PC is done via the API func-  
<sup>2403</sup> tions provided by the producer. In addition, the API used by CIVIDEC has access  
<sup>2404</sup> to several extra functions. These allow the user to download a customised bitfile to  
<sup>2405</sup> the FPGA, access the I/O registers and use the USB data transfer.

### <sup>2406</sup> 5.7.1 Software

<sup>2407</sup> The software has been designed in C++ in several levels of abstraction. Figure 5.11  
<sup>2408</sup> shows the structure of the classes. The classes Device, PSA and RawSignalHandler  
<sup>2409</sup> are there to make it easier to read and understand the controller code. In principle the  
<sup>2410</sup> PSfunctions can also be accessed directly by the controller, but for this the instruction  
<sup>2411</sup> sequences must be well known and understood.

### <sup>2412</sup> 5.7.2 Data readout

<sup>2413</sup> The device records the data in two forms - as signal waveforms and as histograms  
<sup>2414</sup> of analysed pulse parameters. Both are available upon request from the controller.  
<sup>2415</sup> Only one of the two can be transferred via the USB line at a time.

<sup>2416</sup> The waveforms are saved into a FIFO buffer, which can hold up to 64 pulses of the  
<sup>2417</sup> length of  $\sim$ 500 samples. The data format for each pulse is such that it starts with a  
<sup>2418</sup> header containing the pulse timestamp and the sequential number, continues with the  
<sup>2419</sup> data samples and ends with a header containing all the measured parameters (width,

## 5.8. PERFORMANCE RESULTS

---

2420 amplitude, area, falling slope and form factor). When the FIFO is full, it issues a  
2421 flag, which tells the controller that the data buffer is ready for readout.

2422 The histograms are implemented into the FPGA's Block RAM. Their size ranges  
2423 from 256 to 4096 bins (an 8-bit or a 12-bit histogram, respectively), depending on the  
2424 required histogram resolution. For instance, the width parameter is measured with a  
2425 0.2 ns resolution; the expected maximum pulse width is less than 20 ns. This yields  
2426 the maximum range of 100 bins, making an 8-bit histogram sufficiently large. The  
2427 same reasoning is applied to the amplitude measurement. In this case the maximum  
2428 range is defined by the 8-bit resolution of the ADC. The area measurement, however,  
2429 yields higher values and can therefore have a more refined binning (12-bit). Finally,  
2430 a single 12-bit 2D histogram is included, with 6 bits for every axis. It is used as an  
2431 online scatter plot for comparing one measured parameter to another. An example  
2432 for it is a comparison of the width against the area, which can help the user determine  
2433 the cuts that need to be applied to the measurement.

## 2434 5.8 Performance results

2435 The device has been tested in the lab using a pulse generator as well as several radioactive  
2436 sources. The results show that: 1) the amplitude, area and width measurement  
2437 are linear across all input ranges, 2) the highest rate of the PSA algorithm is  $\sim 5 \times 10^6$   
2438 pulses per second and 3) the lowest SNR where the algorithm still functions is  $\sim 5$ .

2439 **Trigger rate** A pulse generator was used to verify the highest achievable rate at  
2440 which the PSA still analyses every incoming pulse. The final state machine imple-  
2441 mented in the pulse analysis module prevents the triggering block from issuing a  
2442 trigger due to an incoming pulse if the previous analysis is still in ongoing. Given  
2443 that all the pulses were of the same length, the analysis duration was always the  
2444 same. When the time between the incoming pulses was shorter than the time of the  
2445 analysis, the pulses were not analysed. Figure 5.12 shows the sharp decline in the  
2446 percentage of the analysed pulses when reaching the rate of 5 MHz. Therefore the  
2447 overall analysis duration for a 10 ns pulse is approximately 200 ns.

2448 **Linearity** A pulse generator was used to verify the linearity of the measurements  
2449 across all input ranges. Pulse width and amplitude were varied and measured both  
2450 with the oscilloscope and the PSA to check for non-linearities or inconsistencies in the  
2451 PSA measurements. The resulting plots in figures ?? and 5.13c show that the PSA  
2452 measurements agree well with those from the oscilloscope. The major inconsistency  
2453 is observed in the lower range of the plots. It stems from the fact that the bandwidth  
2454 limit of the PSA is lower than that of the oscilloscope, which affects the pulse shape.  
2455 Effectively, the PSA cannot measure the rectangular pulses of the width smaller than  
2456 2 ns.

2457 **Stability** The input pulse signal was superimposed with white noise generated by  
2458 a noise generator with a variable gain. The mixed signal yielded pulses with an

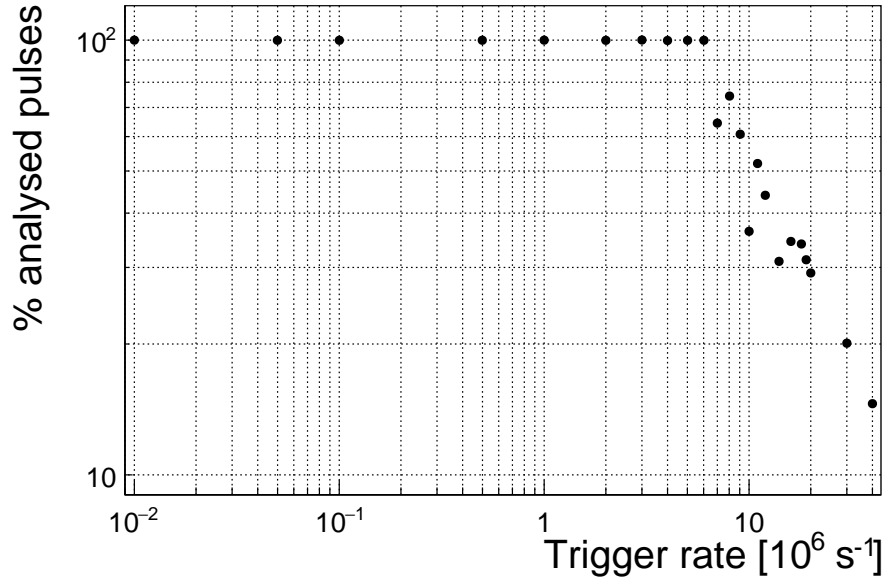


Figure 5.12: This figure shows the capability of the device to analyse all arriving pulses for a range of input frequencies. The highest achievable rate with zero lost pulses is  $5 \times 10^6 \text{ s}^{-1}$ .

SNR ranging from 5 (very noisy) to 100 (noise negligible). The PSA then performed the pulse parametrisation at different SNRs. The resulting plots in figures 5.13b, 5.13d and 5.13e show that the pulse width measurement is stable even for low SNR whereas the amplitude measurement is affected significantly. This stems from the analysis taking the highest sample as the pulse's amplitude. The area measurement, being effectively the integrated amplitude across the pulse, is also affected by the faulty amplitude measurement. Nevertheless, the mean area remained the same. This means that the added noise only affects the resolution of the spectrum, not its position.

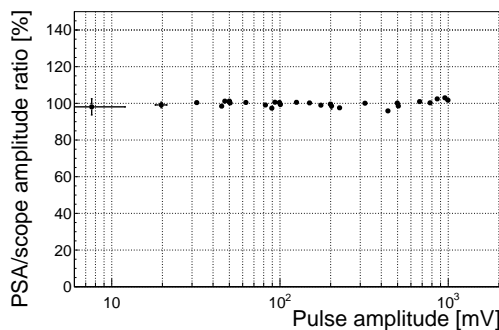
### 5.8.1 Comparison between the charge- and current-sensitive spectroscopy

The calibration was done using a  $^{148}\text{Gd}^{239}\text{Pu}^{241}\text{Am}^{244}\text{Cm}$  source which emits  $\alpha$  particles with four different energies. The PSA in combination with the current amplifier was compared against the 8-bit spectroscopic application in combination with the charge amplifier and a commercial 14-bit spectroscopic readout.

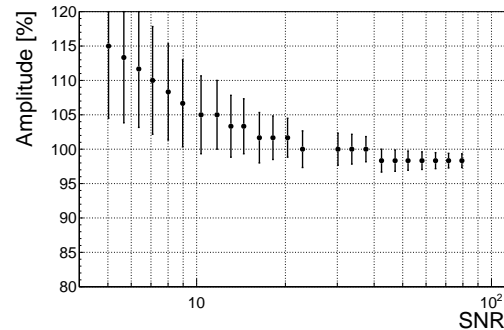
The  $^{241}\text{Am}$  peak measured by the Cx amplifier has an RMS of 0.8 ADC, which corresponds to a 32 keV energy resolution. For comparison, the C2 amplifier measures this peak with an RMS of 1.9 ADC, which corresponds to a 75 keV energy resolution. Therefore the energy spectrum measured by the current amplifier has a lower energy resolution.

## 5.8. PERFORMANCE RESULTS

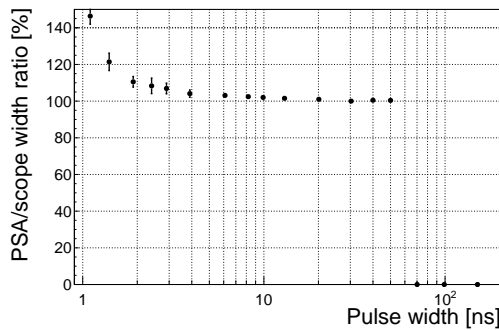
---



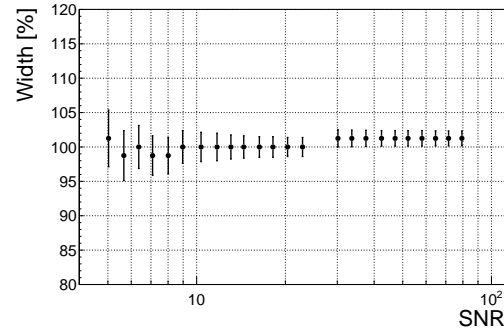
(a) Linearity across the amplitude range.



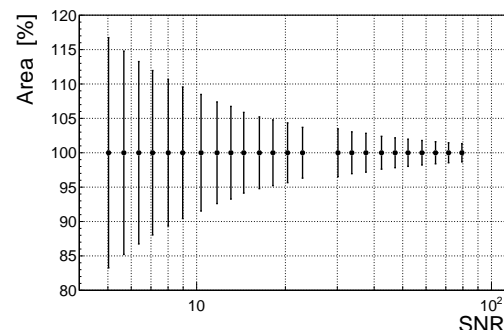
(b) Amplitude stability.



(c) Linearity across the width range.



(d) Width stability.



(e) Area stability.

Figure 5.13: These diagrams show the linearity of the measurements and their stability with respect to analog noise.

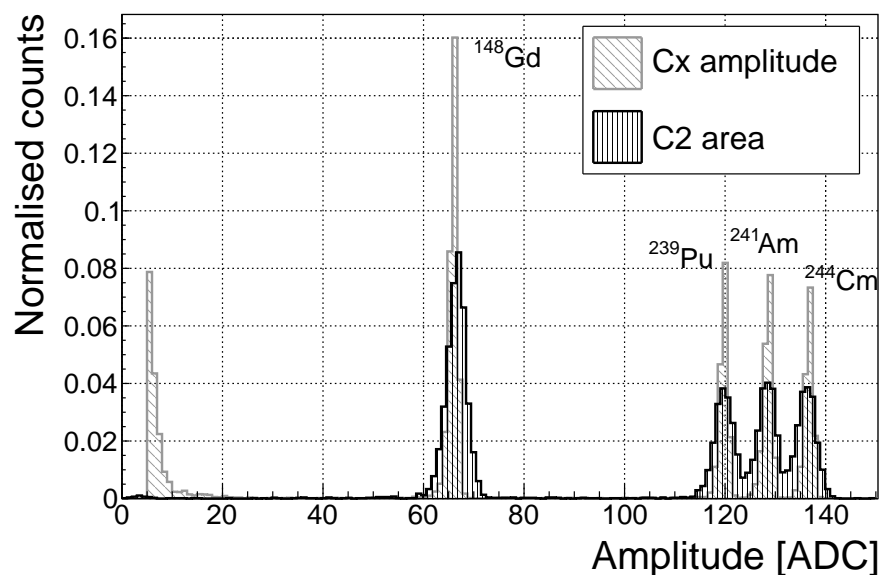


Figure 5.14: Spectrum of a  $^{148}\text{Gd}^{239}\text{Pu}^{241}\text{Am}^{244}\text{Cm}$  source using a Cx and a C2 amplifier.

## 5.9. SOURCE CALIBRATION

---

### 2479 5.9 Source calibration

2480 The operation of the pulse shape analysis has been tested using several radioactive  
 2481 sources. In particular, an  $\alpha$ , a  $\beta$  and a  $\gamma$  source have been used. Each source has  
 2482 been placed on top of the diamond detector and left for a predefined time depending  
 2483 on its activity. Table 5.2 shows the sources used, the time of exposure and their rate  
 2484 during this time. The data for the  $\alpha$  source have been taken for both polarities. In  
 2485 addition, a long run with an  $\alpha$  source with a sheet of paper in between the source  
 2486 and the diamond has been taken. The paper stops the  $\alpha$  particles but lets through  
 2487 the photons, which helps to estimate the background photon radiation of the source.

Run	Source	Radiation	Energy [MeV]	Time [h]	Triggers	Rate [ $s^{-1}$ ]	Bias [V]
2488	1 $^{241}\text{Am}^*$	$\alpha$	5.5	60	958	4.4e-3	500
	2 $^{241}\text{Am}$	$\alpha$	5.5	17	10558	0.17	500
	3 $^{241}\text{Am}$	$\alpha$	5.5	18	11454	0.18	-500
	4 $^{90}\text{Sr}$	$\beta$	2.3	0.42	1.07e6	1000	500
	5 $^{60}\text{Co}$	$\gamma$	1.3	0.28	1.34e6	3300	500
	6 $^{239}\text{Pu Be}$	$n$	1-10	2.5	1.5e6	230	500

2489 Table 5.2: Measurements carried out at Atominsttitut.

2490 The pulses acquired during the data taking are shown in persistence plots in  
 2491 figures 5.15. Figure 5.15a showing the  $^{241}\text{Am}$  source background reveals that the  
 2492 diamond detector had been contaminated, probably with chipped-off grains of the  
 2493 unsealed source. This stems from the fact that  $\alpha$  pulses are recorded despite having  
 2494 a sheet of paper, which stops all the particles emitted by the source. However, the  
 2495 number of  $\alpha$  hits due to contamination is negligible - an estimated  $1 \text{ h}^{-1}$ . Another  
 2496 point worth noting is the falling slope of the rectangular pulse in figure 5.15c. This  
 2497 stems from the space charge that had built up during the neutron irradiation and is  
 2498 discussed in section ???. Finally, figure 5.15f shows that the neutron source causes  
 2499 the widest variety of pulse shapes - triangular and rectangular as well as those in  
 2500 between. Pulse shapes caused by neutrons are described in detail in [44, 43].

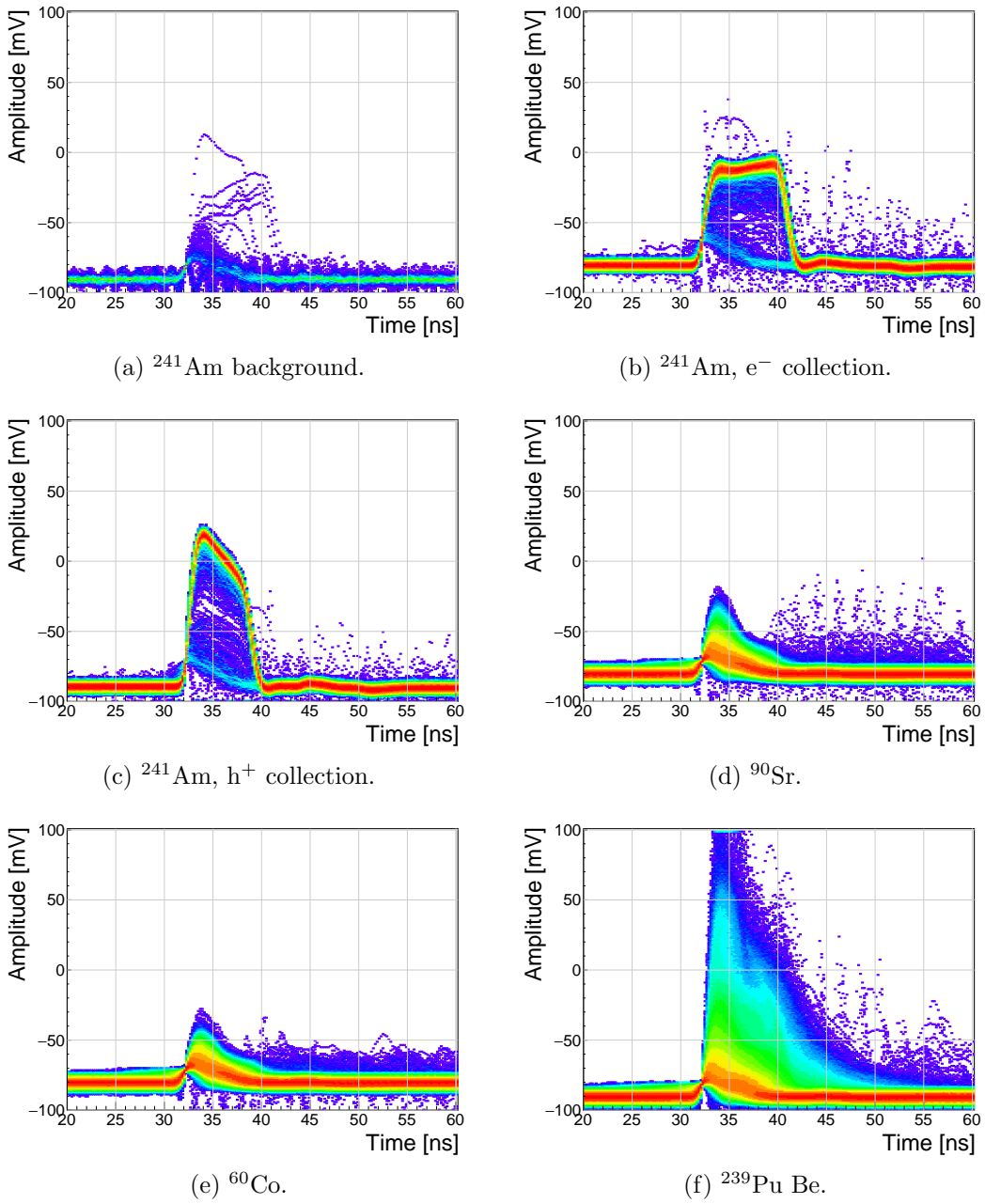


Figure 5.15: Accumulated pulses for all runs.

## 5.9. SOURCE CALIBRATION

---

### 5.9.1 Source measurements – scatter plots

An online pulse shape analysis has been run on all the above mentioned data sets. The parameters of the pulses are plotted in 2D histograms - in form of scatter plots. The aim is to find a way to distinguish between the various types of radiation in order to only select the spectrum of a single type of particles from a spectrum of a mixed source. The energy spectrum is directly proportional to the measured area of the current pulses, therefore all the parameters are plotted against the pulse area. The parameters used are:

- FWHM
- Base width
- Amplitude
- Amplitude × Base width
- Base width – FWHM
- Falling slope

Every individual parameter can be attributed a set of qualifiers with which a certain part of the distribution can be rejected. There are two ways to apply the qualifiers. One is to set the minimum and maximum value for a specific parameter. The accepted pulses are those in between these two values. The minimum and the maximum qualifier are marked with a blue and a red line in the subsequent scatter plots. The second way is to apply a linear cut to the distribution in the scatter plot. The user can choose the slope of the line and to accept either the pulses above or below the line. The colour of the line is blue if the part above the line is accepted and red if opposite. Currently two scatter plots have this option implemented: area vs amplitude and area vs amplitude×base width. The latter represents the Form Factor, which is discussed in section 5.6.2.

The sets of plots in figures 5.16, 5.17, 5.19 and 5.20 show the above listed parameters plotted against the pulse area for  $^{241}\text{Am}$  background, electrons and holes,  $^{90}\text{Sr}$  and  $^{64}\text{Co}$  source, respectively. Any distinguishable difference between the plots of two sources would suggest that that particular parameter can be used to distinguish one type radiation from the other. For the most part the photons are considered the rejected pulses (greyscale colour palette) whereas  $\alpha$  particles or neutrons are accepted (yellow colour palette). In special cases only a certain types of neutron interactions are accepted, as depicted in section 5.10.

#### 5.9.1.1 $^{241}\text{Am}$ source

The source emits  $\alpha$  particles at  $\sim 5.5$  MeV and photons with a range of energies. Due to the losses in the air and the electrode the measured  $\alpha$  energy varies – between  $\sim 5$  MeV down to 1 MeV.

Figures 5.16 and 5.17 show the pulse area distribution with respect to the aforementioned parameters, for electrons and holes respectively. Focusing on the top left plot in figure 5.16, a distinctive horizontal stripe appears at a width of 9 ns, ranging from 100 up to 630 pVs. This is the aforementioned spread of  $\alpha$  energies. The shape of the pulse from this type of radiation retains the width even at smaller energies. Only its amplitude is decreased. This is because the free charge carriers in the diamond are traveling with the same speed in all cases, inducing rectangular pulses of the same widths.

The other cluster in the [area, FWHM] phase space comes from the background photons. The two clusters are far apart from one another with no overlap. It is therefore straightforward to define a cut in the FWHM to distinguish between the  $\alpha$  and  $\gamma$  entries. This is done by means of the minimum and maximum FWHM constant qualifier, which marked red and blue in the [area, FWHM] subfigure.

The [area, amplitude] subfigure also reveals two distinguishable clusters, which can be segregated using a linear qualifier. The angle of the  $\alpha$  stripes in the [area, amplitude] subplots is significantly smaller than that of the photon stripe. The separation is much less pronounced in the other subfigures.

There is a third barely distinguishable island visible in the top two plots, both area and width values close to zero. This island is formed by noise, which triggered the analysis.

The situation is similar when inverting the bias voltage and collecting holes, as shown in figure 5.17. Here, however, the two clusters are much closer together even in the [area, FWHM] subfigure. This makes it more difficult to define a clear border between the two. The other five qualifiers are in this case less important than the FWHM. Nevertheless, it can be deduced from the plots that the difference BW-FWHM must be below 4 ns.

The slope is dependent of the amplitude, which can be seen in the bottom right plot, making it an unreliable qualifier in the lower area range. The amplitude, scaling with area, makes a distinguishable straight line in the middle left subfigure.

The amplitude increase with area in the [area, amplitude] subfigure is similar for photons and  $\alpha$  particles. Therefore a linear qualifier can not be used to distinguish  $\alpha$  radiation from  $\gamma$  radiation when measuring holes.

Figures 5.18a and 5.18b show a one-dimensional area distribution of the acquired data for electron and hole collection. The blue histogram represents all collected data whereas the red one marks the data whereby the pulse parameters are within the qualifiers. In both figures the  $\alpha$  peak at 600 pVs is clearly visible, followed by a  $\gamma$  quasi-Landau distribution with an MPV of  $\sim$ 70 pVs and a noise peak at the very left of the area distribution. These two contributions have been rejected by the FWHM qualifier.

## 5.9. SOURCE CALIBRATION

---

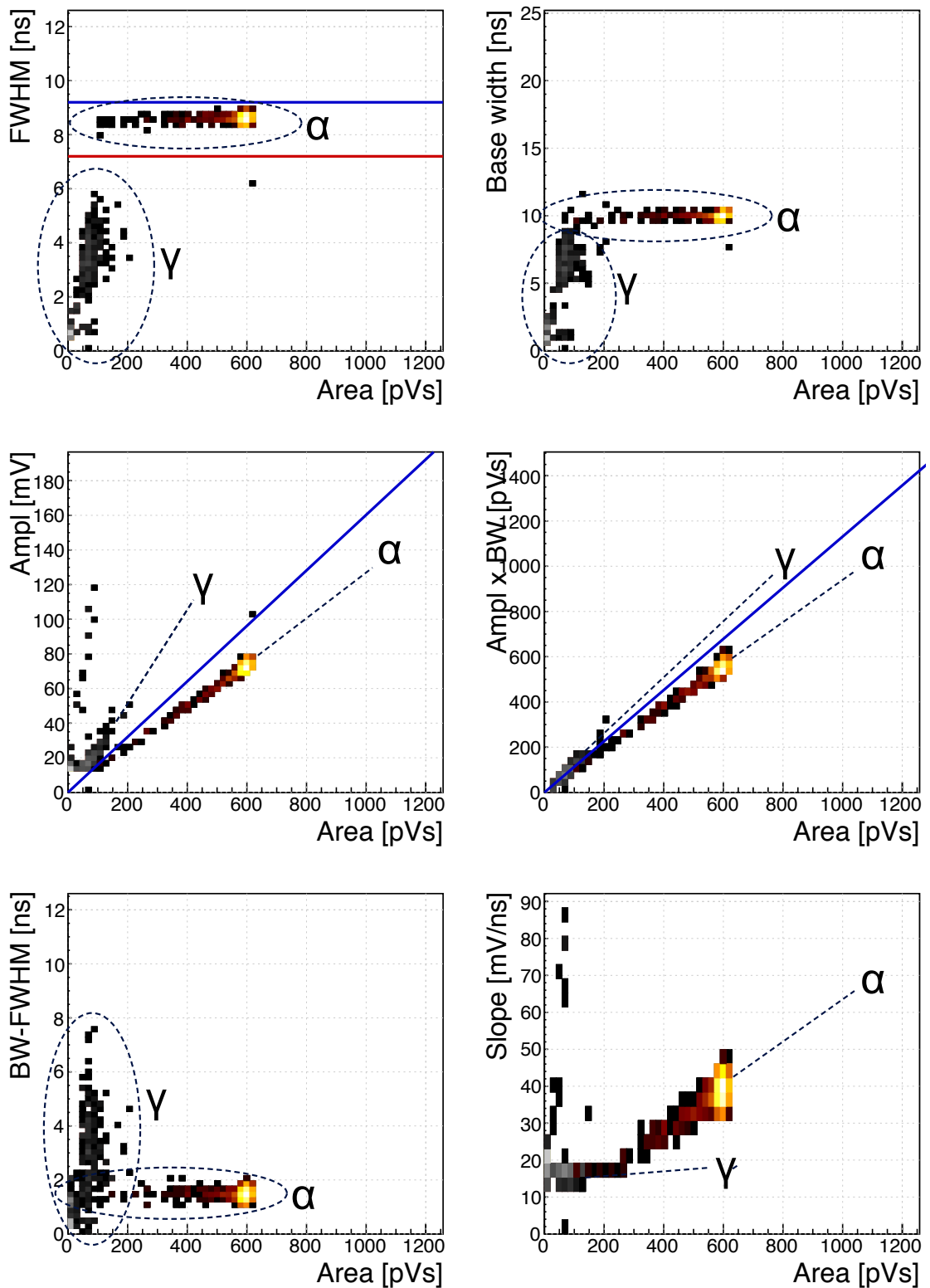


Figure 5.16:  $^{241}\text{Am}$ ,  $e^-$  collection. Qualifier: FWHM. Optional qualifiers: Amplitude, Form Factor.

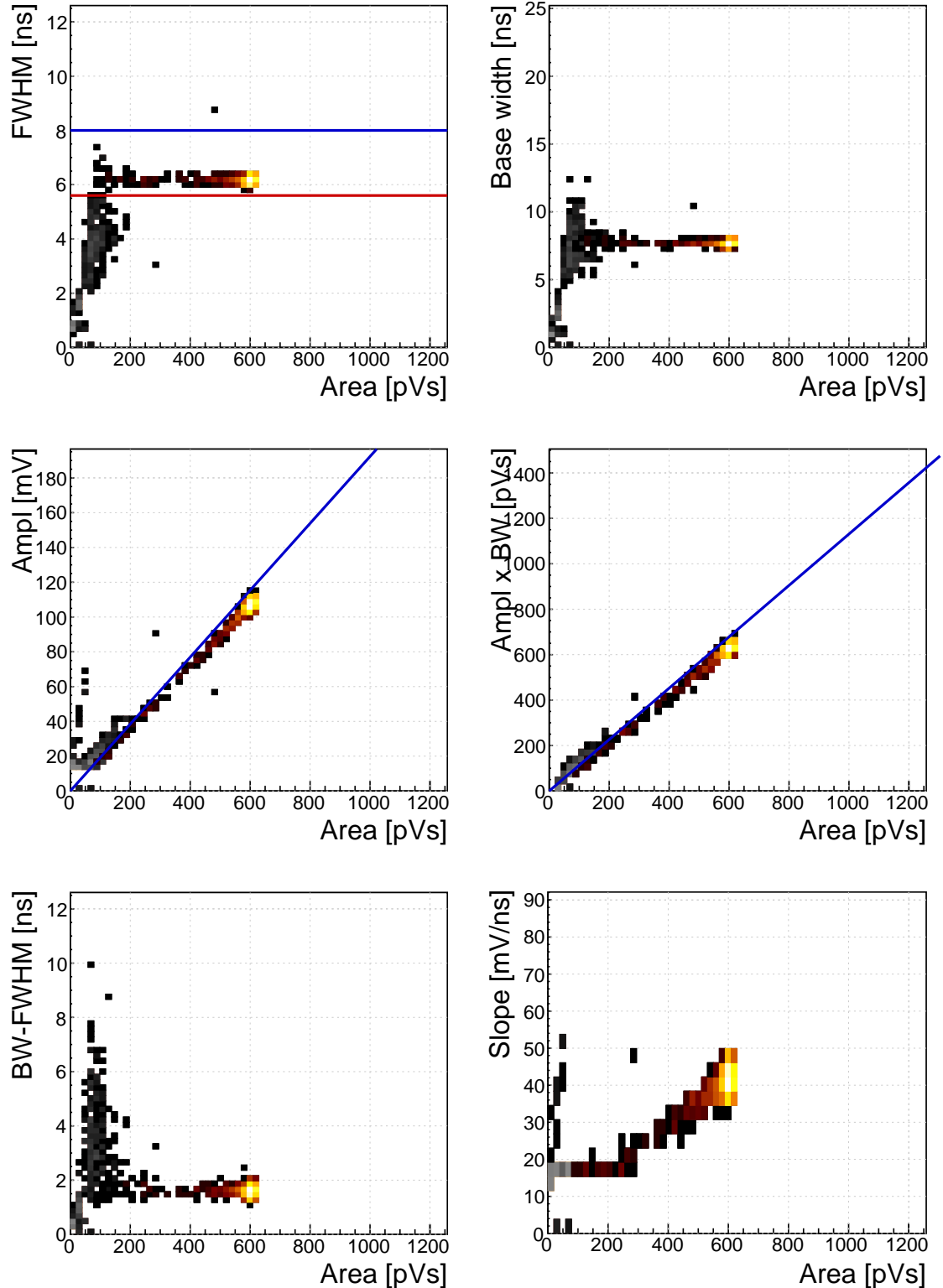
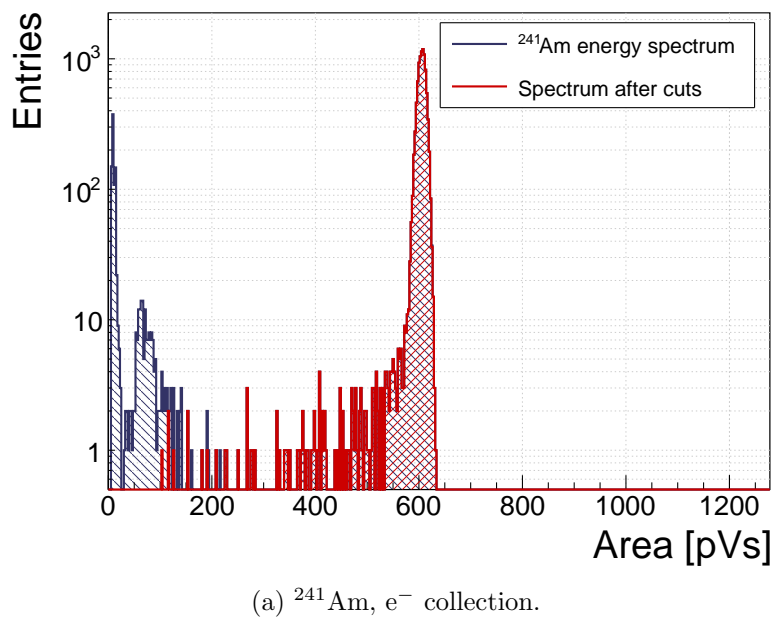


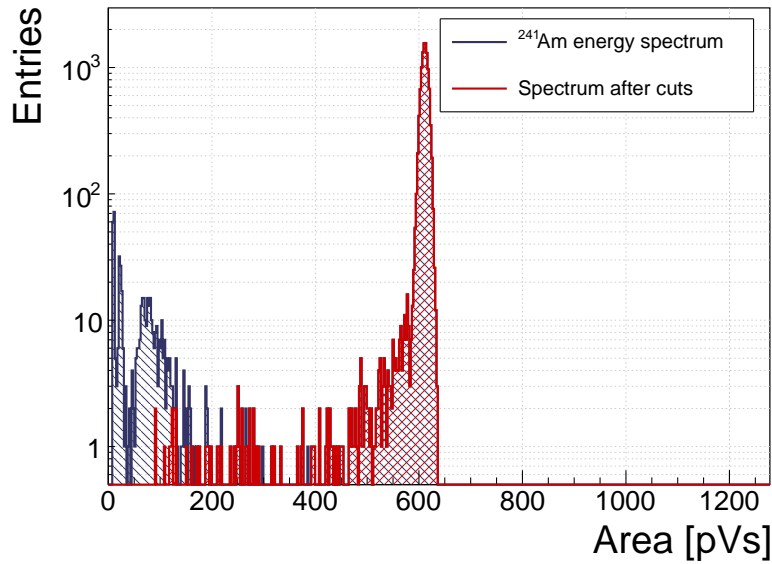
Figure 5.17:  $^{241}\text{Am}$ ,  $\text{h}^+$  collection. Qualifier: FWHM.

## 5.9. SOURCE CALIBRATION

---



(a)  $^{241}\text{Am}, e^-$  collection.



(b)  $^{241}\text{Am}, h^+$  collection.

Figure 5.18:  $^{241}\text{Am}$  area histograms for electron and hole collection.

2577 **5.9.1.2  $^{90}\text{Sr}$  and  $^{60}\text{Co}$  source**

2578 The phase space of the  $^{90}\text{Sr}$  source overlaps entirely with that of the  $^{60}\text{Co}$  source, as  
2579 results from figures 5.19 and 5.20. This renders it virtually impossible to distinguish  
2580 between photons and electrons (MIPs). Comparing the [area, FWHM] phase space  
2581 of the photons and alphas and the high reach of the former, the electron collection of  
2582 the alphas would need to be used to distinguish between the two types of particles.

2583 The one-dimensional histograms in figure 5.21 show a quasi-Landau distribution  
2584 with the MPV at  $\sim 70$  pVs, which is in agreement with the background  $\gamma$  radiation  
2585 emitted by the  $^{241}\text{Am}$  source, as shown in figure 5.18 in the previous subsection. This  
2586 is however not a pure Landau distribution. Relative to the 600 pVs  $\alpha$  peak, the ex-  
2587 pected MPV of MIPs would be  $\sim 30$  pVs, which is not the case in these distributions.  
2588 This is because the PSA device is a self-triggering system, which cuts the lower ener-  
2589 getic particles with the trigger threshold. The resulting distribution is therefore only  
2590 the top portion of the real Landau distribution. Unfortunately this is the limitation  
2591 of the device, governed by the analog noise of the current pre-amplifier.

## 5.9. SOURCE CALIBRATION

---

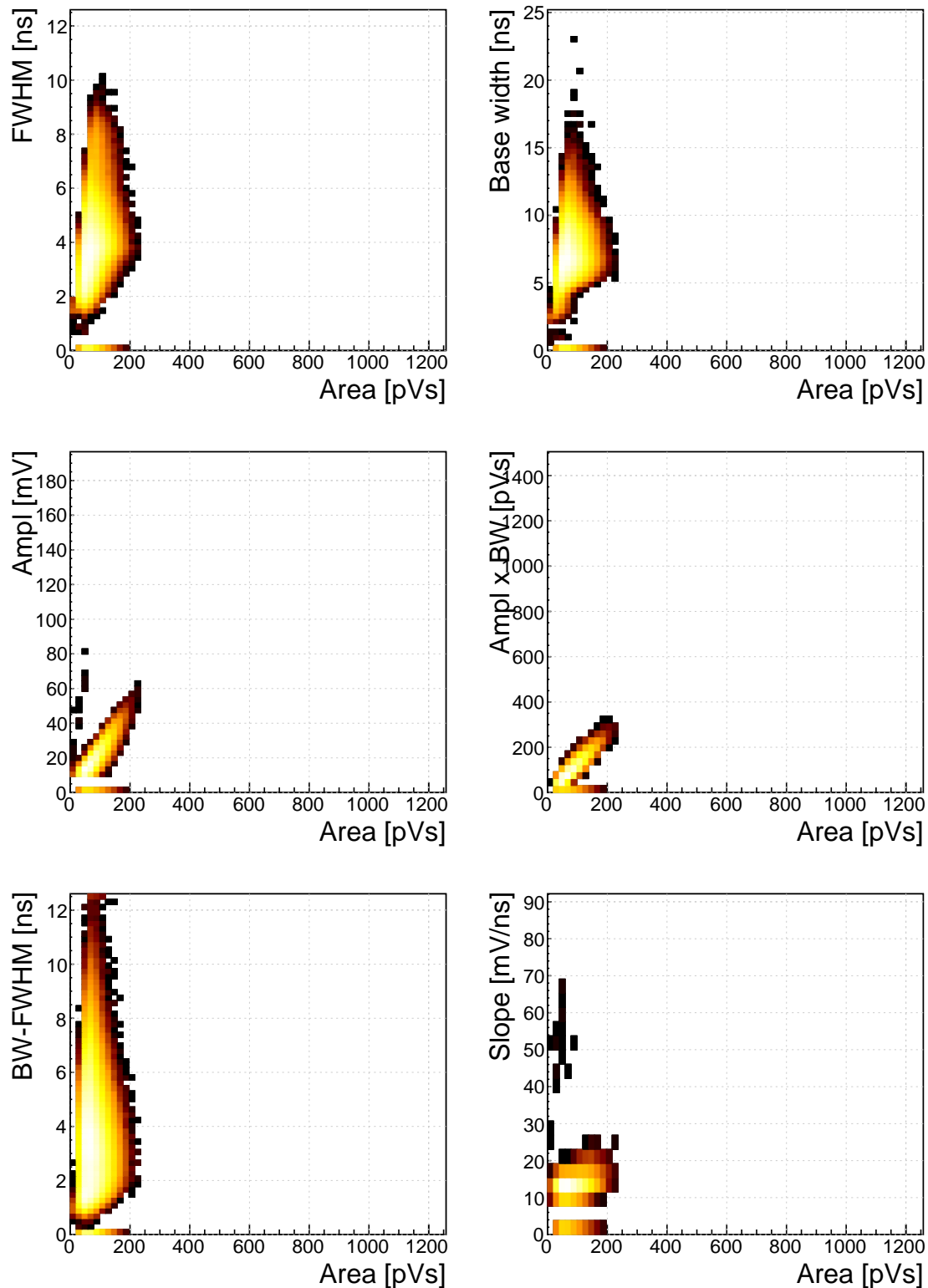


Figure 5.19:  $^{90}\text{Sr}$  scatter plots.

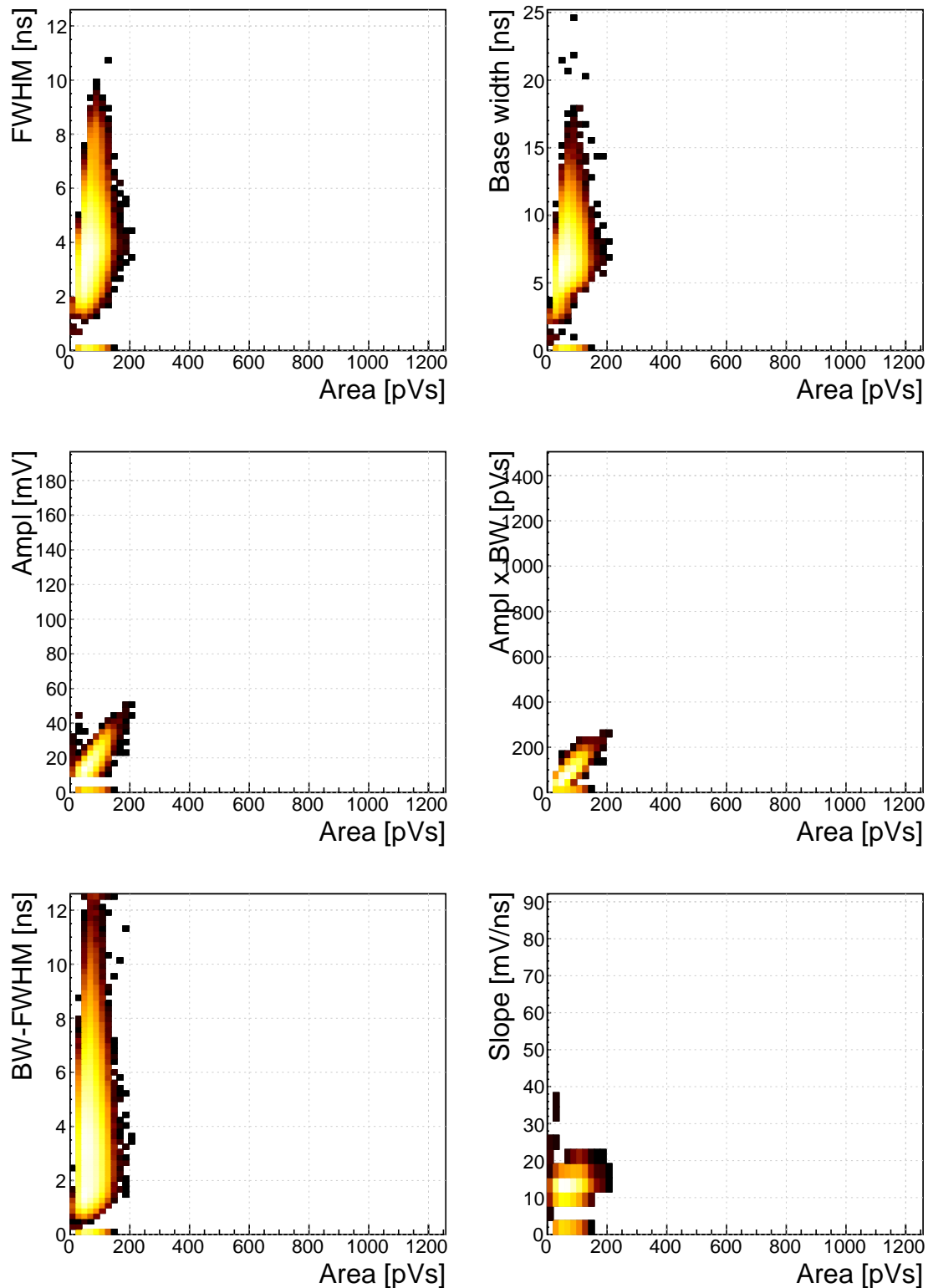


Figure 5.20:  $^{60}\text{Co}$  scatter plots.

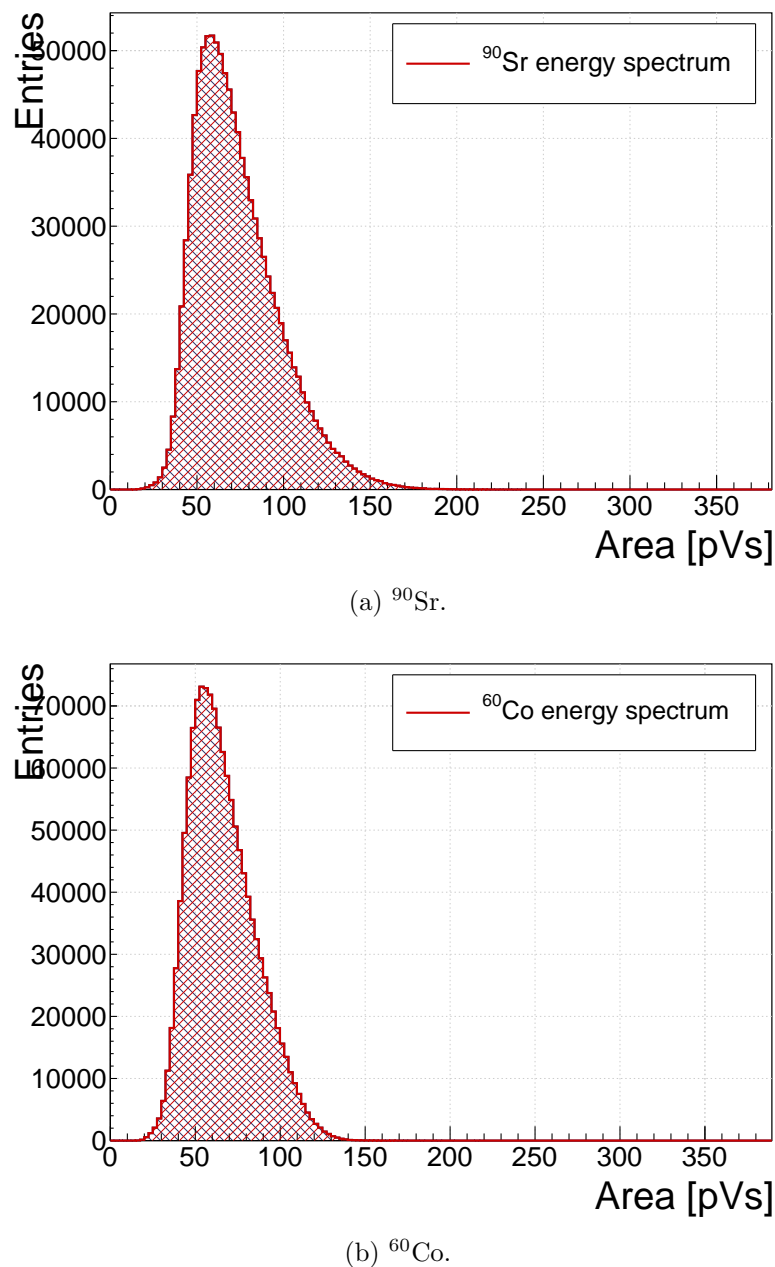


Figure 5.21: Energy distributions for  $\gamma$  and  $\beta$  particles.

## 5.10 Applications in neutron instrumentation

The real-time pulse shape analysis procedure can be applied to more complex systems.  
This section includes three applications where the PSA has been applied.

Semiconductor-based neutron detectors provide a compact technology for neutron detection. However, the cross section of a neutron with the diamond bulk is very low, since it only interacts with the core of the atom. Diamond is mainly used to detect charged particles and photons.

Research neutron reactors radiate a mix of particles, apart from neutrons also photons. The photons are considered a background radiation, concealing the neutron spectrum. When measured with diamond, the signal from neutrons is difficult to distinguish from the photon spectrum. In addition, low energy neutrons do not cause nuclear reactions in the bulk. All in all, the neutron measurements in a reactor present a challenge with diamond. However, by means of the PSA, the neutron signal can be discriminated from the photon background to some extent. The following two cases show how measurements of fast ( $n^+$ ) and thermal ( $n^-$ ) neutrons have been carried out by making use of the PSA.

Note the changing scale on the X axis in the figures.

### 5.10.1 Thermal neutron flux monitoring

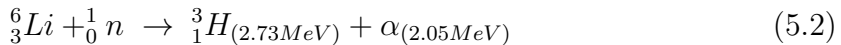
Research neutron reactors like TRIGA MARK II [?] at Atominstitut [?] in Vienna are capable of emitting neutrons at a wide range of energies. The neutron flux is proportional to the current power of the reactor. It is therefore instrumental to monitor the neutron flux to make sure that the reactor operation is within the specified limits. However, the byproduct of the radioactive decays in the core is  $\gamma$  radiation, which has an energy range that overlaps with that of neutrons, making it difficult to measure the neutron flux. This is where PSA and diamond detectors come into play. This section describes the application of thermal neutron flux monitoring by means of the PSA.

Thermal neutrons do not interact with the diamond bulk due to their low kinetic energy (of the order of 0.012 eV). Hence a converter foil has to be added to produce second order effects. Incoming neutrons interact with the foil, producing a set of secondary particles. These can then be detected upon hitting the detector bulk. Common neutron interactions that are used in thermal neutron detection are  $^{10}\text{B}(n,\alpha)^7\text{Li}$  reaction and  $^6\text{Li}(n,\alpha)^3\text{H}$  reaction ( $\alpha$  stands for  $^4_2\text{He}$ , see equation 5.2). The focus in this section is on the latter. With a foil installed, there are several possibilities for neutrons to interact with the detector system. Each of these interactions ionises the diamond bulk in its own way, resulting in a specific shape of the current pulse. A neutron can: 1) interact with the foil, producing an  $\alpha$  and a  $^3\text{H}$ , 2) interact with a carbon atom in the lattice, producing an  $\alpha$  and a  $\gamma$  or even three  $\alpha$ . The thermal neutrons do not have enough kinetic energy to interact with the lattice,

## 5.10. APPLICATIONS IN NEUTRON INSTRUMENTATION

---

2631 therefore the focus is on case (1). The equation for this reaction is the following:



2632 The particles in the first case are produced outside the diamond and get stopped  
2633 immediately upon hitting the sensor. The resulting pulses for both particles have a  
2634 rectangular shape of the same width, because the carriers drift with the same speed  
2635 in both cases. The difference is in the number of free carriers produced - the tritium  
2636 creates more (proportional to the deposited energy), which in turn induces a higher  
2637 pulse.

2638 TRIGA MARK II neutron reactor emits large amounts of  $\gamma$  radiation in the  
2639 energy range up to 3 MeV. This already affects the measurements of  $\alpha$  particles, the  
2640 energy of which peaks at 2.05 MeV in the case of  ${}^6Li$  converter foil. However,  $\gamma$   
2641 background radiation can be suppressed by discriminating current pulses of photons  
2642 from those induced by  $\alpha$  particles. This idea has already been implemented in offline  
2643 analysis in [29, 24]. The results show that the background photons can be subtracted  
2644 successfully. In order to make sure that every single incident thermal neutron has  
2645 been accounted for, the algorithm has been ported to FPGA where it detects and  
2646 analyses particles in real time.

### 2647 5.10.1.1 Measurements

2648 ROSY readout device with the implemented Pulse Shape Analysis was put to a test  
2649 at Atominstut in Vienna. Their TRIGA neutron reactor is capable of delivering  
2650 thermal neutrons with the energy 0.012 eV at a rate of  $10^3 \text{ n cm}^{-2} \text{ s}^{-1}$ , with a  
2651 considerable  $\gamma$  background.

2652 First, the device was calibrated using an unsealed monochromatic  ${}^{241}Am$  source  
2653 with the emitted particle energy  $E_\alpha = 5.12MeV$  (taking into account the losses in  
2654 the air). Then the diamond detector was exposed to the beam. Secondary reaction  
2655 products ( $\alpha$  and  ${}^3H$  particles), created by neutrons hitting the converter foil, were  
2656 detected by the diamond sensor, together with a significant photon background. Then  
2657 the pulse identification algorithm was applied to discriminate between the reaction  
2658 products and the photons.

2659 The main parts of the detector are an sCVD diamond sensor sized  $4.7 \times 4.7 \text{ cm}^2$   
2660 and a  $1.8 \mu\text{m}$  thick LiF converter foil, both embedded in an RF-tight PCB. The  
2661 diamond sensor is biased with a bias voltage of  $1 \text{ V}/\mu\text{m}$  and capacitively coupled to  
2662 CIVIDEC's C2 40 dB wide bandwidth current preamplifier. A 5 m long BNC cable  
2663 connects the preamplifier to CIVIDEC ROSY box. The detector assembly together  
2664 with the preamplifier has to be placed in front of an exit hole of the reactor.

2665 Note: this data set has been taken with an older version of the firmware, which  
2666 only measured a limited number of pulse parameters.

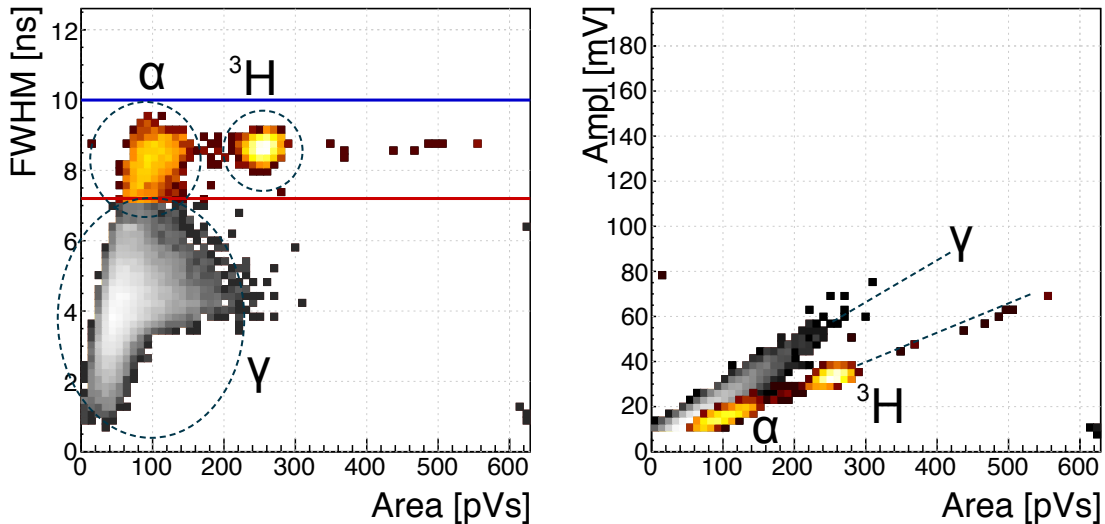


Figure 5.22: Thermal neutrons, photons. Qualifier: FWHM.

#### 2667 5.10.1.2 Results and discussion

2668 The data collected by the PSA show a high flux of photons, which covers a wide area  
 2669 range. The  $^3\text{He}$  peak is clearly visible and has almost no overlap with the photon  
 2670 cluster. The  $\alpha$  cluster has a much lower energy and is in the same energy range as  
 2671 the photons. However, if a FWHM parameter is observed, a distinction between the  
 2672 photons and the  $\alpha$  can be seen. By setting a qualifier to the right value, the photon  
 2673 background is cut away, leaving only the thermal neutron decay products in the data  
 2674 set, as shown in figure 5.22. The resulting one-dimensional area histogram before and  
 2675 after applied cuts is shown in figure 5.23. The blue distribution is the mixed field  
 2676 of background photons, tritium and  $\alpha$  particles. The latter are completely hidden in  
 2677 the  $\gamma$  energy distribution. After applied qualifiers the  $\alpha$  peak suddenly appears.

#### 2678 5.10.1.3 Conclusion

2679 By applying the FWHM qualifier to the acquired data from the TRIGA neutron reactor,  
 2680 the  $\alpha$  and tritium particles can be identified and separated from the  $\gamma$  background.  
 2681 The resulting cleaned data can be used to correctly count the thermal neutrons de-  
 2682 tected by the diamond sensor.

### 2683 5.10.2 Fusion power monitoring

2684 Many research collaborations around the world are trying to develop a functional  
 2685 fusion reactor, which could provide a cleaner energy source. One of them is ITER [8],  
 2686 a research fusion reactor being built in France. The idea behind it is to harvest  
 2687 energy from the fusion of light atoms into a heavier one. For ITER the fuel chosen

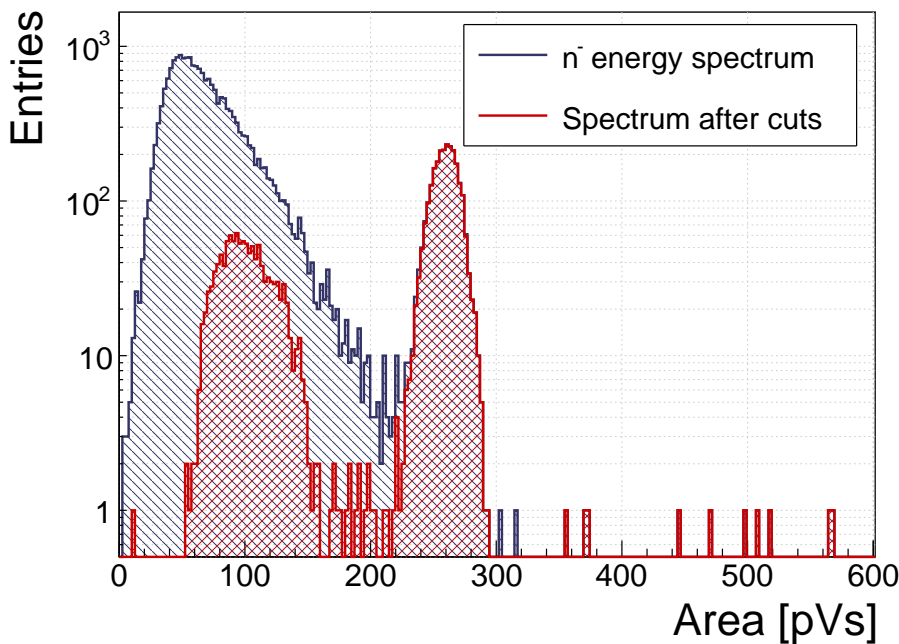
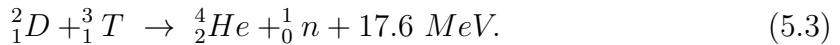


Figure 5.23: Energy spectrum after applied qualifiers reveals the tritium and  $\alpha$  peak

2688 is a mixture of deuterium and tritium, which fuse into a helium atom at extremely  
 2689 high temperatures (plasma), emitting a highly energetic neutron as a byproduct. The  
 2690 equation is the following:



2691 The  $\alpha$  particle immediately deposits its energy within the plasma. The neutron, due  
 2692 to its neutral charge, continues its way out of the system where it is stopped. The  
 2693 stopping power is converted into energy, which heats the water into steam, which in  
 2694 turn spins the turbines, generating electricity.

2695 It is possible to monitor the activity of the reactor by measuring the flux of neu-  
 2696 trons emitted. Neutron diagnostics such as neutron cameras, neutron spectrometers  
 2697 and neutron flux monitors therefore provide robust measurements of fusion power. A  
 2698 high  $\gamma$  background makes it difficult to accurately measure the neutron flux. This is  
 2699 a motivation to use a diamond based detector with a real-time PSA algorithm.

2700 The neutrons emitted are 14 MeV mono-energetic fast neutrons. The most ac-  
 2701 curate and efficient way to detect them with a diamond detector is by means of a  
 2702  $C_{12}(n,\alpha)$  reaction with a carbon atom in the ballistic centre [30]. In this region the  
 2703 positive and negative charge carriers created by  $\alpha$  that start drifting in the opposite  
 2704 directions need the same time to reach the opposite electrodes.

### 2705 5.10.2.1 Measurements

2706 The  ${}^{239}\text{Pu Be}$  neutron source has been used to simulate the fusion reactor. It emits a  
 2707 mixed field of neutrons and photons with a wide range of energies. The neutrons are

rarely detected with diamond – the interactions happen mostly in the electrodes on either side of the detector. The  $\alpha$  particles created by the interactions are detected by the diamond. Depending on the side of the interaction, the created pulse is either due to hole– or electron collection. These two interactions make the two distinct lines in the [area, FWHM] phase space at 9 ns and 6 ns, as shown in figure 5.24, top left plot.

A very interesting interaction point is the ballistic centre [?] of the diamond. A ballistic centre is the position from which it takes the holes and the electrons the same amount of time to drift to the opposite electrodes. In this case the shortest possible pulse is created. Conversely, to conserve the collected charge and thus the pulse area, the pulse amplitude must be the highest at the ballistic centre. The entries in between are created by neutron interactions at random positions in the diamond, which produce pulses of various shapes.

### 5.10.2.2 Results and discussion

Coming back to the motivation, the most efficient way of counting the 14 MeV neutrons is through the measurement of the neutrons interacting in the ballistic centre [?]. To extract this type of interaction several qualifiers must be used. The first possibility is the FWHM set to 3–5 ns. However, this time the cuts on the [area, amplitude] and the [area, amplitude  $\times$  base value] phase space are preferred. First, a minimum constant amplitude qualifier is set to 22 mV, as shown in figure 5.24, middle left plot. Then a linear amplitude qualifier is set such that only the pulses with the highest amplitude for every area value are taken. This ensures that the high pulses from the ballistic centre are chosen. Second, a maximum linear amplitude  $\times$  base value qualifier is set such that only the pulses bearing the closest resemblance to a rectangle are chosen, as shown in figure 5.24, middle right plot. In this phase space the entries at the bottom of the distribution are bearing more resemblance to a rectangle whereas those at the top are more akin to triangles.

The resulting [area, FWHM] subfigure after applied qualifiers highlights the entries with a FWHM of 4 ns, which is the width of the pulses induced by neutrons interacting in the ballistic centre. This proves that these combined qualifiers indeed pinpoint these neutron interactions. The final one-dimensional area/energy distribution of the neutrons interacting in the ballistic centre is shown in figure 5.25.

The result could be further improved by further constraining the identification, e.g to define the minimum FWHM constant qualifier and the minimum slope constant qualifier.

### 5.10.2.3 Conclusion

By applying the appropriate qualifiers to the data, the neutron interactions in the ballistic centre can be identified.

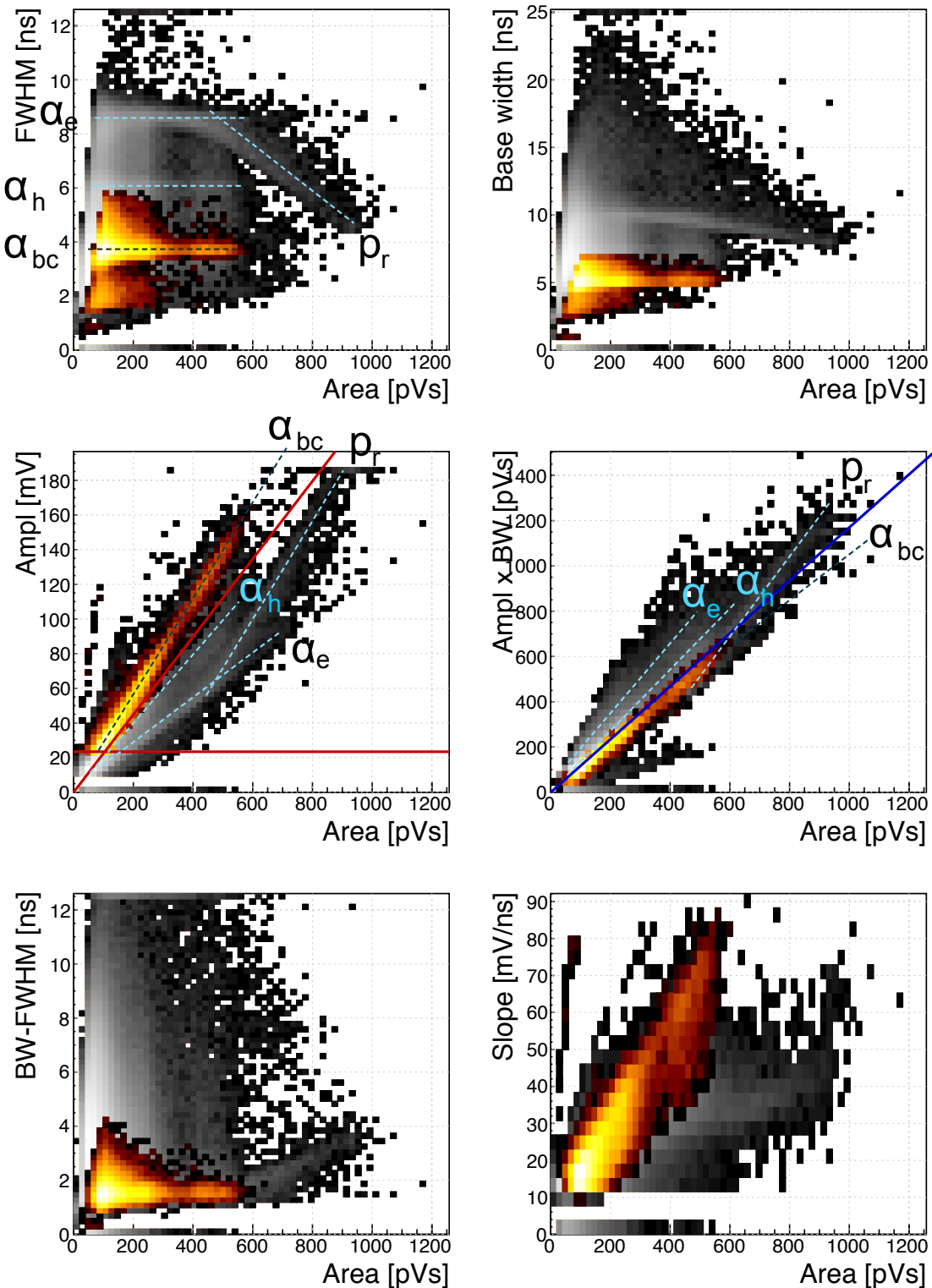


Figure 5.24:  $^{239}\text{Pu Be}$ . Qualifiers: BW-FWHM, FWHM, Form Factor

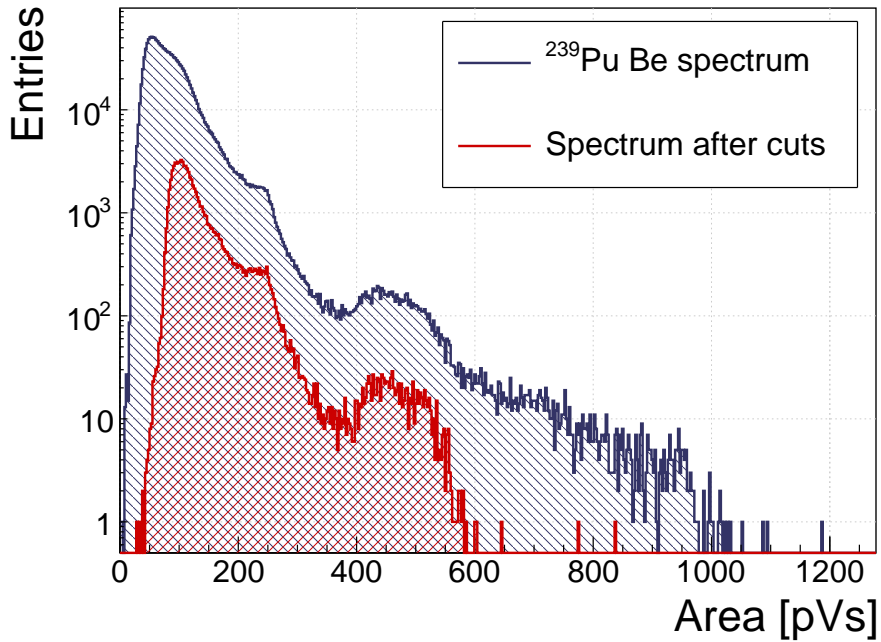


Figure 5.25:  $^{239}\text{Pu}$  Be, energy distribution of the neutrons interacting in the ballistic centre.

### **2746 5.10.3 Fast and thermal neutron monitoring**

**2747** The CROCUS reactor at EPFL [3] is a research neutron reactor. The research group  
**2748** working on the reactor is interested in measuring neutrons with energies between  
**2749** 1–2 MeV, which is overlapping with the  $\gamma$  background energy range.

**2750** The highest output power of the CROCUS reactor is 100 W. Currently there  
**2751** are fission chambers that carry out the neutron counting, which is a measure of the  
**2752** activity of the reactor. The new goal is to measure both neutrons and photons,  
**2753** but separately. The pulse shape analysis is a good solution for this task. For this, a  
**2754** 400  $\mu\text{m}$  thick diamond detector with a specially designed casing was added to measure  
**2755** the activity. The LiF foil was added for conversion of thermal neutrons. The ROSY  
**2756** box with the integrated PSA routine was used for signal analysis.

#### **2757 5.10.3.1 Measurements**

**2758** At the highest reactor activity the system counts particles at a rate of  $\sim 1.5 \times 10^5 \text{ s}^{-1}$ .  
**2759** The results from a test run at 10 W output power are shown in figure 5.26. The data  
**2760** include a mixed field consisting of fast neutrons, photons and of  $\alpha$  and  $^3\text{H}$  particles  
**2761** as products of thermal neutron decay in the LiF foil in front of the detector. The  
**2762** energy deposited in the diamond is not as high as that from the  $^{239}\text{Pu}$  Be source.  
**2763** In addition, the analog noise during this measurement is higher than in the previous  
**2764** application. These conditions combined make particle identification at CROCUS a  
**2765** challenging task.

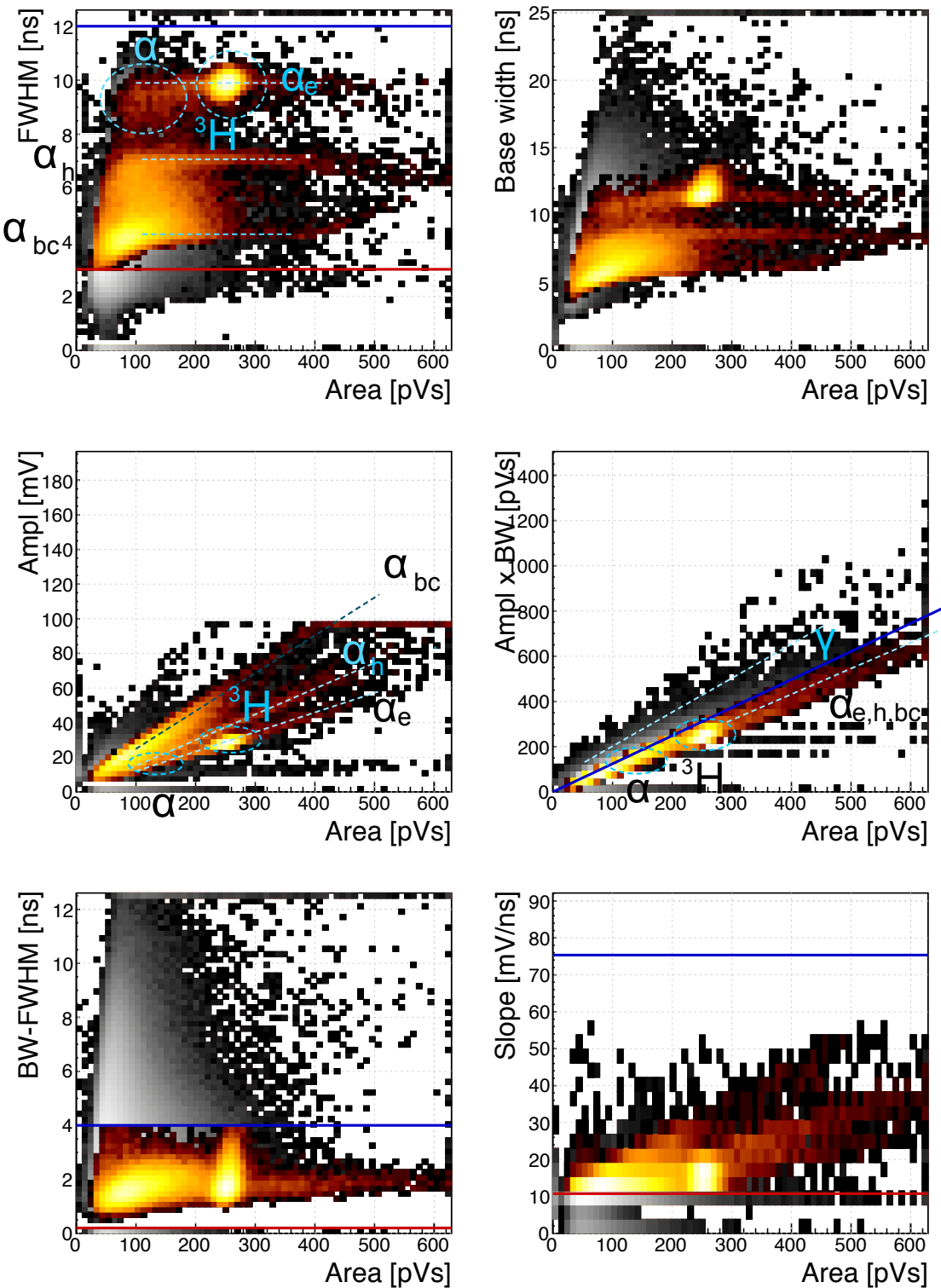


Figure 5.26: Fast neutrons, thermal neutrons, photons. Qualifiers: BW-FWHM, FWHM, Form factor, Slope.

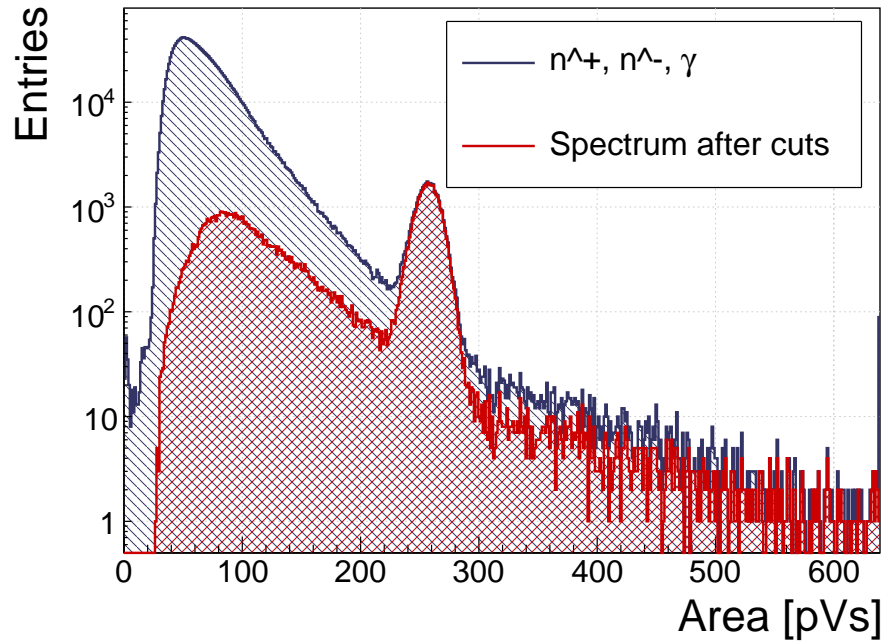


Figure 5.27: Energy spectrum in CROCUS before and after applied qualifiers

2766 **5.10.3.2 Results and discussion**

2767 The aim of this exercise is to identify both thermal and fast neutrons. For this the  
2768 main qualifier used is the Form Factor - the linear line in the [area, amplitude×base  
2769 value] phase space. Additional FWHM, FWHM-BW and slope constant qualifiers are  
2770 used to clean the outlying entries. The resulting accepted entries in figure 5.26 have  
2771 the distinctive three-line fast neutron signature in the [area, FWHM] subfigure with  
2772 two superimposed islands by the  $\alpha$  and  ${}^3\text{H}$  cluster produced by thermal neutrons in the  
2773 LiF foil. The  $\gamma$  background is sufficiently suppressed. The resulting one-dimensional  
2774 histogram of the area/energy distribution is shown in figure 5.27.

2775 **5.10.3.3 Conclusion**

2776 By applying the Form Factor qualifier both fast and thermal neutrons can be identi-  
2777 fied, suppressing the  $\gamma$  background.

2778 **5.11 Conclusion**

2779 This chapter describes a system that can identify the type of radiation in real time.  
2780 The system is implemented on an FPGA in a CIVIDEC ROSY box and is used with  
2781 diamond detectors. The signal from the diamond sensor is read in and analysed in the  
2782 firmware. First the shape of the pulse is parametrised. Then the logic determines the  
2783 type of particle according to the user defined cuts. Finally the parameters are written  
2784 into a histogram, which is read out by the user. The firmware is designed to carry  
2785 out the pulse shape analysis of a single pulse in  $\sim 200$  ns, yielding a maximum pulse  
2786 rate of  $5 \times 10^6$  particles per second. The rate as well as the linearity the measurement  
2787 stability with respect to noise have been verified using a pulse generator. Then several  
2788 radioactive sources were used to calibrate the device. Finally the system has been set  
2789 up in two neutron reactors to test the operation in a mixed field containing thermal  
2790 neutrons, fast neutrons and photons. The identification can be optimised using a  
2791 combination of qualifiers to achieve the desired effect.

<sub>2792</sub>

# Bibliography

- <sub>2793</sub> [1] *ASIC*. [http://www.embedded-systems-portal.com/CTB/CTB\\_images/L2/L2 ASIC.jpg](http://www.embedded-systems-portal.com/CTB/CTB_images/L2/L2 ASIC.jpg).
- <sub>2794</sub> [2] *Atominstitut, Technical University of Vienna, Austria*.  
<sub>2795</sub> <http://ati.tuwien.ac.at/startpage/EN/>.
- <sub>2796</sub> [3] *CROCUS neutron reactor*. <http://lrs.epfl.ch/page-55655-en.html>.
- <sub>2797</sub> [4] *DRS4*. <https://www.psi.ch/drs/evaluation-board>.
- <sub>2798</sub> [5] *Element Six*. <http://www.e6.com>.
- <sub>2799</sub> [6] *European Centre for Nuclear Research, CERN*. <http://home.cern>.
- <sub>2800</sub> [7] *IHa Technologies Pte. Ltd.* <https://www.2atechnologies.com>.
- <sub>2801</sub> [8] *ITER fusion reactor*. <https://www.iter.org/>.
- <sub>2802</sub> [9] *Neutron Time-of-flight experiment*. <https://ntof-exp.web.cern.ch/ntof-exp/>.
- <sub>2803</sub> [10] *Paul Scherrer Institute*. <https://www.psi.ch/>.
- <sub>2804</sub> [11] *RD42 collaboration*. <http://rd42.web.cern.ch/rd42/>.
- <sub>2805</sub> [12] *TRIGA MARK II neutron reactor*. <http://ati.tuwien.ac.at/reactor/EN/>.
- <sub>2806</sub> [13] *Xilinx Virtex 5 FPGA*. <http://www.hdl.co.jp/XCM-109/top.560.jpg>.
- <sub>2807</sub> [14] *Determination of operational dose equivalent quantities for neutrons*. ICRU,  
<sub>2808</sub> Washington, DC, 2001.
- <sub>2809</sub> [15] General Atomics. *View of the TRIGA reactor*. 2015.
- <sub>2810</sub> [16] H. Bethe and J. Ashkin. *Experimental Nuclear Physics*, ed. E. Segre, page 253,  
<sub>2811</sub> 1953.
- <sub>2812</sub> [17] W. Blum, W. Riegler, and L. Rolandi. Particle Detection with Drift Chambers,  
<sub>2813</sub> volume 2 of 2. Springer-Verlag, Berlin Heidelberg, 2008.
- <sub>2814</sub> [18] Giorgio Brianti. SPS North Experimental Area. Technical Report CERN-SPSC-  
<sub>2815</sub> T-73-8. LabII-EA-Note-73-4, CERN, Geneva, 1973.

## BIBLIOGRAPHY

---

- 2816 [19] Maximilien Brice. *View of the nTOF detector*. Oct 2010.
- 2817 [20] Maximilien Brice. *LHC tunnel*. Jan 2011.
- 2818 [21] P. Carazzetti and H. R. Shea. *Electrical breakdown at low pressure for planar*  
2819 *microelectromechanical systems with 10- to 500  $\mu\text{m}$  gaps*. *J. Micro/Nanolith.*  
2820 *MEMS MOEMS*, (8(3), 031305), Jul-Sep 2009.
- 2821 [22] Daniel Dominguez. *Standard Model. Le modele standard*. General Photo, Mar  
2822 2015.
- 2823 [23] CIVIDEC Instrumentation GmbH. *sCVD diamond sensor*.  
2824 <http://www.cividec.at>, 2015.
- 2825 [24] E. Griesmayer, R. Bergmann, H. Böck, M. Cagnazzo, P. Kavrigin, B. Mor-  
2826 genbesser, and M. Villa. *A Novel Neutron Flux Monitor Based On Diamond*  
2827 *Detectors at the Vienna TRIGA Mark II Reactor*. submitted to the proceedings  
2828 of ICRR 2015, 2015.
- 2829 [25] E. Griesmayer and B. Dehning. Diamonds for beam instrumentation. *Physics*  
2830 *Procedia*, 37:1997 – 2004, 2012. Proceedings of the 2nd International Conference  
2831 on Technology and Instrumentation in Particle Physics (TIPP 2011).
- 2832 [26] Moritz Guthoff, Wim de Boer, and Steffen Müller. Simulation of beam induced  
2833 lattice defects of diamond detectors using {FLUKA}. *Nuclear Instruments and*  
2834 *Methods in Physics Research Section A: Accelerators, Spectrometers, Detectors*  
2835 *and Associated Equipment*, 735:223 – 228, 2014.
- 2836 [27] M. Huhtinen. Simulation of non-ionising energy loss and defect formation in  
2837 silicon. *Nuclear Instruments and Methods in Physics Research A*, 491:194–215,  
2838 September 2002.
- 2839 [28] Hendrik Jansen, Norbert Wermes, and Heinz Pernegger. *Chemical Vapour De-*  
2840 *position Diamond - Charge Carrier Movement at Low Temperatures and Use in*  
2841 *Time-Critical Applications*. PhD thesis, Bonn U., Sep 2013. Presented 10 Dec  
2842 2013.
- 2843 [29] P. Kavrigin, P. Finocchiaro, E. Griesmayer, E. Jericha, A. Pappalardo, and  
2844 C. Weiss. *Pulse-shape analysis for gamma background rejection in thermal neu-*  
2845 *tron radiation using CVD diamond detectors*. *Nuclear Instruments and Methods*  
2846 *in Physics Research A*, (795), 2015.
- 2847 [30] P. Kavrigin, E. Griesmayer, F. Belloni, A.J.M. Plompen, P. Schillebeeckx, and  
2848 C. Weiss.  $^{13}\text{C}(n,\alpha_0)^{10}\text{Be}$  cross section measurement with sCVD diamond detec-  
2849 tor. submitted to EPJA, 2016.
- 2850 [31] Claude A. Klein. Radiation-induced energy levels in silicon. *Journal of Applied*  
2851 *Physics*, 30(8):1222–1231, 1959.

## BIBLIOGRAPHY

---

- [32] Gregor Kramberger, V. Cindro, A. Gorisek, I. Mandic, M. Mikuz, and M. Zavrtanik. Effects of bias voltage during priming on operation of diamond detectors. *PoS, Vertex2012:013*, 2013.
- [33] W. Y. Liang. Excitons. *Physics Education*, 5:226–228, July 1970.
- [34] Claudia Marcelloni De Oliveira. *IBL installation into the inner detector of the ATLAS Experiment side C. General Photo*, May 2014.
- [35] M. Mikuž. *Diamond sensors for high energy radiation and particle detection*. TIPP, 2011.
- [36] W P C Mills. *The present performance of the SPS*. *IEEE Trans. Nucl. Sci.*, 26(CERN-SPS-AOP-79-9):3176–3178. 3 p, Mar 1979.
- [37] S. F. Novaes. *Standard model: An Introduction*. In *Particles and fields. Proceedings, 10th Jorge Andre Swieca Summer School, Sao Paulo, Brazil, February 6-12, 1999*, 1999.
- [38] Joao Pequenao. *Computer generated image of the whole ATLAS detector*. Mar 2008.
- [39] Heinz Pernegger. *The Pixel Detector of the ATLAS Experiment for LHC Run-2*. Technical Report ATL-INDET-PROC-2015-001, CERN, Geneva, Feb 2015.
- [40] S. Ramo. *Currents Induced by Electron Motion*. *Proceedings of the IRE*, 27:584–585, 1939.
- [41] V. Sarin. *Comprehensive Hard Materials*. Elsevier Science, 2014. p. 411.
- [42] W. Shockley. *Currents to Conductors Induced by a Moving Point Charge*. *Journal of applied Physics*, 9:635, 1938.
- [43] C. Weiss. A CVD diamond detector for  $(n,\alpha)$  cross-section measurements. PhD thesis, TU Wien, Vienna, 2014.
- [44] C. Weiss, H. Frais-Kölbl, E. Griesmayer, and P. Kavrigin. *Ionization signals of diamond detectors in fast neutron fields. publication in preparation*, 2016.
- [45] J. L. Yarnell, J. L. Warren, and R. G. Wenzel. Lattice vibrations in diamond. *Phys. Rev. Lett.*, 13:13–15, Jul 1964.